Doctorate Dissertation
博士論文

Positron Timing Measurement to Search for Lepton Flavor Violating Decay in MEG II

（荷電レプトン非保存現象探索のための
MEG II実験における陽電子時間測定）

A Dissertation Submitted for Degree of Doctor of Philosophy
May 2018
平成 30 年 5 月博士（理学）申請

DEPARTMENT OF PHYSICS, GRADUATE SCHOOL OF SCIENCE,
THE UNIVERSITY OF TOKYO
東京大学大学院理学系研究科物理学専攻

Miki Nishimura
西村　美紀

Abstract

A new positron timing counter has been developed for the MEG II experiment which aims to explore new physics beyond the standard model of the particle physics by searching for the $\mu^+ \to e^+\gamma$ decay with the world's highest sensitivity. The most stringent upper limit for the branching fraction for the decay was set by the MEG experiment in 2016 to be 4.2×10^{-13} (90 % confidence level) by reducing background effectively [1]. The dominant background was the accidental coincidence between uncorrelated positrons and photons. Therefore the precise timing measurements of the positrons and the photons were strongly required to separate the signals from the background.

To realize a further deep search for the $\mu^+ \to e^+\gamma$ decay in the MEG II experiment, further development of detectors is essential to reduce the background which increases with the planned higher beam intensity. Moreover the detectors should keep their performance at the higher background rate.

To satisfy the requirements, we established the innovative concept of the timing counter: the pixelated timing counter. It is composed of 512 small counters, each of which consists of a fast plastic scintillator plate with 6 silicon-photomultipliers (SiPM) at both ends. This innovative pixelated design helps to reduce pile-up events and allows simultaneous multiple timing measurements to obtain a better overall resolution. Furthermore the timing counter takes a role as a trigger of timing. The online time resolution reduces the trigger rate and data size effectively.

Positron timing measurement can be improved by the single counter resolution below 100 ps and the multiple measurement scheme. The design of the single counter is optimized to achieve the best time resolution. We assembled and tested ~550 counters and obtained the time resolution (σ) of 65–90 ps.

Via several beam tests we also demonstrated the improvement of the time resolution with the multiple counters. Furthermore to extract the maximum performance of the multiple timing measurement, we established a reconstruction algorithm treating multiple hits effectively, and calibration systems among the counters.

After finalizing the design of the timing counter and the several beam tests, the final detector was constructed and installed in 2017. We successfully carried out a pilot run of the timing counter including the calibration system, slow control system, and trigger system. An time resolution below 40 ps with more than 8 counters is demonstrated. Taking into account the number of hits from the signal positron obtained by a Monte-Carlo simulation, the result corresponds to an average resolution of 38.5 ps for the signal positrons.

The overall positron time resolution including the effect from uncertainty from tracking by drift chamber is 40 ps, which is more than twice better than that in the MEG experiment. The resolution of the relative time between the positrons and the photons is

estimated to be 64–80 ps by assuming the time resolution of photon to be 50–70 ps. The result indicates 35–50 % background reduction from the MEG experiment from the timing measurement point of view and it satisfies to realize a sensitivity of 6×10^{-14}. In conclusion, the timing counter enables the MEG II experiment to realize the unprecedentedly deep search for the $\mu^+ \to e^+\gamma$ decay .

Contents

Chapter 1

Introduction

The theory of everything has been dreamed by particle physicists for more than a hundred year. *Everything* means all interactions and fundamental particles. The trial is still underway and what is known is the standard model (SM) in the particle physics. The SM have succeeded in explaining a lot of phenomena, but still it does not explain *everything* such as the origin of the dark matter and the neutrino oscillation observed by experimentalists. Moreover from the theoretical point of view, it is not exactly unified, nor does it explain the generations of the particles. Consequently, new physics beyond the SM (BSM) should be exist.

The conservation of the lepton flavor is one of the huge questions which the SM cannot explain because the origin of three generations of leptons is not described. Therefore there is a room for BSM to drop their hints. Actually the neutrino flavor oscillation was already discovered, which cannot be explained by the SM because of the assumption of the massless neutrinos. On the other hand, in the charged lepton sector, no flavor violation is observed. However, many models of new physics predict charged lepton flavor violation (cLFV) large enough to be detected by near future experiments.

The most stringent upper limit on the branching fraction of $\mu^+ \to e^+\gamma$ decay, which is one of cLFV decays, was set by the MEG experiment [1], which yielded the upper limit of 4.2×10^{-13} (90 % confidence level). In general this result from MEG is most stringent limit on BSMs in every cLFV decays. For a deeper search physicists of the MEG experiment aim at a sensitivity enhancement and planned an upgrade experiment, called the MEG II experiment. To realize the ultimate sensitivity of the $\mu^+ \to e^+\gamma$ search, the upgrade of the detectors is essential against the increasing background with the beam intensity increase.

Since the dominant background is accidental background made by detecting the uncorrelated positron and photon at the same time, the accurate time measurement is strongly required. Therefore we innovated a new positron timing counter for the MEG II experiment. Use of silicon photo multipliers (SiPMs) allows finer segmentation of the detector. One counter is composed of $120 \times (40\text{–}50) \times 5$ mm^3 fast plastic scintillator and 6-SiPMs at the both end. To extract the maximum performance from the SiPMs, we employed series connection. In total 512 counters are used. This novel design reduces pile up events and improves the overall positron timing resolution significantly.

In this thesis, we will discuss the positron timing measurement focusing on the timing counter performance and ability for the $\mu^+ \to e^+\gamma$ search in the MEG II experiment. First the physics motivation of the search will be discussed in detail in Chapter 2 and then Chapter 3 will describe the overall of the MEG II experiment. The detailed design and the quality of each component of the timing counter will be introduced in Chapter 4

and the analysis concept will be described in Chapter 5. After proving the performance by the multiple time measurement with the counters by several beam tests in Chapter 6, we will show the final performance of the timing counter obtained with the final set up of the beam, the magnetic field, the electronics, and the calibration system in the MEG II experiment in Chapter 7. Finally the expected final performance of the time measurement of $\mu^+ \to e^+ \gamma$ and the expected final sensitivity of MEG II will be discussed in Chapter 8 and the thesis will be concluded in Chapter 9.

Chapter 2

Physics Motivation

In this chapter, we will discuss the physics motivation of the $\mu \to e\gamma$ decay search. This muon decay is forbidden in the standard model (SM) of the particle physics, but many of new physics beyond the SM (BSM) predict this decay at a branching fraction of $O(10^{-13})$–$O(10^{-14})$.

2.1 Physics beyond the Standard Model

The ultimate goal of particle physics is to understand all the interactions and all the particles in the Universe by the simplest formula. The standard model in particle physic is a very successful theory to explain many phenomena. It is based on the gauge symmetry of $SU(3)_c \times SU(2)_L \times U(1)_Y$. Though the SM is a successful model, several questions are still remained. First of all it is not exactly unified. The gauge symmetry which the SM has is represented as the direct product of three gauge groups, which have independent coupling constants. Moreover the SM does not include the gravitational interaction at all.

Secondly, the SM does not explain the generations of the particles though we know three generations of quarks and leptons which are distinguished with their masses and flavors. The fundamental reason is the existence of Higgs boson. It is not required by a gauge symmetry but is added artificially to generate spontaneous breaking of the gauge symmetry. Therefore the Yukawa coupling between Higgs boson and each particle, and the mixing pattern between the generations are free parameters independent of the gauge symmetry in the SM. The discovery of the Higgs boson in 2012 [3,4] realized the problem of the lack of the underlying principle for the Higgs existence as well as confirmed the mechanism of generating mass. These two problems of non-single gauge groups and the generations ordered by nobody are the origins of all the free parameters in the SM.

Due to the problems discussed above, it is natural that the SM is not regarded as a complete theory but an effective theory at a low-energy scale. In general, the high energy scale ($\Lambda_{\text{cut-off}}$) of the new physics should be much higher than the weak interaction scale ($M_W \ll \Lambda_{\text{cut-off}}$). However in the process of explaining this huge difference among the energy scales, the absence of the requirement for Higgs boson from any gauge symmetry raises the quadratic divergence in the radiative corrections, which requires a fine tunning between the bare mass and the radiative corrections in Higgs mass. This unnaturalness is called the hierarchy problem.

Moreover some experimental results also indicate the existence of BSM. The neutrino oscillation, which is not described by the SM, was discovered. It demands the modification of the SM. The observation of the cold dark matter also suggests the existence of a new particle in the Universe.

2.1.1 Supersymmetry [2]

The Supersymmetric (SUSY) model is one of the candidates for BSM to solve these problems. By introducing a SUSY partner for each SM particle and the symmetry under the super-transformation between boson and fermion, the divergence in the radiative corrections in the Higgs mass is canceled by the difference of statistics between boson and fermion. Furthermore, supersymmetry induces the gravitational interaction naturally. Since the gravitational interaction is not a linear interaction, in general it cannot be renormalized because of the divergence. However, the divergence is suppressed by combining the Poincaré symmetry and the supersymmetry. Another point to notice is that the lightest SUSY particle can be the dark matter.

In the real world any SUSY particles are observed which means that the supersymmetry is broken. Therefore SUSY breaking mechanism is essential and depends on the models.

2.2 $\mu \to e\gamma$ Decay as Touchstone for New Physics

Muon is the particle in the second generation of charged leptons with heavier mass than electron mass. It was discovered in 1937 in cosmic rays [5]. Historically studies on muon decays including the search for $\mu \to e\gamma$ decay have contributed to the deep understanding of the SM such as the lepton flavor conservation. Since the first search of $\mu \to e\gamma$ in 1947, beams and detectors developments have pushed down the upper limit on the branching fraction of the decay as shown in Fig. 2.1. Nowadays the search changes its role to provide deep insight for new physics.
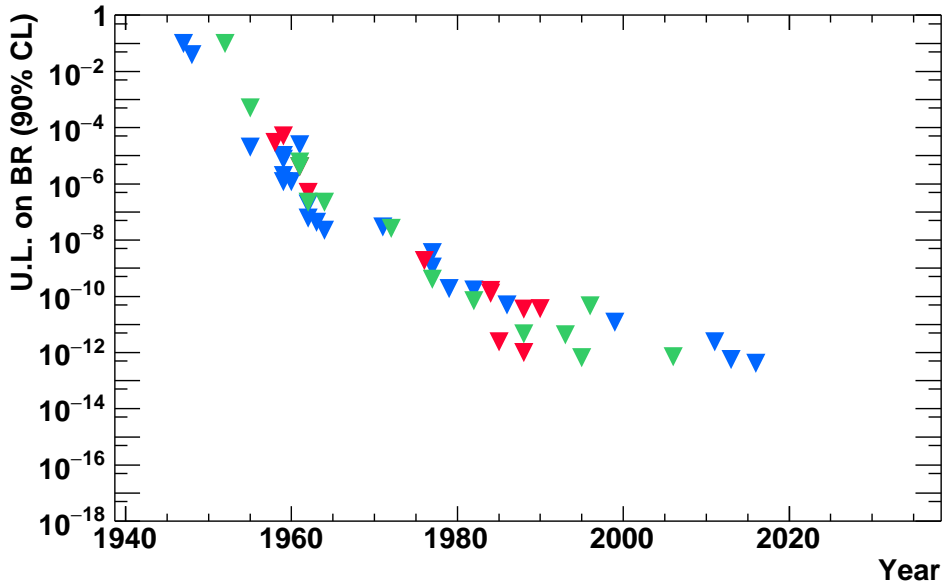

Figure 2.1: Development of the upper limits on $\mu \to e\gamma$ (blue), $\mu N \to eN$ (green), and $\mu \to 3e$ (red).

2.2.1 $\mu \to e\gamma$ decay in the SM

In the SM $\mu \to e\gamma$ decay is forbidden. However the discovery of the neutrino oscillation tells us non-zero mass of the neutrino and thus lepton flavor is not conserved. This result can be implemented to the SM in the simplest way and in that case a non-zero branching fraction of the $\mu \to e\gamma$ decay is calculated as [6, 7],

$$\mathcal{B}(\mu \to e\gamma) = \frac{\Gamma(\mu \to e\gamma)}{\Gamma(\mu \to e\nu\bar{\nu})} \tag{2.1}$$

$$= \frac{3\alpha}{32\pi} \left| U_{\mu i} U_{ei} \frac{m_i^2}{M_W^2} \right|^2 \tag{2.2}$$

$$= \frac{3\alpha}{32\pi} \left| \Sigma_{i=2,3} U_{\mu i}^* U_{ei} \frac{\delta m_{i1}^2}{M_W^2} \right|^2 \tag{2.3}$$

By substituting measured values [8] for U and δm_{i1}^2, the branching fraction is obtained as.

$$\mathcal{B}(\mu \to e\gamma) \leq 10^{-54}. \tag{2.4}$$

It is too small to be detected by experiments in near future.

2.2.2 $\mu \to e\gamma$ decay in BSMs

While the SM does not allow the $\mu \to e\gamma$ decay, many BSMs predict the decay with the large branching fraction around the current limit obtained by experiments. Especially in most cases of SUSY models, in general, the new source of the flavor mixing in mass matrices of the SUSY particles induces the cLFV including the $\mu \to e\gamma$ decay. The following demonstrates some of the attractive models induce the $\mu \to e\gamma$ decay.

SU(5) SUSY GUT

The SU(5) SUSY grand unified theory (GUT) is the model which unifies the gauge groups of $SU(3)_c$, $SU(2)_L$, and $U(1)_Y$ into a single SU(5) group at the order of 10^{16} GeV energy scale. In this model the cLFV is induced by the off-diagonal elements of the mass matrix of the SUSY lepton partners (sleptons) when the matrix of the SM leptons is diagonalized. That is when

$$V_R y_e V_L^\dagger = \text{diagonal}, \tag{2.5}$$

the off-diagonal elements for the right handed sleptons are given as [9]

$$(m_{\tilde{e}_R}^2)_{ij} \simeq -\frac{3}{8\pi^2}(V_R)_{i3}(V_R)_{j3}^* |y_u^{33}|^2 m_0^2 (3 + |A_0|^2) \ln \frac{M_P}{M_G}, \tag{2.6}$$

where M_P is the reduced Planck mass; M_G represents the GUT scale; and m_0 and A_0 are the universal scalar mass and trilinear coupling. Fig. 2.2 shows the possible Feynman diagrams induced by this off-diagonal elements.

SUSY Seesaw

Tiny neutrino mass is also a question for which we do not have any explanation. The seesaw mechanism [10–13] provides a natural explanation by introducing the Majorana mass term of right-handed neutrinos. When the Majorana neutrinos are included, two
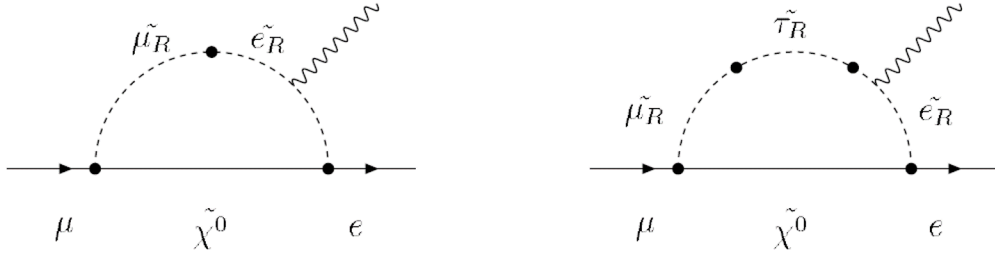
Figure 2.2: Feynman diagrams inducing $\mu \to e\gamma$ in SU(5) SUSY GUT. [9]

Yukawa coupling matrices appear in the lepton sector to couple the right-handed neutrino supermultiplets. Since the two matrices are independent, in SUSY seesaw model, the left-handed slepton mass matrix has off-diagonal element, which enhances cLFV.

In particular the high-scale SUSY, where the mass of the SUSY particles are in $O(10)$ TeV, predicts a large branching ratio of $\mu \to e\gamma$ of 10^{-13}–10^{-14} [14]. The recent results of no observation of the SUSY particles in the energy frontier experiment at the LHC and light Higgs mass of 126 GeV favor the high-scale SUSY.

Chapter 3

MEG II Experiment

In this chapter an overview of the MEG II experiment will be described. At the beginning the principle and requirements of the experiment will be introduced. Then the beamline used by MEG II will be described in the second section, and finally the detectors in MEG II in the third section.

3.1 Principle of $\mu \to e\gamma$ Search

The signal can be identified simply because the decay is a two-body decay, whereas the backgrounds arise from an accidental coincidence of uncorrelated positrons and photons, called accidental background, and a four-body decay of muons, called physics background. The schematic of the signal and the two backgrounds are shown in Fig. 3.1.
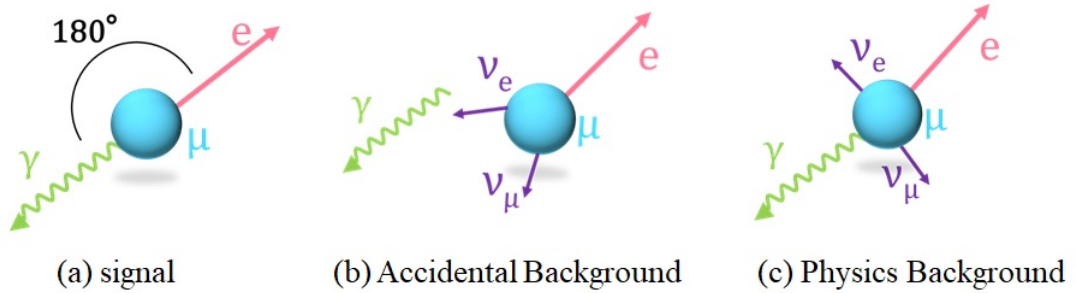

Figure 3.1: Drawing of $\mu \to e\gamma$ decay (a) and backgrounds (b, c).

3.1.1 Signal

The $\mu \to e\gamma$ decay is a simple two-body decay. A muon emits a back-to-back, mono-energetic, time coincident pair of a photon and a positron in the rest frame of the muon, that is

- $t_{e\gamma} = 0$

- $E_\gamma = E_e = m_\mu/2 = 52.8$ MeV

- $\Theta_{e\gamma} = 180°$

where $t_{e\gamma}$ is the time difference between the photon and the positron; E_γ and E_e are the energies of the photon and the positron, respectively; m_μ is the muon mass; and $\Theta_{e\gamma}$ is the opening angle between the photon and the positron.

The expected number of signals can be written with the branching fraction $\mathcal{B}$,

$$N_{sig} = R_\mu \times T \times \Omega \times \mathcal{B} \times \epsilon_e \times \epsilon_\gamma \times \epsilon_{cut} \tag{3.1}$$

where R_μ is the instantaneous muon intensity and T is the total acquisition time; Ω is the solid angle of the detector; ϵ_e and ϵ_γ are the detection efficiencies of positrons and photons respectively; and ϵ_{cut} is the efficiency of the event selection. All of these values except for the branching fraction given by the nature should be increased to observe the $\mu \to e\gamma$ decay.

3.1.2 Backgrounds

We utilize a positive muon beam; otherwise a nucleus in target material can form a muonic atom by capturing a negative muon. The decay from the muonic atom is no longer a two-body decay, which means we can not distinguish the signals kinematically.

Even though we use a positive muon beam, there are two backgrounds from muon decays of SM for $\mu^+ \to e^+\gamma$ search. One is the accidental background from the accidental coincidence of a positron from Michel decay ($\mu^+ \to e^+\nu_e\nu_\mu$) and a high-energy photon from any sources. The other background is a physics background from a radiative muon decay (RMD), $\mu^+ \to e^+\nu_e\bar{\nu}_\mu\gamma$.

Concerning muon decays in SM, the fraction of Michel decay mode is almost 100 % as shown in Tab. 3.1.

Table 3.1: The fraction of muon decay [8]

Decay Mode	Fraction
$\mu^- \to e^- \bar{\nu}_e \nu_\mu$	$\approx 100\%$
$\mu^- \to e^- \bar{\nu}_e \nu_\mu \gamma$	$(6.0 \pm 0.5) \times 10^{-8}$
$\mu^- \to e^- \bar{\nu}_e \nu_\mu e^+ e^-$	$(3.4 \pm 0.4) \times 10^{-5}$

Since the signal is characterized by the energies, the timing, and the opening angle of the emitted positron and photon as discussed above, the dependence of the backgrounds fraction per muon decay on these observables should be considered. In the following discussion, the positron and photon energies normalized to a half of the muon mass, $x = 2E_e/m_\mu$ and $y = 2E_\gamma/m_\mu$, and the opening angle, $z = \pi - \Theta_{e\gamma}$, are used. The effective partial branching fractions of the backgrounds are defined for the signal region of the $\mu^+ \to e^+\gamma$ search. Taking $\delta t_{e\gamma}$, δx, δy, and δz [1] to be the ranges of the signal region for the corresponding observables, the interesting region can be written as,

$$\begin{cases} 1 - \delta x \le x \le 1 + \delta x & \text{(3.2a)} \\ 1 - \delta y \le y \le 1 + \delta y & \text{(3.2b)} \\ 0 \le z \le \delta z & \text{(3.2c)} \\ -\delta t_{e\gamma} \le t_{e\gamma} \le \delta t_{e\gamma} & \text{(3.2d)} \end{cases}$$

---

[1]Considering the positron mass, the maximum range of y is $1 - \sqrt{r}$ and that of x is $1 + \sqrt{r}$ where $r = (m_e/m_\mu)^2$. However the effect is small enough to be ignored compared with the resolutions in principle.

As a reference the performance of the MEG experiment which set the most stringent upper limit on the branching ratio of $\mu \to e\gamma$ decay is shown in Tab. 3.2. Taking 90% of signal region is covered, which can be obtained by multiplying σs by 1.64, the signal region can be obtained as,

$$
\begin{cases}
\delta x \approx 0.015 \\
\delta y \approx 0.019 \\
\delta z \approx 20 \text{ mrad} \\
\delta t_{e\gamma} \approx 200 \text{ ps.}
\end{cases}
\tag{3.3}
$$

Table 3.2: Resolutions (in σ) in the MEG experiment [1]. The fractions are shown in parentheses when resolutions changed event by event.

Observables	Resolutions (σ)
Photon Energy (σ_{E_γ})	2.3% (fraction: 42%), 1.6% (58%)
Positron Energy (σ_{E_e})	330 keV (82%), 1.1 MeV (18%)
Opening Angle θ ($\sigma_{\theta_e\gamma}$)	15.0-16.2 mrad
Opening Angle ϕ ($\sigma_{\phi_e\gamma}$)	8.9-9.0 mrad
Time ($\sigma_{t_e\gamma}$)	122 ps

Physics Background

The positron and photon from RMD mimic a $\mu^+ \to e^+\gamma$ signal. They are emitted simultaneously and, moreover, when little momentum is carried off by the neutrinos, the positron and photon are emitted like back-to-back with the momentum close to that of the signal. RMD branching the fraction can be written in the V−A interaction as [9],

$$
\begin{aligned}
d\mathcal{B}(\mu^+ \to e^+\bar{\nu}_\mu\nu_e\gamma) = \frac{\alpha}{64\pi^3}\beta dx\frac{dy}{y}d\Omega_e d\Omega_\gamma [&F(x,y,d) \\
&-\beta\vec{P}_\mu \cdot \hat{p}_e G(x,y,d) \\
&-\vec{P}_\mu \cdot \hat{p}_\gamma H(x,y,d)],
\end{aligned}
\tag{3.4}
$$

where $d\Omega_e$ and $d\Omega_\gamma$ are solid angles of the emitted positron and photon with energy intervals of dx and dy respectively; $\vec{P}_\mu$ is the vector of muon polarization; $\hat{p}_e$ and $\hat{p}_\gamma$ are the unit vectors of a positron and a photon momenta defined by $\hat{p}_e \equiv \vec{p}_e/|\vec{p}_e|$ and $\hat{p}_e \equiv \vec{p}_e/|\vec{p}_e|$ as $\vec{p}_e$ and $\vec{p}_\gamma$ are momenta of a positron and a photon; β is defined as $\beta \equiv |\vec{p}_e|/E_e$; and d is given by $d \equiv 1 - \beta\hat{p}_e \cdot \hat{p}_\gamma$. $F(x,y,d)$, $G(x,y,d)$, and $H(x,y,d)$ are given in Appendix A of [9].

As discussed above, an RMD decay mimics a $\mu^+ \to e^+\gamma$ signal when $x \approx 1$, $y \approx 1$, and $z \approx 0$. The background branching fraction in an experiment depends on its resolutions of x, y, and z, and can be calculated by integrating Eq. 3.4 over Eq. 3.2a, Eq. 3.2b, and Eq. 3.2c,

$$
d\mathcal{B}_{RMD}(\mu^+ \to e^+\bar{\nu}_\mu\nu_e\gamma) = \int_{1-\delta x}^{1+\delta x}dx\int_{1-\delta y}^{1+\delta y}dy\int_0^{\delta z}dz\frac{dB(\mu^+ \to e^+\bar{\nu}_\mu\nu_e\gamma)}{dxdydz}.
\tag{3.5}
$$

The MEG experiment [1], which is the most recent experiment of $\mu \to e\gamma$ search, calculated the effective branching fraction as shown in Fig. 3.2 (b). Since the observed

shape of $dB(\mu^+ \rightarrow e^+\bar{\nu}_\mu\nu_e\gamma)$ is smeared by the detector resolutions in the experiment, Eq. 3.4 is folded with the detector responses in their calculation. They set the upper edges for E_e, and E_γ to 53.5 MeV corresponding to 1.0127 in x and y, and $\cos\Theta_{e\gamma}$ to -0.9996 as ~ 0.0283 in z instead of their detector resolutions and show the effective branching fraction as the function of the lower edges for E_e and E_γ of the signal region. In MEG the energy resolutions of positron (σ_{E_e}) and photon (σ_{E_γ}) are 330 keV[1] and 2.3%, respectively. The partial branching ratio in $52.5 < E_e < 53.5$ MeV and $52.0 < E_\gamma < 53.5$ MeV is,

$$d\mathcal{B}_{RMD}(\mu^+ \rightarrow e^+\bar{\nu}_\mu\nu_e\gamma) \sim 1 \times 10^{-14} \tag{3.6}$$

This level of background is not such a large number but not negligible for a $\mu \rightarrow e\gamma$ search going down its sensitivity to $\mathcal{O}(10^{-14})$ while it is negligible in MEG in which the single event sensitivity is $(5.84 \pm 0.2) \times 10^{-13}$. This background can be reduced by improving detector resolutions for the opening angle and momenta.
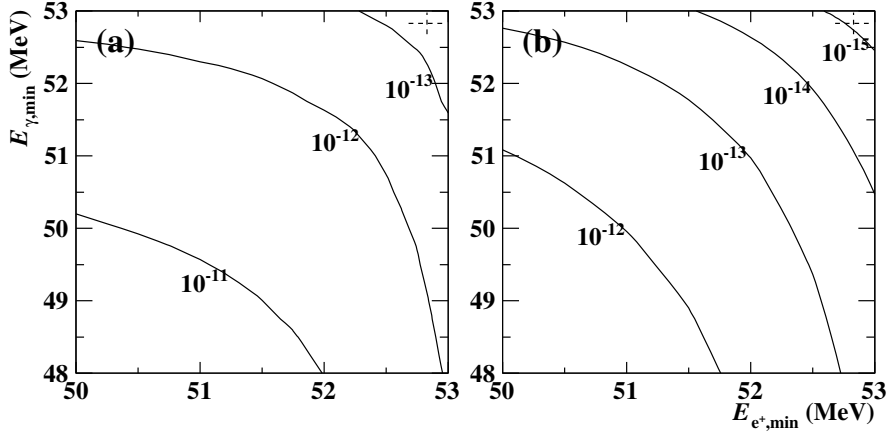

Figure 3.2: Effective branching ratios of the backgrounds in the MEG experiment [1]. The kinematic windows are defined by $E_{e^+,\min} < E_e < 53.5$ MeV, $E_{\gamma,\min} < E_\gamma < 53.5$MeV, $|t_{e\gamma}| < 0.24$ ns and $\cos\Theta_{e\gamma} < -0.9996$. (a) Accidental background (b) RMD background calculated by theoretical branching ratio (Eq. 3.5) smeared by MEG detector responses.

Accidental Background

The accidental background is the dominant background in a high intensity environment. Uncorrelated positron and photon can mimic the $\mu^+ \rightarrow e^+\gamma$ signal by an accidental coincidence when their momenta are around the signal momentum of 52.8 MeV.

The source of the background positron is a Michel positron. Its momentum is around the signal momentum when the opening angle of the two neutrinos are small. On the other hand, the photon background sources come from an annihilation in flight of a positron (AIF) and an RMD. Fig. 3.3 shows the photon background rate in the MEG experiment [15] and indicates that AIF and RMD are the dominant background of photon. In addition accidental pileup of photons is also another source of background.

The effective branching fraction of the accidental background ($\mathcal{B}_{acc}$) to one muon can be written with an instant intensity of muon beam (R_μ) as,

$$\mathcal{B}_{acc} = R_\mu \cdot f_e^0 \cdot f_\gamma^0 \cdot \frac{(\delta z)^2}{4} \cdot (2\delta t_{e\gamma}), \tag{3.7}$$

---

[1]This is the core value. Tail component of $\approx 18\%$ is observed with $\sigma_{E_e} \approx 1.1$ MeV
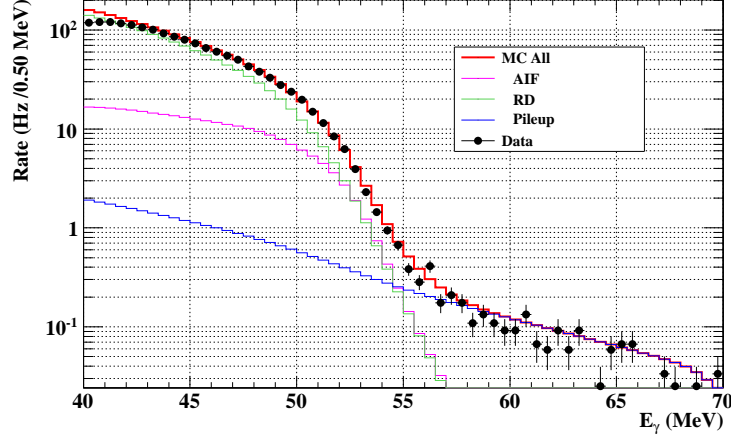
Figure 3.3: Trigger rate of photon background in MEG experiment [15].

where f_e^0 and f_γ^0 are the integrated energy spectra of a positron and a photon within the signal region respectively. f_e^0 can be calculated by integrating the Michel positron energy spectrum given by Fig. 3.4 [16]. At the signal region $x \approx 1$ the spectrum is almost flat, therefore,

$$f_e^0 \approx 2(\delta x). \tag{3.8}$$

By contrast, f_γ^0 can be obtained by combining AIF and RMD gamma spectra. While the spectrum of AIF depends on material distribution in an experiment, that of RMD can be calculated by integrating Eq. 3.4 over all positron energy and opening angle, and Eq. 3.2b for photon energy. It is described in [17]. At first the result of the integration of the positron energy and the opening angle is,

$$dB(\mu^+ \to e^+ \bar{\nu}_\mu \nu_e \gamma) = [J_+(y)(1 + P_\mu \cos\theta_\gamma) + J_-(y)(1 - P_\mu \cos\theta_\gamma)] + \mathcal{O}(\sqrt{(r)})] \frac{dy}{y} d(\cos\theta) \tag{3.9}$$

where $J_+(y)$ and $J_-(y)$ are given by

$$J_+(y) = \frac{\alpha}{6\pi}(1 - y)[(3\ln\frac{1 - y}{r} - \frac{17}{2}) + (-3\ln\frac{1 - y}{r} + 7)(1 - y) \\ + (2\ln\frac{1 - y}{r} - \frac{13}{3})(1 - y)^2], \tag{3.10}$$

$$J_-(y) = \frac{\alpha}{6\pi}(1 - y)^2[(3\ln\frac{1 - y}{r} - \frac{93}{12}) + (-4\ln\frac{1 - y}{r} + \frac{29}{3})(1 - y) \\ + (2\ln\frac{1 - y}{r} - \frac{55}{12})(1 - y)^2]. \tag{3.11}$$

In the interesting region $y \approx 1$ the effect of $J_+(y)$ is much larger than that of $J_-(y)$ because $J_-(y)$ has the larger power of $(1 - y)$. The partial branching ratio integrated over 3.2b can be obtained as,

$$\begin{aligned} db_\gamma &= \int_{1-\delta y}^{1+\delta y} dy \frac{dB(\mu^+ \to e^+ \bar{\nu}_\mu \nu_e \gamma)}{dy} \\ &\approx \frac{\alpha}{4\pi}(\delta y)^2[\ln(\delta y) + 7.33](1 + P_\mu \cos\theta_\gamma) d(\cos\theta_\gamma). \end{aligned} \tag{3.12}$$

Assuming the unpolarized muon, $P_\mu = 0$, it can be written as,

$$b_\gamma \approx \frac{\alpha}{2\pi}(\delta y)^2[\ln(\delta y) + 7.33]. \tag{3.13}$$

In conclusion, assuming the photon from RMD as the dominant source of the photon background, the number of the accidental background can be written as

$$N_{acc} = R_\mu \times T \times \Omega \times \mathcal{B}_{acc} \times \tilde{\epsilon}_e \times \tilde{\epsilon}_\gamma \tag{3.14}$$
$$\propto R_\mu^2 \times T \times \delta y^2 \times \delta x \times \delta z^2 \times \delta t_{e\gamma}, \tag{3.15}$$

where $\tilde{\epsilon}_e$ and $\tilde{\epsilon}_\gamma$ are the detection efficiencies of background positrons and photons respectively, which have small difference from those of signals because of difference of the distribution of momenta, opening angle, and so on. Consequently, the background can be reduced by tightening the signal region of x, y, z, and $t_{e\gamma}$, while it is increased with the square of R_μ.

The effective branching ratio of the accidental background is estimated in the MEG experiment by using time side-band events. Fig. 3.2a describes it as a function of the minimum integral range of E_e and E_γ. In the MEG environment the partial branching fraction is obtained as,

$$\mathcal{B}_{acc} \sim \mathcal{O}(10^{-13}) \tag{3.16}$$

The partial branching ratio of the accidental background is one or two order of magnitude larger than that of RMD in 3.6 and is the dominant background with recent detector performance. This background level is not acceptable to achieve the sensitivity down to $\mathcal{O}(10^{-14})$. The reduction of the accidental background is essential for MEG II experiment.
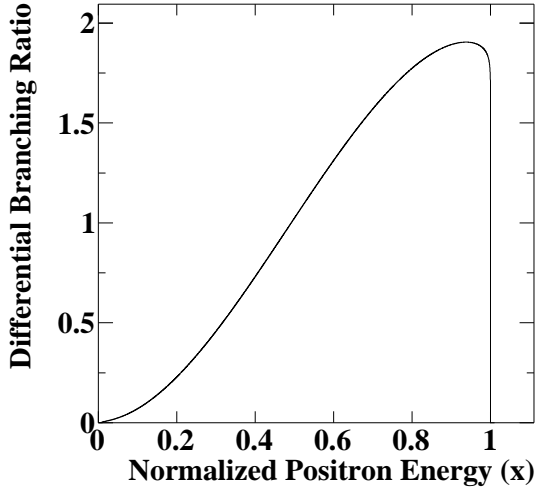

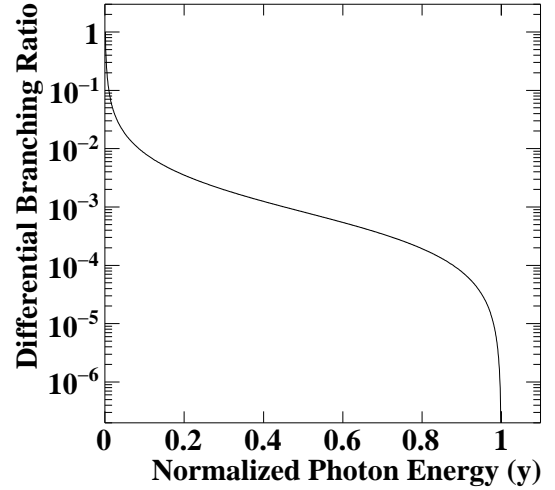Figure 3.4: Positron energy spectrum from Michel decay [16]

Figure 3.5: Photon energy spectrum

3.1.3 Requirements

The necessity of background reduction is described in the previous subsection. In particular, reducing accidental background, which is the dominant background, is essential.

There are several requirements for the $\mu \to e\gamma$ search. Firstly a high intensity direct current (DC) muon beam is required. Comparing Eq. 3.1 and Eq. 3.14, the number of the accidental backgrounds depends quadratically on the instant muon intensity while the signal events increases only in proportion to the instant intensity of muon beam. Hence a DC beam matches the experiment to acquire large statistics effectively with minimizing the accidental background.

Secondly, the detector improvement is equally important to reduce the background. Eq. 3.7 and Eq. 3.14 indicate that the improvement in resolutions of the momenta, and the opening angle and the time between a positron and a photon suppresses the background.

Furthermore we can make an effort to reduce the photon background source unlike the positron background which depends on only muon beam intensity. As explained above, photons of accidental background mainly come from RMD and AIF. To avoid the AIF, material should be minimized throughout the positron path. In addition, any kind of detector or analysis to identify the RMD and AIF also help to suppress the photon background. In summary, the requirements for the $\mu^+ \to e^+\gamma$ search are,

- High intensity DC muon beam

- Minimized material detectors having high performance for measurement of momenta, opening angle and time of positron and photon

3.1.4 MEG to MEG II

The requirements above are satisfied in the MEG experiment, which is why they achieved the highest sensitivity for the search in the world. A schematic of the MEG experiment is described in Fig. 3.6. The beam line employed by MEG is in Paul Scherrer Institut (PSI) and provides the most intense DC muon beam in the world. Muons are stopped in a target, and then emitted photons are detected in a liquid xenon calorimeter with which the positions, times, and energies are measured, and emitted positrons are bent by a superconducting magnet and their momenta, vertex and times are measured by a drift chamber and a timing counter. These detectors made it possible to yield the most stringent upper limit on branching ratio of $\mu^+ \to e^+\gamma$ of 4.2×10^{-13} (90 % confidence level) [1].

However further enhancement of the sensitivity is difficult in MEG because of the increase of the number of backgrounds as shown in Fig. 3.7. The figure indicates that the degree of the sensitivity enhancement becomes less with accumulation of the data and further data acquisition in MEG makes little sense. The upgrade of detectors is, therefore, mandatory to reach the sensitivity of $\mathcal{O}(10^{-14})$.

The key of the upgrade to MEG II is the maximum usage of the muon beam in PSI. Since the drift chamber could not operate in a highly radiation environment which induces discharge and unacceptable background level for the MEG detectors, the intensity of muon beam was limited and was reduced by a factor of 2-3 from the maximum intensity. We can exploit full intensity of the muon beam by

- Development of high rate tolerable positron spectrometer.

- Resolution improvement for all the detectors

Furthermore the MEG experiment had a poor detection efficiency ($\sim$40 %) of positron. The material between the drift chamber and timing counter, such as the drift chamber electronics and support, induced scattering of positrons before timing counter resulting in the poor efficiency and poor timing resolution at the positron side. Consequently,
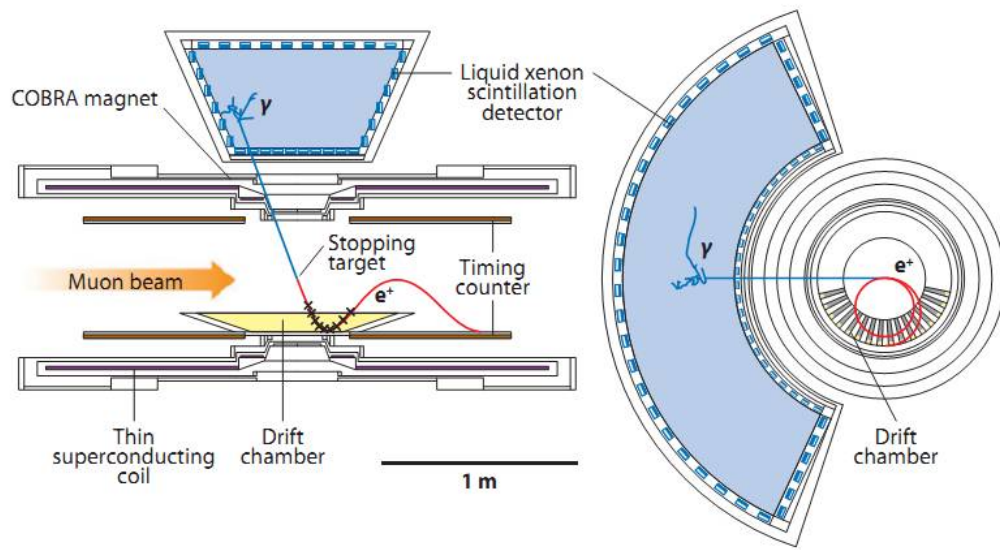
Figure 3.6: Schematic of the MEG experiment
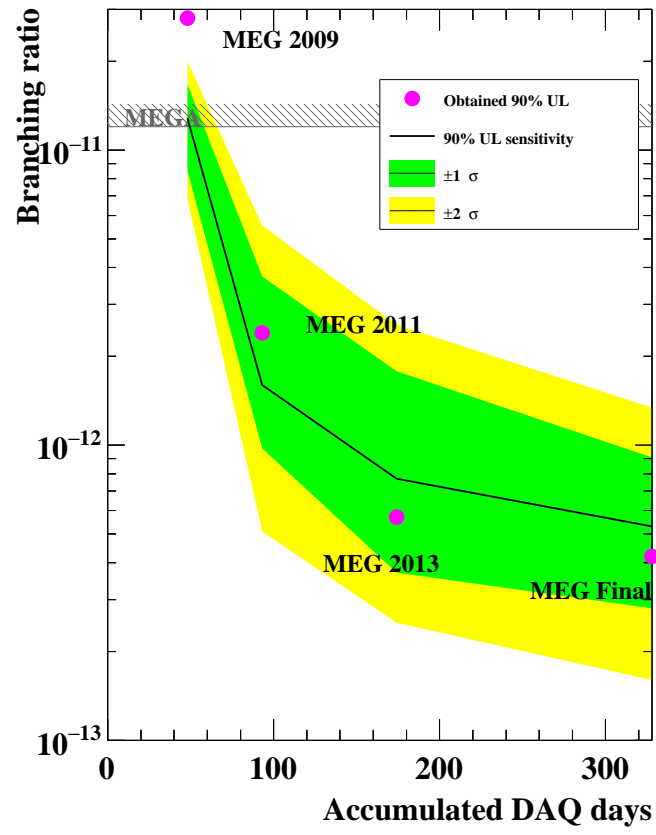
- Low mass positron spectrometer

is also required.

Figure 3.7: Sensitivity improvement in MEG.

3.2 Muon Beam in MEG II

To achieve an unprecedented sensitivity of the $\mu^+ \to e^+\gamma$ search, the requirements for the muon beam are:

- High intensity,

- DC,

- Low momentum muon

The key to a high intensity muon beam is using surface muon. This section will introduce a beamline from generation of the proton beam providing muon beam to the area for MEG II experiment. Overview of the beamline is shown in Fig. 3.8.

3.2.1 Proton Accelerators at PSI

Muon beams in PSI originate from the protons. The proton acceleration in PSI is suitable for production of high intense low momentum muon beams. Several reactions are relevant to generation of pions, which is the source of muons, such as $p + p \to p + n + \pi^+$, and $p + n \to n + n + \pi^+$. At least protons should have $\sim$280 MeV in the lab frame where one of the protons is at rest for these pion generation processes. Beyond the energy threshold of the pion generation, the cross section increases continuously with the energy of the protons. Furthermore, when the proton energy is beyonds $\sim$580 MeV, double pion creation, such as $p + n \to p + n + \pi^+ + \pi^-$ and $p + p \to n + n + \pi^+ + \pi^+$, can occur. On the other hand, the pion generated from higher energy proton beam tends to have larger kinetic energy. Concerning low momentum muon production, the production peak is obtained around 500 MeV of proton energy [18].

PSI proton accelerator pushes up the proton energy to 590 MeV. There are three stages of the proton accelerators before the muon production. At the beginning Cockcroft-Walton pre-accelerator generates protons from a hydrogen source and accelerate them up to 870 keV. The pre-accelerated protons are injected into a separate-sector isochronous cyclotron called Injector II , which consists of four magnets and two main RF cavities ($\sim$ 400 kV) and two third-harmonic cavities ($\sim$30 kV) [19]. The picture is shown in Fig. 3.10. This first cyclotron delivers 2.4 mA beam to the main ring cyclotron by accelerating energy up to 72 MeV. The second cyclotron is composed by five cavities including four main RF cavities and eight magnets (schematic is shown in Fig. 3.12), and accelerates the beam up to 590 MeV and provides 2.2 mA beam, that is 1.3 MW beam. Frequency is 50 MHz and bunch width is 0.3 ns.

3.2.2 Muon Production and πE5 Beamline

The accelerated protons reach to two graphite target, Target M and Target E, sequentially and the rest protons ($\sim$70%) arrive the Spallation Neutron Source target or a beam dump. Thickness of target M is 5 mm and that of target E is 40 mm along beam axis and they rotate to avoid being heated too much by high energy proton beam. They are attached seven beamlines having variety momentum and intensity and providing pion, proton, and muon beams. In the targets, pions are produced as discussed above and generate muons by $\pi^+ \to \mu^+\nu_\mu$ decay. The lifetime of a pion is $\sim$ 26 ns at the rest and that of muon is 2.2 μs, while the pulse of the proton beam is 20 ns. Therefore produced muon beam is DC beam effectively. Since πE5 beamline providing the highest intensity muon beam in the seven beamlines, it is employed for MEG II experiment.

Figure 3.8: Overview of Beamlines in PSI. (1) Cockcroft-Wolton injector. (2) Injector. (3) 590 MeV Ring Cyclotron. (4) Target E. πE5 area is encircled in red.
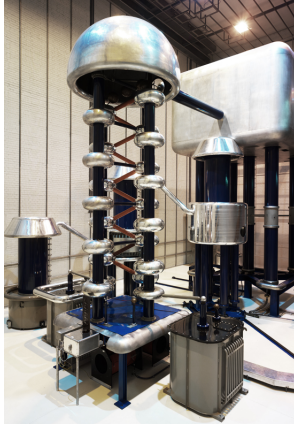
Figure 3.9: Cockcroft-Wolton linear accelerator [20]. It is the first stage of the proton acceleration. Condensers linked by orange bars produce the charge accumulation only upwards.
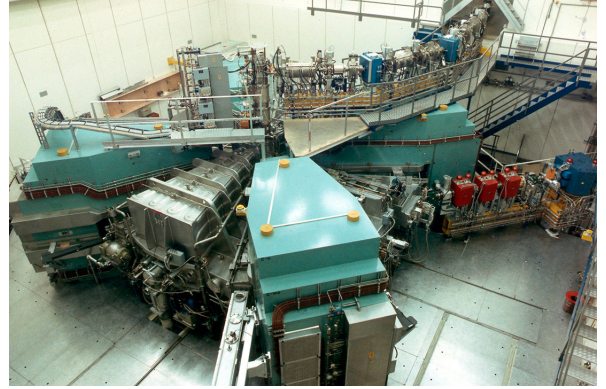

Figure 3.10: Injector2 [21]. Magnets are turquoise-colored and silver-colored staffs inter magnets are resonators.

πE5 beamline is the most backward beamline with respect to the primary proton beam from Target E. The angle is 165°, which is tuned for surface muon [23] originating from pion stopping "skin" of a production target and decaying at rest. Muons generated from pions at the rest have monochromatic momentum of 29.8 MeV/c and are $\sim$100 % polarized. The muons with small momentum can be stopped easily on a thin target. Component of πE5 beam line is shown in Fig. 3.15. It consists of bending magnets, quadrupoles, hexapoles, and slits. They determine momentum and/or acceptance. Behind the second bending magnet AST momentum flux of Fig. 3.13 is obtained. Enhancement of μ^+ flux around 29.8 MeV/c is shown in the figure. [1] In MEG II sub-surface muon is also used.

3.2.3 Beam Transport System after πE5 Beamline

After πE5 beamline, there is the transport system to a stopping target in the MEG II detector. It is composed by first quadrupole triplet magnet (Triplet1), a cross-field separator (Wien-filter), second quadrupole triplet magnet (Triplet2), and Beam Transport Solenoid (BTS) as shown in Fig. 3.15. The two set of magnets and the separator separate between surface muons and positron contamination from Michel decay or pair creation of a photon from π^0 decay in the production target. In front of MEG II detectors the final adjustment of muon momentum is performed by BTS.

3.2.4 Beam Intensity in MEG II

In MEG II beam intensity increases to $\sim$7$\times$10^7 μ^+/s, which is two times higher that in MEG, 3$\times$10^7 μ^+/s. The intensity in MEG is much lower than the maximum ability of πE5 beam line, $\sim$ 10^8. Positron spectrometer in MEG could not tolerate high rate hits, so it limited the beam intensity. A beam blocker decreased the intensity. Development of the detectors in MEG II enables us to utilize almost full beam ability. Though backgrounds

---

[1]Negative pions are captured by nuclei before their decaying. Therefore no peak can be observed in negative muon flux.
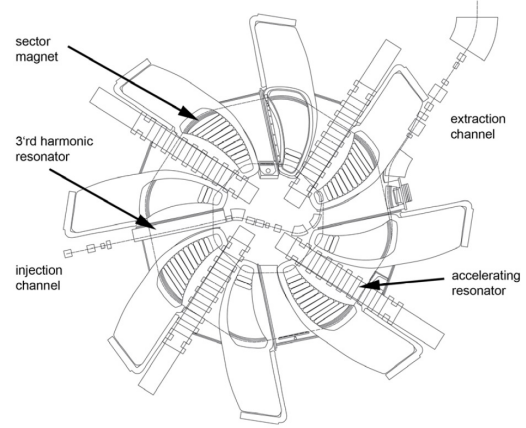
Figure 3.11: Picture of Ring Cyclotron

Figure 3.12: Schematic of main ring cyclotron in PSI [22]

also increases as Eq. 3.7 with higher beam intensity, they are also reduced by detector development.

3.2.5   Muon Stopping Target in MEG II

Muon stopping targets is placed at the center of COBRA magnet. It is required to perform high muon stopping efficiency with low material to avoid multiple scattering of emitted positrons, photon conversion from RMD, and background photon yield from positron bremsstrahlung, or annihilation in flight (AIF). Moreover for target alignment reconstruction of the positron vertex is required. In the MEG experiment polyethylene/polyester target is placed with slant angle of 20.5° and the target has six holes as shown in Fig. 3.16 to reconstruct vertex and check the target alignment. However they found the deformation of the target and it could not be monitored or corrected. Since reconstructed positron trajectory is projected on the target plane, the deformation makes a large error of positron direction. As a result in MEG largest systematics error of 13 % came from the deformation in their final result while the total contribution from the other items is less than 1 % [1]. Therefore the target in the upgraded experiment MEG II should be mechanically stable and monitoring system is also needed.

For the new target several materials are tested as shown in Tab. 3.3 [24]. In these materials a scintillator plate is a strong candidate, because it is large advantage that the beam intensity and profile can be measured by catching scintillation light by CCD camera. It was already tested and sub-millimeter level of beam image was obtained.

To monitor the target deformation photogrammetric monitoring is planned and tested. Dots are printed on target and monitored by CCD camera. The picture is shown in Fig. 3.17. Furthermore laser survey by putting low-mass cubic ball on target frame, and coordinate measurement machine are also planned.
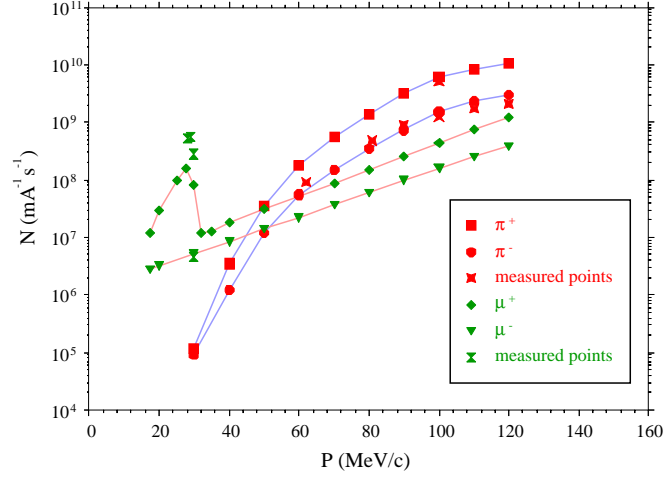
Figure 3.13: Muon and pion flux in πE5

Table 3.3: The parameters of candidate target [24]. Inclination angle are set $15.0°$ and degrader thickness is 350 μm.

Material	Thickness (μm)	Thickness (X_0)	Density (g cm^{-3})	Stop Efficiency (%)	Multiple Scattering (mrad)	
					μ^+[18MeV]	e^+[52MeV]
CH$_2$	140	2.8×10^{-4}	0.893	83	52.0	3.0
Be	90	2.6×10^{-4}	1.848	83	49.3	2.9
Mylar	100	3.5×10^{-4}	1.390	84	58.5	3.4
Scint. PVT	130	3.1×10^{-4}	1.032	84	54.5	3.2
Diamond	40	3.3×10^{-4}	3.515	81	56.8	3.3
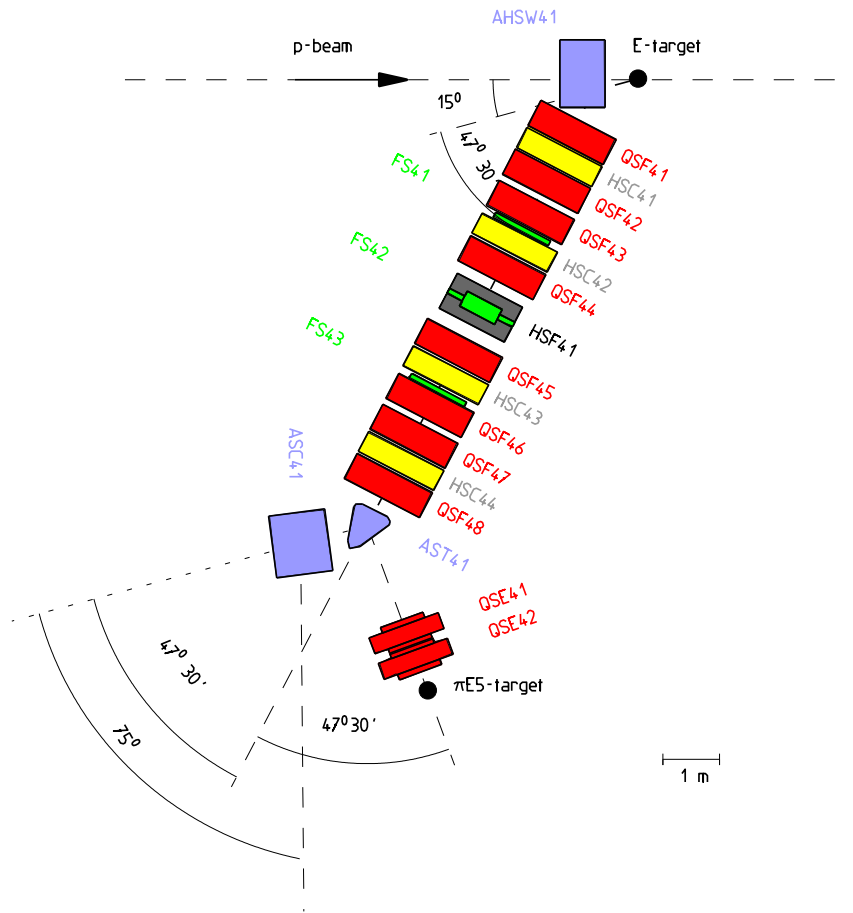
Figure 3.14: PiE5 Beam line
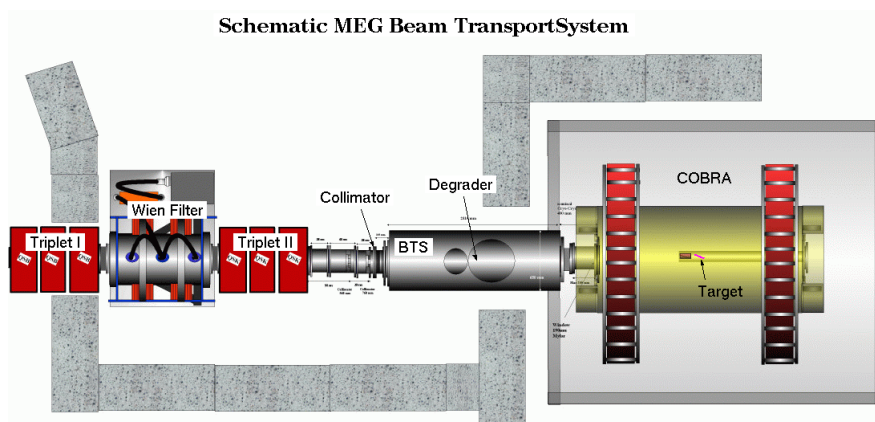
Figure 3.15: Beam transport system

Figure 3.16: Target in MEG. There
are six holes for vertex study and
target alignment.
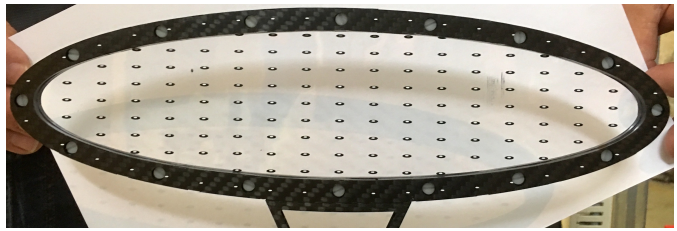
Figure 3.17: Scintillator target with marking
for monitoring.
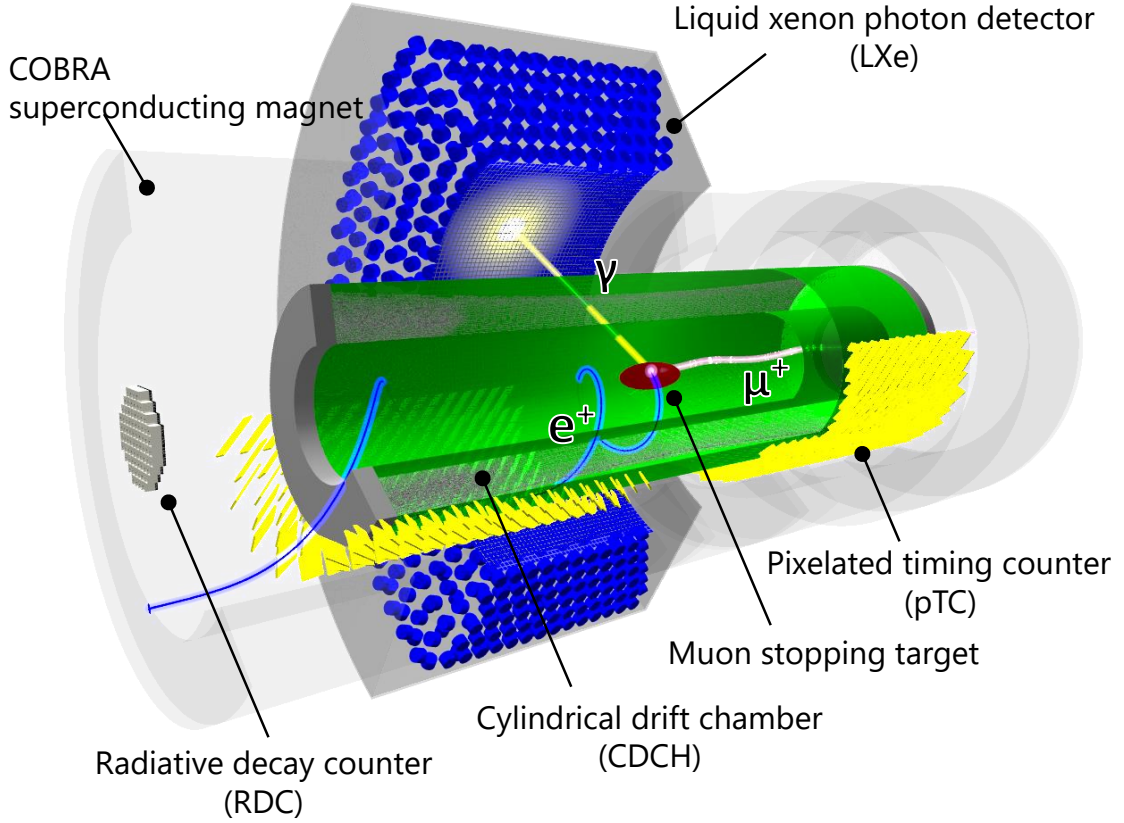
3.3 Detectors

Figure 3.18: MEG II overview

Overview of the MEG II detectors is shown in Fig. 3.18. The global coordinates in MEG II are defined with the target center as the origin; z is along the beam direction, y is assigned an axis from bottom to top direction, and x is the rest axis in the right-handed rectangular coordinate. A muon is stopped on target placed at center of the COBRA coordinate. We also define the θ as the polar angler from z-axis, and the ϕ as an azimuthal angle.

A muon is stopped on the target and emits a gamma-ray and a positron in the signal decay. The gamma-ray is detected by a liquid xenon (LXe) photon detector. Position and time on first interaction point with LXe, and energy of gamma-ray are measured. It is C-shape detector which acceptance to whole solid angle is ∼11 %. On the other hand, a positron is bent by a special magnet called COBRA and measured by two detectors, wire drift chamber (DCH) and timing counter (TC), which acceptances cover the positrons emitted to opposite side from the gamma acceptance region. The DCH reconstructs positron trajectories, which is propagated to target plane and reconstruct the vertex and the direction on the target, while time of positrons is reconstructed by TC which consists of plastic scintillator with photo sensor readout. Flight time of photon to the interaction point in the LXe photon detector is reconstructed by the positron momentum and vertex reconstructed by DCH.

The overall concept of MEG II as described above is similar to that of MEG, so we reuse

the COBRA magnet and liquid xenon, and its cryostat. By contrast, the performance of every detectors of LXe, DCH, and TC are upgraded, especially DCH and TC are replaced with quite new ones. Furthermore a new detector, radiative decay counter (RDC), which idea is based on the background study in MEG is installed in the MEG II experiment. To reduce the background photon originated from RMD, a low momentum positron from RMD is tagged by RDC. In following sub sections, we will get into detail of each detector.

3.3.1 Positron Spectrometer

The positron spectrometer is one of most important detectors in MEG and MEG II. What we should consider is high background rate from Michel decay following the momentum distribution as shown in Fig. 3.4. The positron spectrometer should survive in the high rate environment. In MEG the unique magnet called COBRA was developed. The name is abbreviation of COnstant Bending RAdius. The magnet forces for the same momentum positron to have the same radius independent on its incident angle and sweep the positron away out of detector region quickly. Fig. 3.19 describes the principle of the COBRA magnet and the power of the background reduction is shown in Fig. 3.20. Owing to COBRA the hit rate in drift chamber region is decreased. Only the positrons having signal momentum reach to detectors and remain hits in only twice or three times turn. The trajectory of the bent positron is measured by drift chamber typically in the first or second turn and then the positron time is measured a positron timing counter composed of plastic scintillator readout by photo sensors typically in the second turn. The measured timing on the timing counter is translated to the time on a vertex by subtracting the flight time between the timing counter and the vertex, which reconstructed by DCH.

In the MEG II experiment, we reuse the COBRA magnet. On the other hand, totally new detectors are installed as a drift chamber and a timing counter. Upgrade concept of the positron spectrometer is shown in Fig. 3.21. In MEG positron scattering between DCH and TC made the efficiency and timing resolution of positron worse than expectation. The positron detection efficiency was 30 % while it was expected to be 65 %. The timing resolution was 107 ps which is composed of TC resolution of 76 ps and the flight time resolution of 75 ps. In MEG II, we will reduce the material between DCH and TC to avoid scattering by employing a single volume DCH unlikely the MEG DCH, which was moduled. As a results the contribution of the flight time reconstruction is expected to be reduced down to 15 ps.
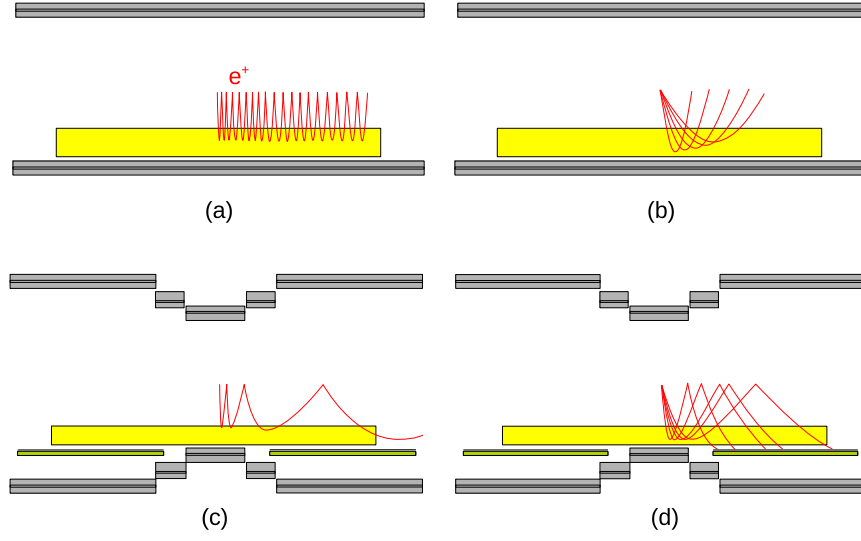
Figure 3.19: Principle of COBRA magnet. The region colored by yellow is detector region. Normal solenoid magnet a positron hits a detector many times (a), while the COBRA magnet sweep it away quickly (c). Positrons with different emitting angles have different bend radius in the field of a solenoid magnet (b). COBRA magnet bends the same momentum positrons in the same radius (d).
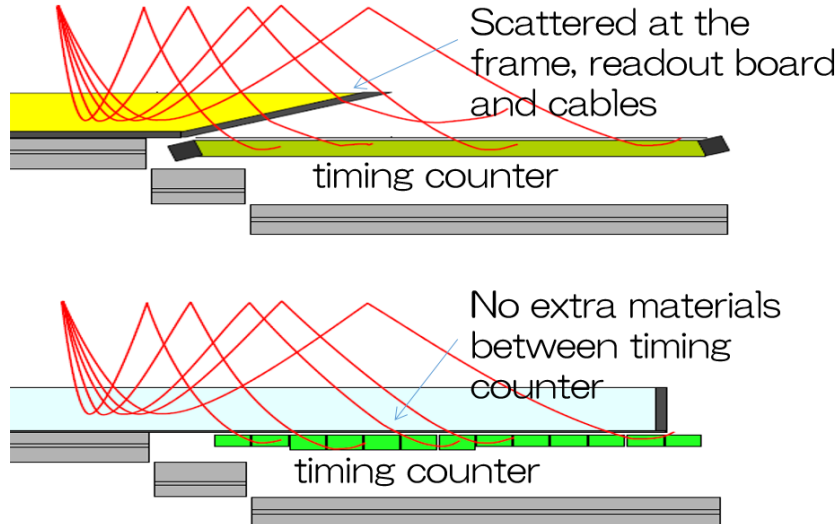

Figure 3.21: Schematic of MEG and MEG II positron spectromenter.

Here, detailed description of the COBRA magnet and the drift chamber will be given
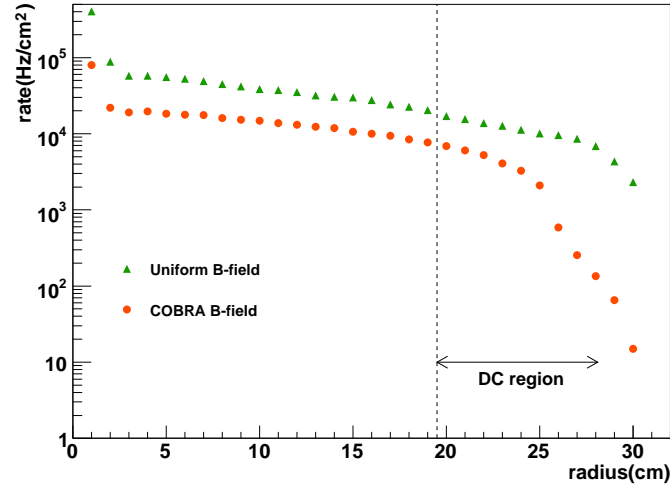
Figure 3.20: Michel positron rate ($/cm^2$) as a function of radius in the COBRA magnetic field with comparison to that in uniform magnetic field. The muon stopping rate is assumed 3×10^7/s which corresponds to the rate in MEG.

and the brief concept of the upgrade of the timing counter will be shown and the next chapter will take over in detail.

COBRA Magnet

The COBRA magnet is a super conducting magnet which consists of two central coil, two gradient coils, and two end coils. Each coil has different radius and length as shown in Fig. 3.22. Since photon should penetrate the magnet wall to the LXe detector, the wall should be as thin as possible, which is 0.197 X_0 equal the penetration of 85 % signal photons.
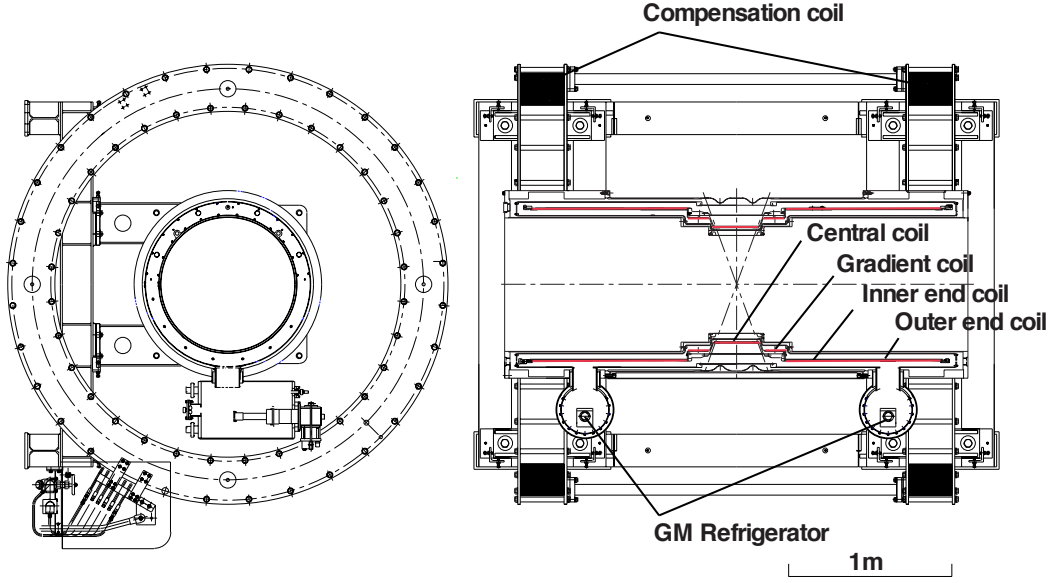
Figure 3.22: Schematic of COBRA magnet.

Its magnetic field is 1.27 T at the center and decreasing down to 0.49 T with $|z|$ increase as shown in Fig. 3.23. However PMT for LXe photon detector loose their gain with strong magnetic field of more than $\sim$50 Gauss. Therefore compensation coils is also placed as shown in Fig. 3.22. Fig. 3.24 shows the magnetic field in the experiment site, which is successfully reduced by the compensation coils.
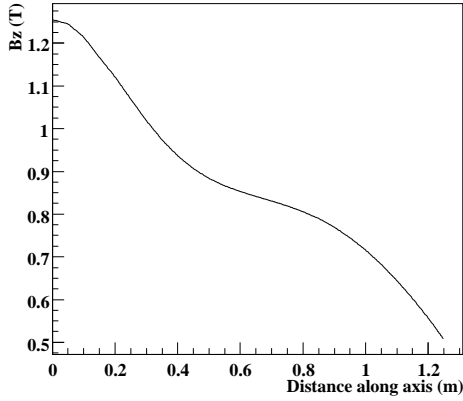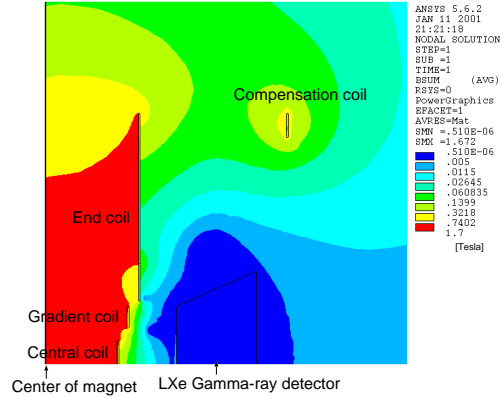

Figure 3.23: Profile of the COBRA magnetic field.

Figure 3.24: Contour of the magnetic field around photon detector.

Drift Chamber

Structure

A tracker in MEG II is single volume wire drift chamber. Sketch of the DCH structure is shown in Fig. 3.25. Inner radius is 17 cm, and outer 29 cm. Length is optimized to avoid multiple scattering between DCH and TC which was the reason of poor positron detection

efficiency in the MEG experiment. In case of the MEG II DCH, as indicated in Fig. 3.26, DCH endcap has largest effect on efficiency of TC and longer DCH, more than 180 cm, is better for the efficiency as shown in Fig. 3.27. In conclusion, we decided 191 cm length.
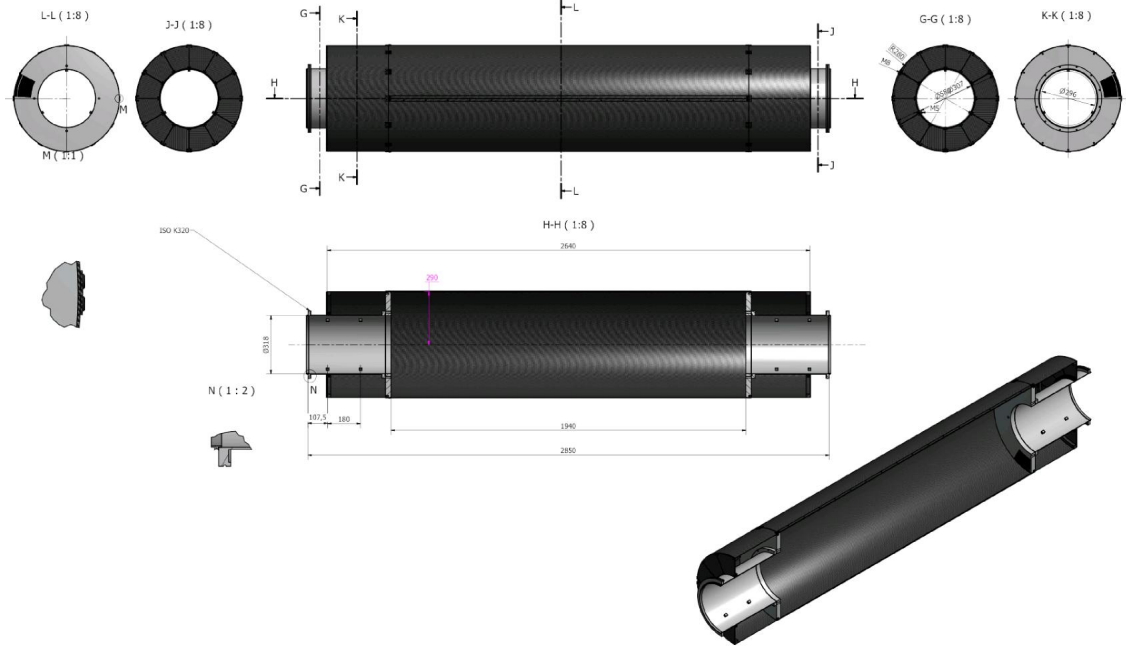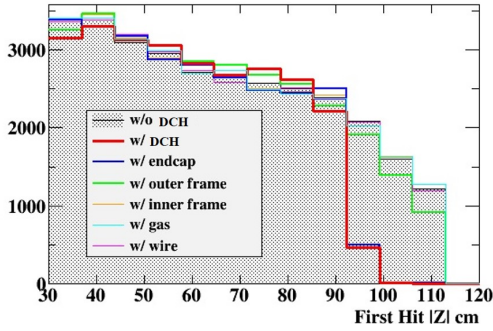

Figure 3.25: DCH structure.

Figure 3.26: Dependence of TC hit count on z coordinate with several DCH material in MC. DCH length is fixed at 90 cm.
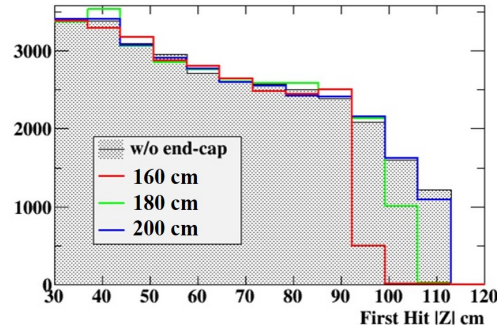

Figure 3.27: TC hit count dependence on z coordinate with several DCH length. Length is written as active length of DCH.

The volume of the DCH is enclosed by a carbon fiber support structure for outer radius, aluminum Mylar foil for inner radius to separate from target region filled with pure helium, and end-plate attached PCB for wires and PEEK$^{®}$ spacer (see Fig. 3.29) for outer along z-coordinate. The end-plate are helm shape gold-plated aluminum ones with 30 mm thickness as shown in Fig. 3.28.
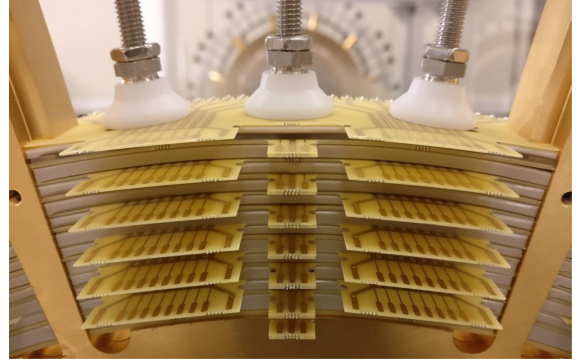
Figure 3.28: Picture of end-plate.

Figure 3.29: Picture of end-plate with PCB and spacer during wiring each layer by using fixing tool shown in top of the picture.

Wire Configuration

The DCH consists of 13056 wires and low mass mixed gas of helium and isobutane (C_4H_{10}) in the ratio of 90:10. These materials correspond to $\sim 1.58 \times 10^{-3}$ X_0 of radiation length for single turn. As shown in Fig. 3.31, the wires compose 10 drift cell layers each of which divided into 12 sectors per 30°. We employ alternating stereo angles for wiring. In Fig. 3.30 configuration of stereo angle is drown. The stereo angle can be written as,

$$\varepsilon_i = \arctan(\frac{2r_i}{L}\sin\alpha_i), \tag{3.17}$$

where stereo angle is ε_i in ith layer; L is DCH length; α_i is angle projected to end-plate; and r_i is radial position of a wire. We choose $\alpha = 30°$, therefore the angles are approximately from 6.0° to 8.5° at several radii. The sign of the stereo angles are chosen both of positive and negative to make two criss-crossing planes, which allow to reconstruct position along z-axis precisely. The size of single cell is almost square from 6.6 mm to 9.0 mm depending on the radius. The center of the cell is sense wire made of gold plated tungsten which diameter is 20 μm and silver plated aluminum field wires with 40 μm diameter surround the sense wires.

Status

DCH is now being prepared towards 2018 run. However during DCH construction we found broken wires several times (totally 14 wires are broken) from July to September in 2017 due to chemical contaminants in wires. The contamination induced the wire corrosion, which was accelerated by tension. After finding the problem we decided to loose the wire stretching from +4 mm to +3.5 mm. In addition, since humidity also influences chemical reaction strongly, that of small volume around DCH is controlled down to 20 % against wire broken, while before that humidity in only whole clean room was controlled down to 60 %. In parallel we are planning construction of second DCH with alternative wires. Its financial support is already secured and study on wire is on going. However first DCH will be installed to check all the procedures for its operation. Wiring of first DCH was stopped after finishing 9th layer in February 2018 by accepting efficiency reduction of $\sim$10 % which is expected by MC study. First one will be installed by end of July.
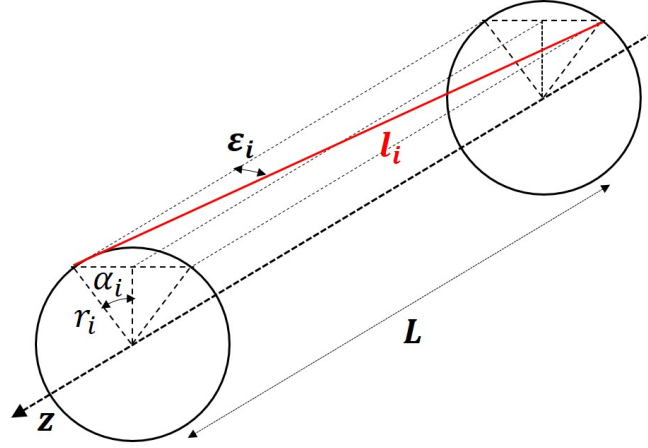
Figure 3.30: Schematic of stereo angle (ε_i) of wire in ith layer. L is DCH length; l_i wire length; α_i angle projected to end-plate; and r_i radial position of a wire

Timing Counter

The timing counter (TC) measures the positron time after DCH tracks the positrons. It placed outer DCH and inner COBRA both of the upstream (US) and the downstream (DS). The TC is segmented by 512 counters in total. Fast plastic scintillator in TC detects the positron and its scintillation light is read out by the 12 SiPMs attached at the both end. The size of the single scintillator counter is $120\times40\times5$ mm^3 or $120\times50\times5$ mm^3 depending on the position. It is totally new detector from MEG which used the 30 scintillator bars ($40\times40\times800$ mm^3) attached two PMTs at the both ends. As a result, we can overcome the higher positron hit rate on the TC. The next chapter will explain the TC in detail.

Status

TC construction and installation were completed in November 2017. Its engineering run with full counters and laser calibration system was also curried out. In following three chapter the detailed result will be discussed. Maintenance of dead fibers and counters is on going towards run in 2018.
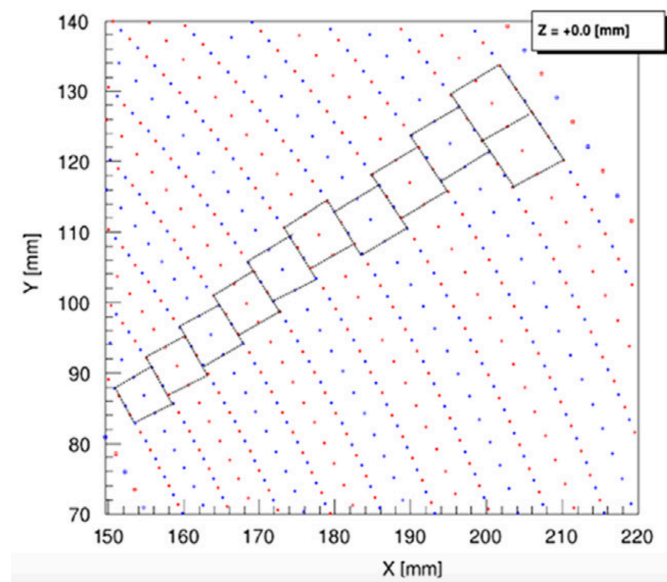
Figure 3.31: Configuration of cells in the drift chamber at $z = 0$.

3.3.2 Photon Detector

Photon are measured by LXe as scintillator in the MEG and the MEG II experiment, not by a magnetic spectrometer reconstructing converted electron-positron pair. In the LXe detector, 900 l of liquid xenon is surrounded by photo sensors as shown in Fig. 3.32. As photo sensors metal diode photomultiplier tubes (PMT) are used for all the surfaces in MEG, while in MEG II PMTs on inner face are replaced with silicon photomultiplier (SiPM). Fig. 3.33 is the design of the LXe detector and shows the definition of the six faces of inner, outer, upstream, downstream, top and bottom. The development view with the definition of the local coordinate system is described in Fig. 3.34. The inner face is on the $r = 67.85$ cm and depth of the active volume is 38.5 cm.
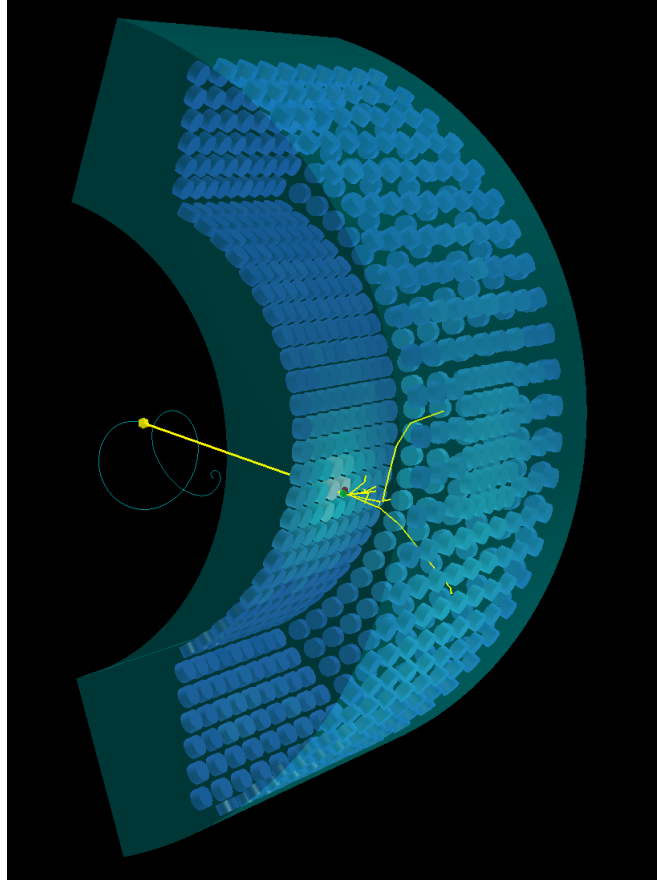
Figure 3.32: Overview of LXe detector. Configuration of photo sensors is one in MEG.

Since photons convert close to the inner face, photo sensors on it are basically illuminated by direct scintillation light. The position and time of the conversion point are reconstructed by distribution of illuminated photo sensors nearby the point, while total energy are reconstructed by summing up all the surrounding photo sensors.

Liquid Xenon

Using liquid as scintillator has an advantage to be uniform and free from radiation hardness, and to be purified whenever it need. We can keep its performance. The advantages of LXe scintillator are a lot more than that. Thanks to large atomic number of 54 and
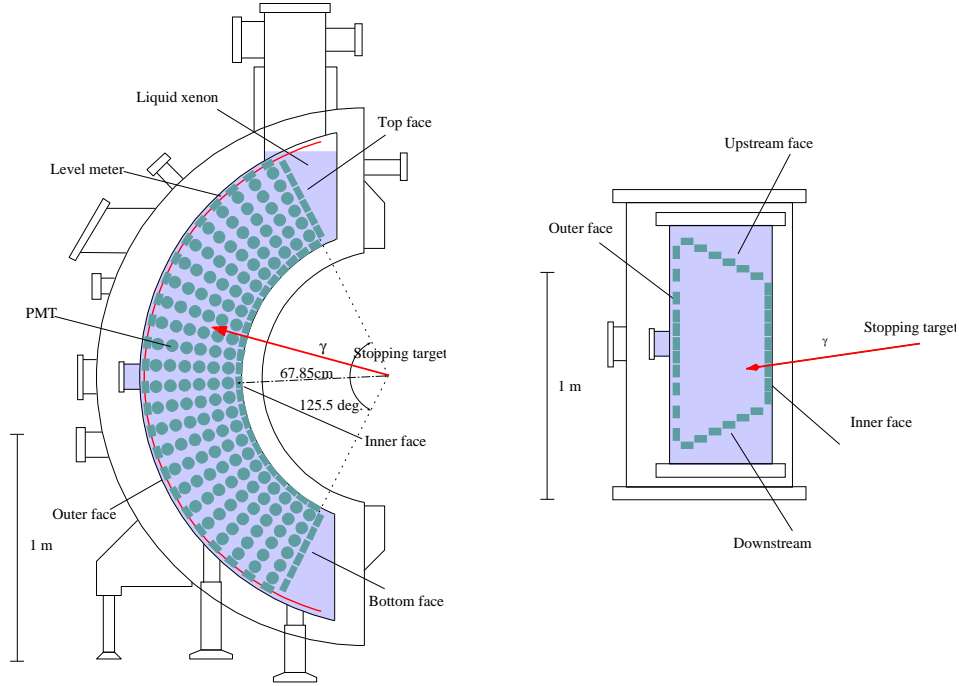
Figure 3.33: Schematic of LXe detector with MEG configuration of the photon sensor.

high density (2.978 g/cm^3 at 161.4 K), LXe performs large stopping power. Normally the photons convert within ~ 10 cm in the detector so we do not have to construct a huge detector. Its light yield of ~ 75 % of that of NaI is also great advantage, and its decay time is fast, 45 ns. Since scintillation light produced via a excited dimer (Xe_2^*) not via a excited xenon atom (Xe^*) itself in LXe, the yielded light is not absorbed by LXe in principle.

On the other hand, there are two disadvantages to adopt LXe. The first is the difficulty to keep it in liquid state. Fig. 3.35 shows the xenon phase diagram and indicates that keeping liquid state is allowed in a small temperature region around the atmospheric pressure. Therefore control of temperature to be around 165 K is essential. A cryogenic system composed of vacuum-tight vessels is already promised in the MEG experiment. For photon entering the LXe as much as possible, the entrance window is as thin as possible to stand ~ 3 atm and it is 0.075 X$_0$. A 200 W pulse-tube refrigerator developed for the LXe in MEG was used [25]. Basically the cryogenic system in MEG is taken over to MEG II. However due to increasing number of the cables from the detector for replacement with SiPMs to be described in next sub section in detail, another refrigerator is added.
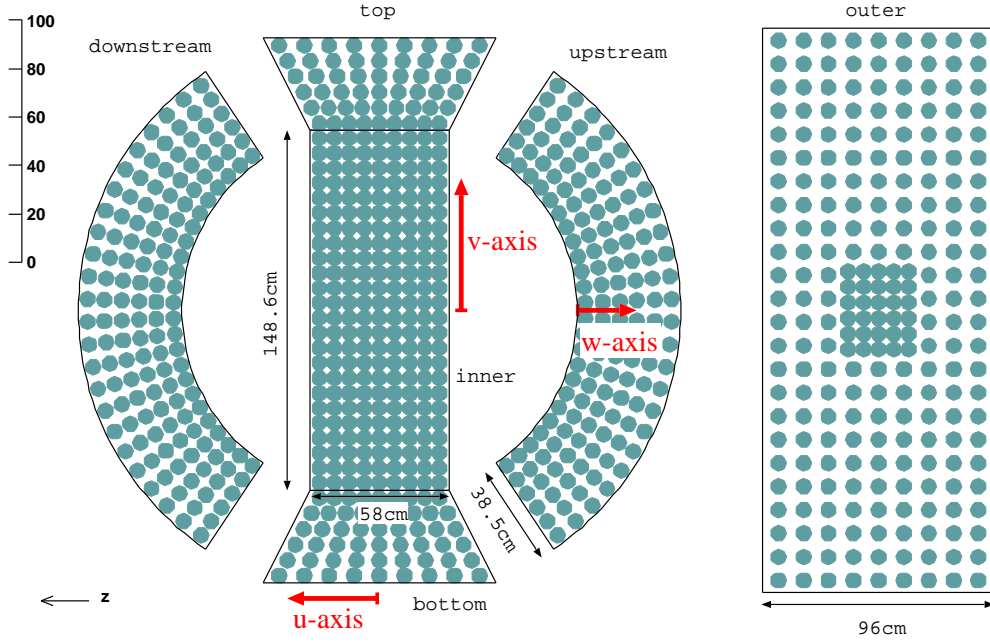
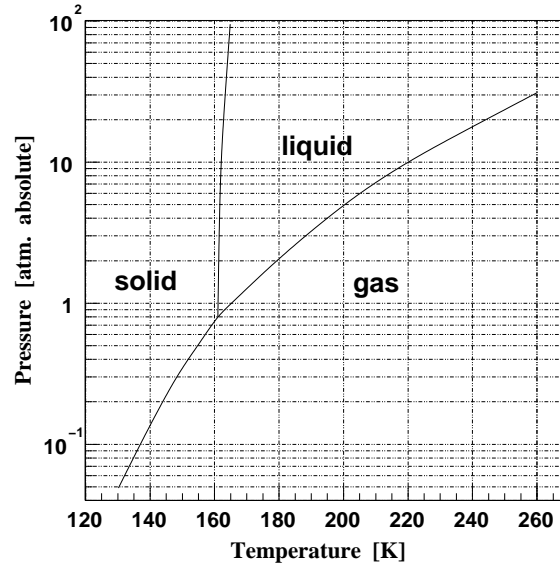Figure 3.34: Development view of LXe with local coordinate system.

Figure 3.35: Phase diagram of xenon.

LXe scintillation light of vacuum ultra-violet (VUV) is the second disadvantage to be overcome. The VUV light, which wavelength is short (10-200 nm), is namely absorbed by the oxygen and nitrogen in the atmospheric air. The wavelength of scintillation light from the excited xenon dinar is ∼175 nm, which is easily absorbed by contamination in LXe detector, mainly oxygen and water. Therefore purification system is required. In MEG purification system in liquid phase using molecular sieves and copper beads, and that in gas phase with metal-heated getter were prepared. These systems succeeded to

remove contaminations down to acceptable level of ppb order. They are re-used in MEG II. As LXe handling system, a storage system which enable purification and transfer to be effective and flexible was also developed in the MEG experiment and is re-used in MEG II.

Photo Sensors

The requirement for the photon sensors are (1) to be sensitive to VUV, and (2) less material to prevent photon from interacting a PMT on inner face, (3) to work proper in the low temperature. To satisfy them, new PMT (R9869) was developed by Hamamatsu photonics and MEG. The properties are summarized in Tab. 3.37 and the picture is shown in Fig. 3.3.2. They chose the quartz window which is transparent for VUV light, and Bialkali (K-Cs-Sb) for photo-cathode which is sensitive for VUV. Moreover to keep the performance against low temperature, the photo-cathode has aluminum strips which avoid the sheet resistance increasing. In MEG the 846-PMTs are installed on every LXe surrounding faces.

Figure 3.37: Properties of LXe PMT (R9869).

Figure 3.36: Picture of PMT (R9869) for LXe detector

Size	57 mm ϕ
Active are size	45 mm ϕ
PMT Length	32 mm
Photo-cathode material	K-Cs-Sb
Dynode type	Metal channel
Number of dynode	12
Typical HV	900 V
Typical gain	1×10^6
Typical quantum efficiency	15 %
Rise time	2 ns
Transit time	12.5 ns Typ.
TTS	0.75 ns Typ.

In the upgrade to MEG II, we replace all PMTs on the inner face to SiPMs. As shown in Fig. 3.34, because of round shape of PMTs there were large interval of 63 mm among PMTs on inner face while diameter of photo-cathode is 46 mm. This non-uniformity of the PMT coverage made event-by-event fluctuation of the efficiency of the scintillation light collection as shown in Fig. 3.38. In shallow events the efficiencies were quite difference between events where a photon interacts close to a certain PMT (event A in the figure), and does on a intermediate point among PMTs (event B). This non-uniform response deteriorated the energy and position resolutions of shallow events as described in Fig. 3.40 and as red markers in Fig. 3.39, even though off-line correction partially recovered the deterioration. Therefore in upgrade the SiPMs are employed to improve uniformity for detection of scintillation light and achieve higher granularity as shown in Fig. 3.41. Moreover SiPM is not sensitive magnetic field while gain of the PMT decreased with magnetic field as described in Fig. 3.42. Though magnetic field around LXe is reduced down to $\sim$50 Gauss, it deteriorated PMT performance. Less material property of SiPMs than that of PMT is also an advantage, which improves the detection efficiency of the photons 9 %.
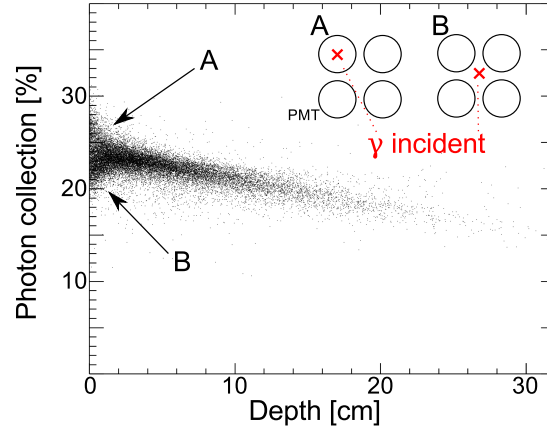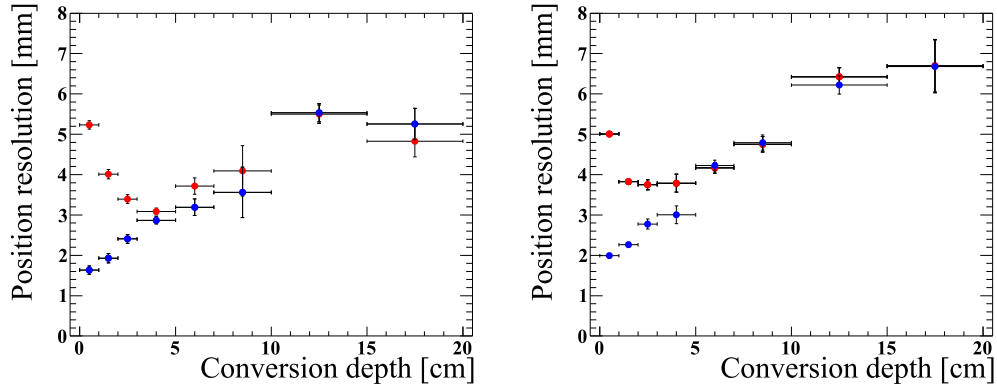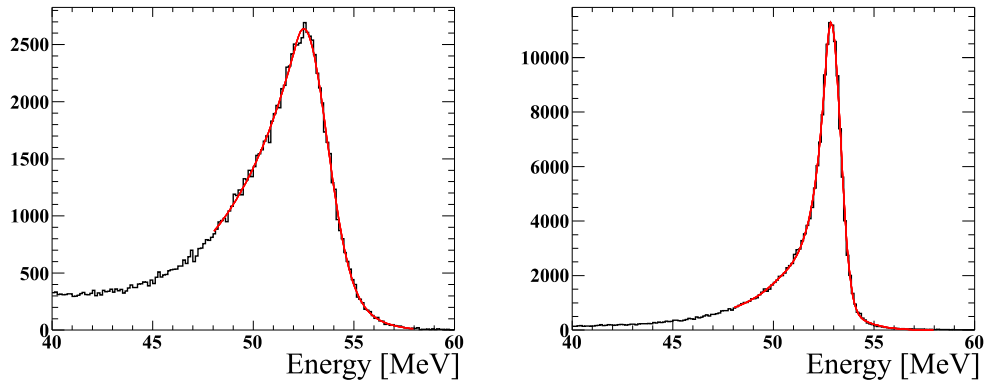
Figure 3.38: Efficiency of scintillation light collection.

Figure 3.39: Position resolution along v-axis (left) and u-axis (right) in MEG (red marker), and MEG II (blue marker).

Figure 3.40: Energy PDFs for signal gamma energy. The distribution of shallow ($w < 2$ cm) events (left) is larger than that of deep ($w \geq 2$ cm) events (right) in MEG.
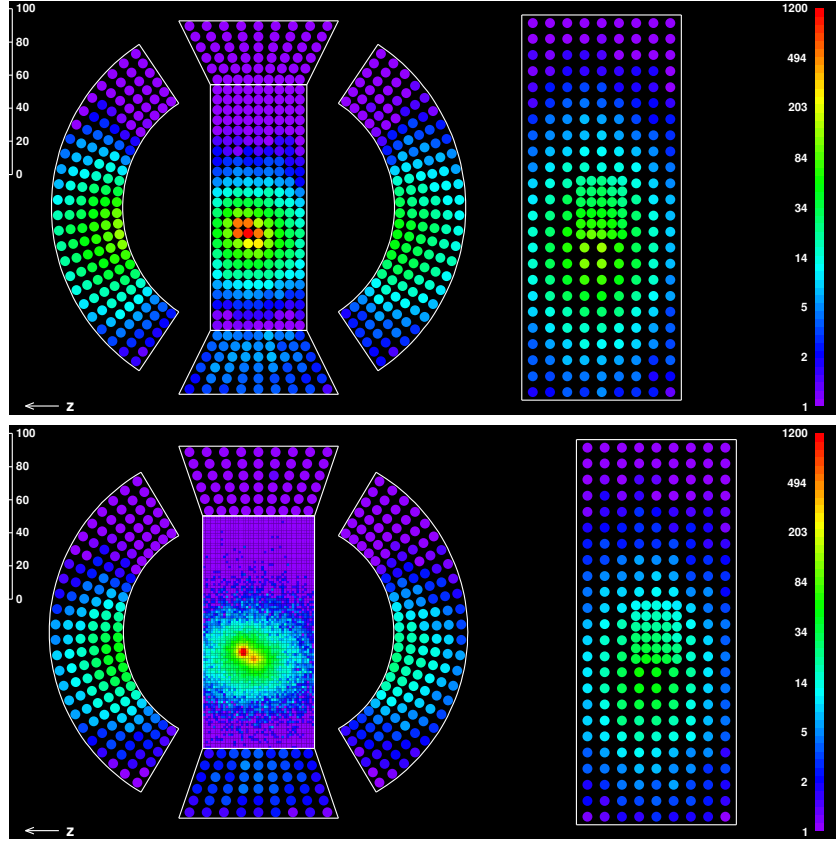
Figure 3.41: Example of an photon event with a pile up in MEG (top) and in MEG II (bottom) in MC. Because of higher granularity by SiPMs, the image of the photon becomes clear and the pile up is clearly separated from signal photon.

The development of the photo sensors is most challenging thing in the LXe detector upgrade, while the control system of LXe is already confirmed in the MEG experiment. What to be overcome are poor VUV sensitivity and small size of commercial SiPM. First, as discussed above, SiPMs should be sensitive to VUV light. We chose the p-silicon on n-substrate (p-on-n) type of SiPM which has higher performance for blue light region than n-on-p type. However the materials in front of sensitive area of the SiPM is not optimized to the VUV and loose photon detection efficiency (PDE). By optimizing a protection layer and anti-reflection coating layer which decreased the PDE, we achieve the PDE higher than 15 % from measurement with photons from α source. The performance which is similar with MEG PMT ($\sim$16 % quantum efficiency), is enough to upgrade LXe detector because the 50 % larger sensor coverage of SiPM increases the total statistics.

Second problem is small size of SiPM. Largest size of commercial one is 6×6 mm^2, but limited number of the readout channels does not allow such a small SiPM to cover whole inner face. However a larger SiPM is faced with such problems as higher dark current rate, larger non-uniform gain, and larger sensor capacitance which causes longer tail and larger noise. To solve these problems, a 12×12 mm^2 SiPM composed of four 6×6 mm^2 SiPMs is developed as shown in Fig. 3.43

The other properties of new SiPMs for LXe have been studied to make sure keeping their performance in high rate and low temperature environment.
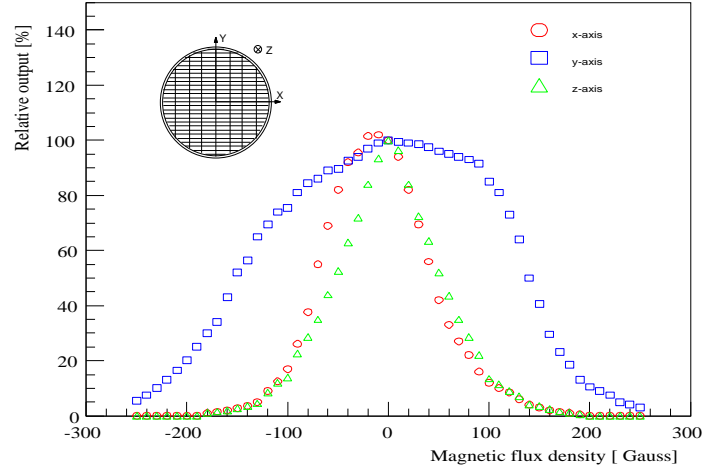
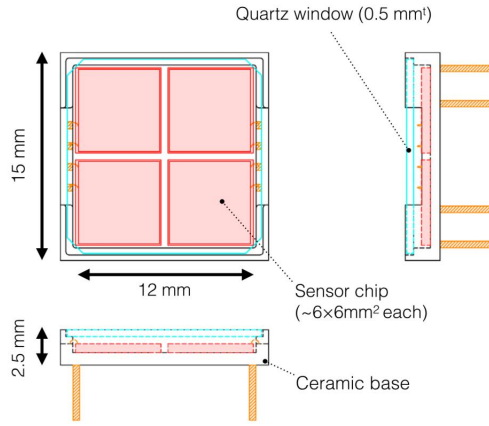Figure 3.42: PMTs gain dependence on magnetic flux density.

Figure 3.43: Drawing of SiPM for LXe.

Status

The construction and installation of the LXe detector is completed in 2017. Though the number of the read out channels is limited due to the delay of the mass production of the electronics, the pilot run is successfully performed at the MEG II beam line.

3.3.3 Radiative Decay Counter

The radiative decay counter (RDC) is newly installed in the MEG II detector to reduce the photon background. As described in Sec. 3.1.2 the dominant background is the accidental coincidence between a positron from Michel decay, and a photon from AIF and RMD. The expected ratio of the photon background is shown in Fig. 3.44. Due to the reduction of the DCH material in MEG II, the photon originated from AIF is expected to be reduced in the simulation study. Therefore RMD should be the dominant source of the photon background. When the photon from RMD has a high energy of more than 48 MeV, which becomes the background, a low momentum positron of 1-5 MeV is also emitted. RDC detects this low momentum positrons. According to simulation study, the sensitivity of

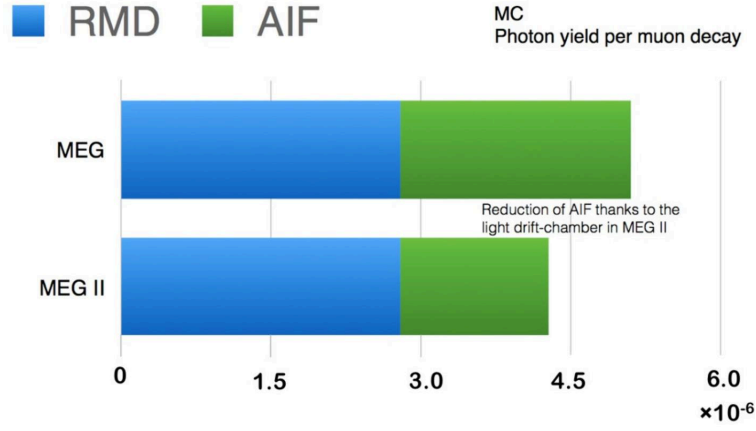the MEG II experiment will be improved by 15 % by RDC.

Figure 3.44: Fraction of photon background source.

Design

The schematic of RDC is shown in Fig. 3.45. RDC is placed downstream on the beam axis because in the COBRA magnetic field the bending radii of the low momentum positrons are smaller than 6 cm. By taking the coincidence with the LXe detector, we can identify the background photon as shown in Fig. 3.46. Moreover to distinguish the RMD positrons from the Michel positrons, which does not emit any photon, the energy is also measured by RDC. The energy distribution of RMD positron and Michel positron at RDC is shown in Fig. 3.47. The Michel positrons tend to have higher energies than the RMD positrons.
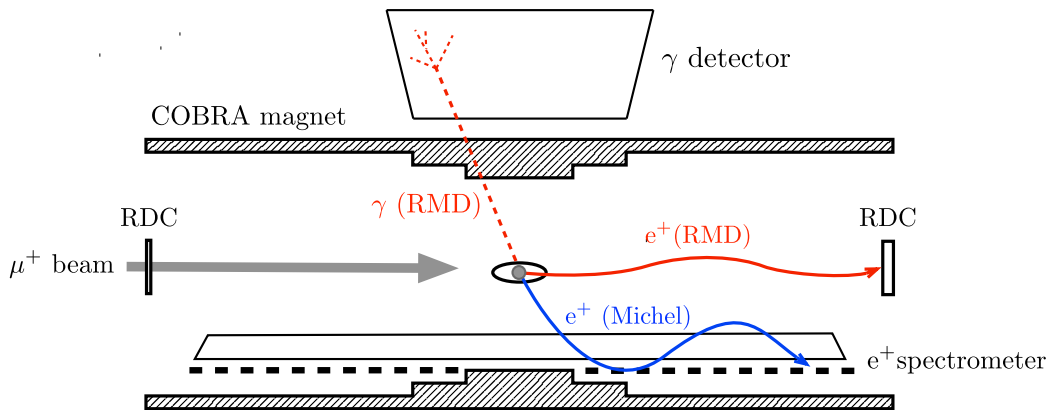
Figure 3.45: Conceptual drawing of RDC.
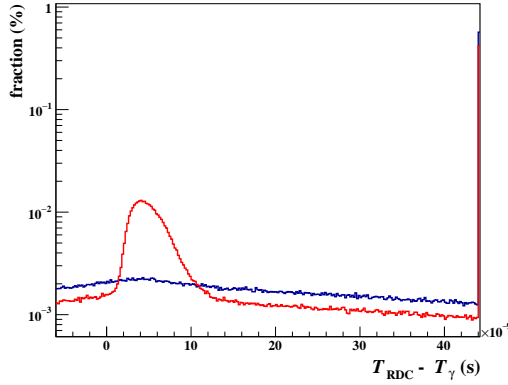
Figure 3.46: Distribution of relative time between the RDC and the LXe detectors in MC. Time resolution of 100 ps is assumed.
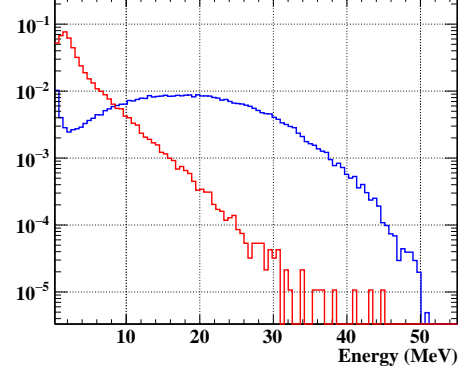
Figure 3.47: Expected energy distribution in RDC from RMD positrons which photon energy is more than 46 MeV (red) and Michel positron (blue).

Fig. 3.48 shows the design of RDC. The RDC detector composed of two parts, 12 plastic scintillator bars for the timing measurement in front and 76 LYSO (Cerium-doped Lutetium Yttrium Oxyorthosilicate) crystals for the energy measurement behind.

The detailed schematic view of the scintillator bars is shown in Fig. 3.49. SiPMs (S13360-3050PE Hamamatsu Photonics) readout the scintillation light from the several size (7-19 cm length, 1 or 2 cm width, 5 mm thickness) of the plastic scintillator bars wrapped a 65 μm thick reflective sheet (ESR from 3M). Using the *beta*-ray from ^{90}Sr source, the time resolution of $\sim$90 ps is obtained in each bar.

Because of the high light yield, LYSO crystal is suitable for the energy measurement. Tab. 3.4 shows the properties of the LYSO crystal. Fig. 3.50 shows the picture of LYSO crystal wrapped with ESR film. Each LYSO crystal is a 2 cm cube and attached one SiPM (S12572-025 from Hamamatsu Photonics) on the downstream side of the crystal by a spring. This calorimeter part of RDC is also measured with ^{60}Co source and the energy resolution is $\sim$6 % for the 1 MeV photon for all the crystals.

Table 3.4: Properties of LYSO crystal [26]

Density	7.4 g/cm^3
Radiation length	1.14 cm
Decay constant	42 ns
Emission peak	420 nm
Light yield	3×10^4 photons/MeV

Performance

The construction of the full RDC detector was completed. It was installed and tested at the πE5 beam line. By using 16 BGO crystals attached PMT as the substitute of the LXe detector, we obtained the RMD peak in the relative time distribution between the photons and the positrons as shown in Fig. 3.51. Moreover the energy is also successfully measured
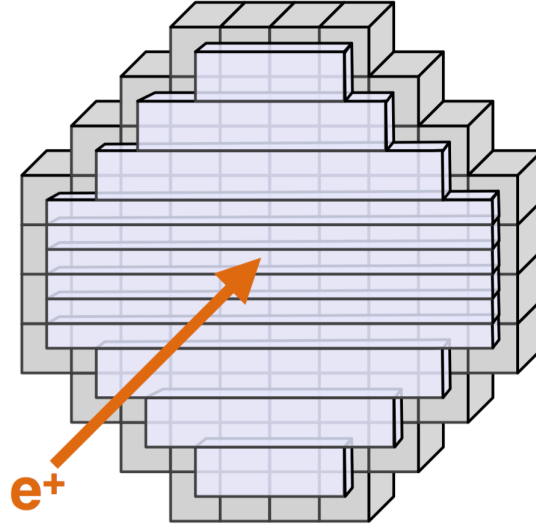
Figure 3.48: Overview of RDC design. Height and width are ∼22 cm.

by the LYSO part as shown in Fig. 3.52. The red colored histogram in Fig. 3.51 shows the time distribution after rejecting the event in which the energy measured by LYSO is more than 4 MeV. By this cut the background is reduced to ∼1/10 while the RMD event is to ∼1/3. The optimization of the trigger threshold and more sophisticated analysis such as likelihood analysis will develop the identification of RMD.

Status

As described above, RDC is ready for the physics run and the ability of the RMD tagging is demonstrated. Furthermore, upstream RDC is under consideration. It is more challenging because RDC in upstream is exposed to the high intensity muon beam. One of the candidates is a synthetic diamond detector. It has fast signal, and high radiation resistance. Assuming the 100 % detection efficiency of the upstream RDC, the enhancement of the sensitivity is expected to be 10 %.

3.4   Trigger and Data Acquisition

In the MEG experiment the raw waveforms from the detectors are obtained for efficient off-line analysis. The digitizer was developed in PSI, which is Domino Ring Sampler (DRS) [27]. While the performance of the electronics should be kept in MEG II, the total channels increase with the usage of SiPMs and the finer cells of the DCH. Moreover the signal of the SiPMs is smaller than that of PMTs which were mainly used in the MEG experiment. Therefore the amplifiers are also required in the new electronics with flexible amplification to satisfy the necessity of the several detectors.

To deal with increase of the channels and SiPMs, the electronics is redesigned. Fig. 3.53 shows the comparison of the design of the electronics in MEG and MEG II. The trigger and DAQ system becomes compact in MEG II by rejecting the active splitter between the
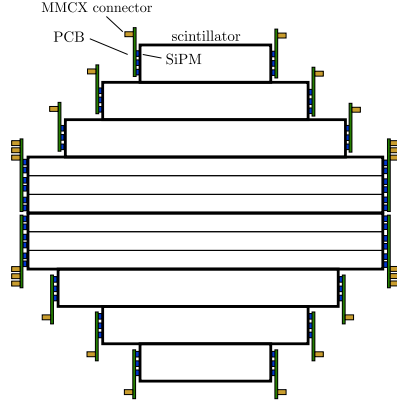
Figure 3.49: Schematic view of scintillator bar attached SiPMs for time measurement.
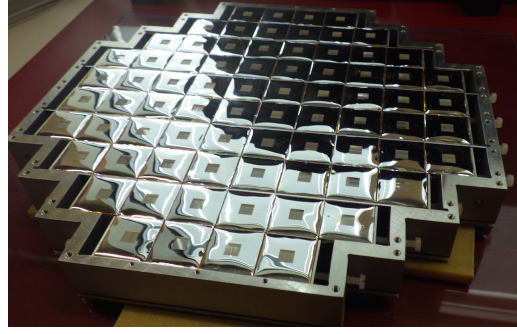

Figure 3.50: Picture of LYSO crystal wrapped by reflector.
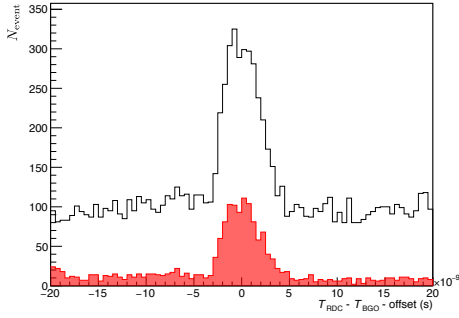

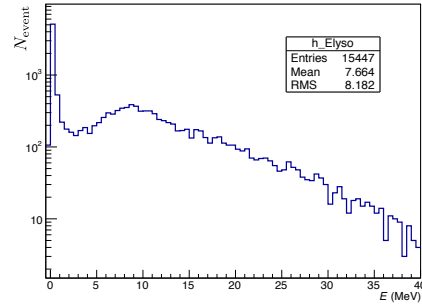Figure 3.51: Distribution of relative time between the RDC and the BGO detectors.

Figure 3.52: Energy distribution measured by LYSO crystal

trigger line and DAQ line in MEG and by integrating the basic trigger, DAQ functionalities, high voltage chip, and amplification onto the same board called WaveDREAM board (WDB) developed in PSI.

In MEG II the WaveDAQ crate is also developed. It is a 3 HE 19" crate with 18 slots to satisfy the requirement of Gbit links, common high voltage source, and the concentrators for the trigger, the clock to correct the jitter, and the data. The Crate Management Board (CMB) is placed in each crate, and generates the crate power of 24 V with 359 W and stand-by power for a shelf manager. Furthermore CMB controls and monitors the slow control in MEG II based on MIDAS (Maximum Integration Data Acquisition System) [28] which was used in MEG successfully.

Each crate also has 16 slots for WDBs each of which has 16 channels, and two of so-called concentrator boards of the Trigger Concentrator Board (TCB) and the Data Concentrator Board (DCB) to operate the trigger and DAQ at the same time. TCB is also used the higher hierarchy of the trigger as a Master board (see Fig. 3.53 again). The MEG II experiment use the 39 crates in total including the global trigger boards.

The MIDAS controls the whole of the system. The raw data from the detectors are stored in the MIDAS file.
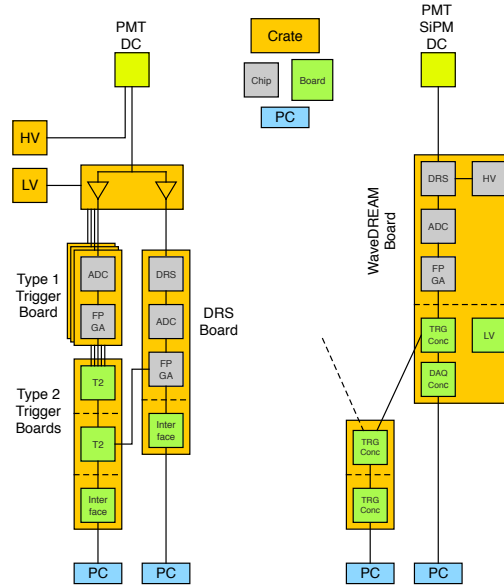

Figure 3.53: Schematic view of TDAQ electronics overview.

3.4.1 WaveDREAM

Fig 3.54 shows the schematic view of the WaveDREAM. It contains an amplifier and a waveform shaper. We can select the flexible gain from 0.5 to 100, and shape the waveform through a programmable pole-zero cancellation. One WaveDREAM has two DRS4 chips connected to two 8 channel ADCs. They digitize the waveform with the maximum sampling speed of 5 GSPS with 1024 cells. The out put of the ADCs are transmitted to Field-Programmable Gate Array (FPGA), which treats trigger algorithms.
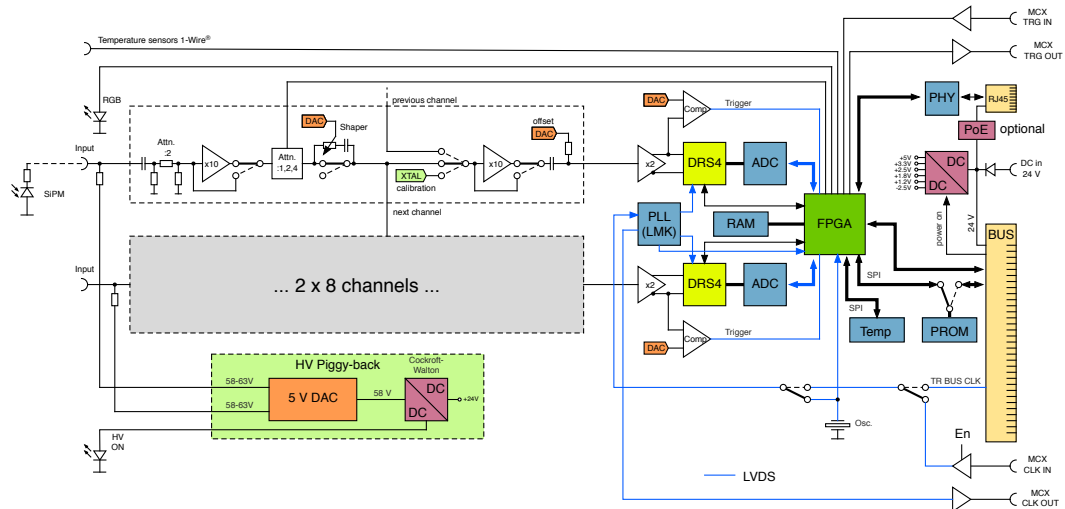

Figure 3.54: Schematic view of WaveDREAM board.

The bias voltages for SiPMs are also generated in the WaveDREAM board by a Cockcroft-Walton (CW) voltage multiplier. Moreover a simple 5 V DAC is mounted after the CW to allow the channel-by-channel biases from +0 V to +5 V. The accuracy of the high voltages is below 1 mV. The currents are measured with a resolution of 1 nA.

3.4.2 Synchronization

The synchronization system with ultra-low jitter has been developed for MEG II. The time reference clock is generated by an ancillary board which provides the DCB in WaveDAQ crate. In the WaveDAQ crate the DCB distributes the master clock to the WDBs via the dedicated clock signal distributer having a jitter cleaner (LMK03000 from Texas Instruments). We performed the jitter less than 10 ps at the input of WDB. Moreover for off-line synchronization the clock pulse itself is readout in WaveDREAM.

3.4.3 Trigger

With increase of the beam intensity, the trigger in MEG II is required suppressing backgrounds to make the trigger rate of 10 Hz or less for the effective DAQ and the reduction of the overall data size. Since DCH signal is too slow to be used for the trigger, the LXe detector and TC are used. The observables reconstructed on-line are the photon energy, the relative time of the photon and the positron, and the opening angle. These algorithms are implemented in FPGA.

In the LXe detector, the summing waveform over 4×4 SiPM patch is transmitted to the trigger system as a single detector. The photon energy is obtained by summing up the signal amplitude taking into account each photo-sensor gain.

The relative time is reconstructed from the on-line time of TC and LXe. The photon time is reconstructed from the patch of SiPMs with the correction of time walk. In MC study, the on-line photon time resolution is expected to be 284 ps with requirement of more than 45 MeV for the photon energy. On the other hand, the positron time is extracted from the single counter of TC which is placed at most inner z in all the hit counters. The time is obtained by averaging the raising times of two channels in the single counter with the correction of the track length from the target to the counter. Since we do not use the DCH information for the trigger, the online time resolution includes the difference of the track length for each positron turn, which is 2-3 ns for each.

Thanks to the pixelated design of TC and higher granularity of LXe in MEG II, we can select the events more tightly from the opening angle view point by preparing the look-up table for the correlation of the position distribution between TC and LXe.

3.5 Current Status of MEG II

We completed the construction and installation of almost all the detectors in the MEG II experiment except for DCH. In summer 2018 DCH will be installed and full engineering run will be started in 2019 toward the physics run.

3.6 Timing Measurement

The theme of this thesis is the timing measurement. The distribution of the relative time between the photon and the positron measured in MEG is shown in Fig. 3.55 [1]. The time of the accidental background distributes uniformly in the time window, while

that of the signal makes a peak. Therefore, as written in Eq. 3.7, the resolution of the relative time between the photon and the positron reduces background lineally. The timing
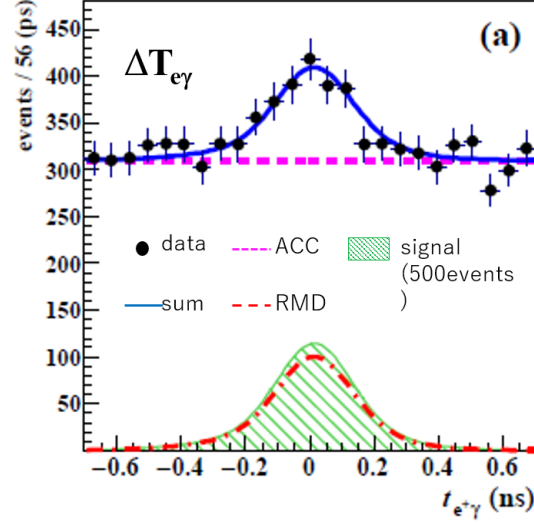

Figure 3.55: PDFs of the relative time between positrons and photons with the data spectra for the full dataset in MEG [1]

measurement in MEG was limited by the positron spectrometer. LXe photon detector had the time resolution of 67 ps, while the time resolution of the positron spectrometer was 107 ps. As described above, in the MEG II experiment, the measurement of the flight time between TC and the vertex will improve to 15 ps by reducing the material between DCH and TC. Therefore, the time resolution of the timing counter will be dominant contribution to the timing measurement of the positron. Its development is essential.

Chapter 4

Timing Counter

The time of the positron is measured by the timing counter (TC) as described in Chap. 3. The positron time on the vertex is reconstructed by subtracting the path length reconstructed by the drift chamber (DCH), which is placed in front of the TC, from the time on the TC. Since the DCH signal is too slow to be used as a trigger, the TC signal also takes a role as the trigger signal of the positron side. The TC is pixelated by scintillator counters readout by SiPMs. This fine segment design improves for the timing measurement significantly. This chapter will explain the concept and design of the timing counter for the MEG II experiment in detail. Furthermore the detailed quality of the counters and the operation system including the calibration system, and the slow control system will be described.

4.1   Requirement

In MEG II the time resolution of the positron side should be improved to be comparable or better than that of the photon side. In MEG II the time resolution of the photon side is expected to be 50–70 ps. Therefore the time resolution of ∼40 ps is required for the timing counter.

In the MEG experiment a timing counter was composed of 30 scintillator bars ($80 \times 4 \times 4 \, \mathrm{cm}^3$) with PMT readout. It achieved ∼70 ps time resolution and led the MEG experiment to success. However, the resolution was worse than the expectation (40 ps) obtained from results in beam tests due to a large variation of the reconstructed hit positions on the bars, a degradation of the PMT gain in magnetic field, poor time calibration among the bars, the electronics jitter, and the effect of pile up hits.

Furthermore, the hit rate on the timing counter is increased with planned increasing of the beam intensity in MEG II. In MEG a PMT had signal event at 1 MHz. In the MEG II environment it will be 2 MHz, which corresponds to one pile up in every event in the DAQ time window. A new positron timing counter should operate at this hit rate.

4.2   Concept

The concept of a new timing counter in the MEG II experiment is a finer segmented counter to overcome these issues. We realize the timing counter by using a new photon sensor, silicon-photomultiplier (SiPM), which is a compact (1–6 mm square) and high gain (10^5–10^6) photon sensor. Furthermore, SiPM is not affected by magnetic fields. By employing the SiPMs, the timing counter can be pixelated with smaller plastic scintillator.

Thus, a signal positron is measured by several counters, which results in better resolutions than that in MEG.
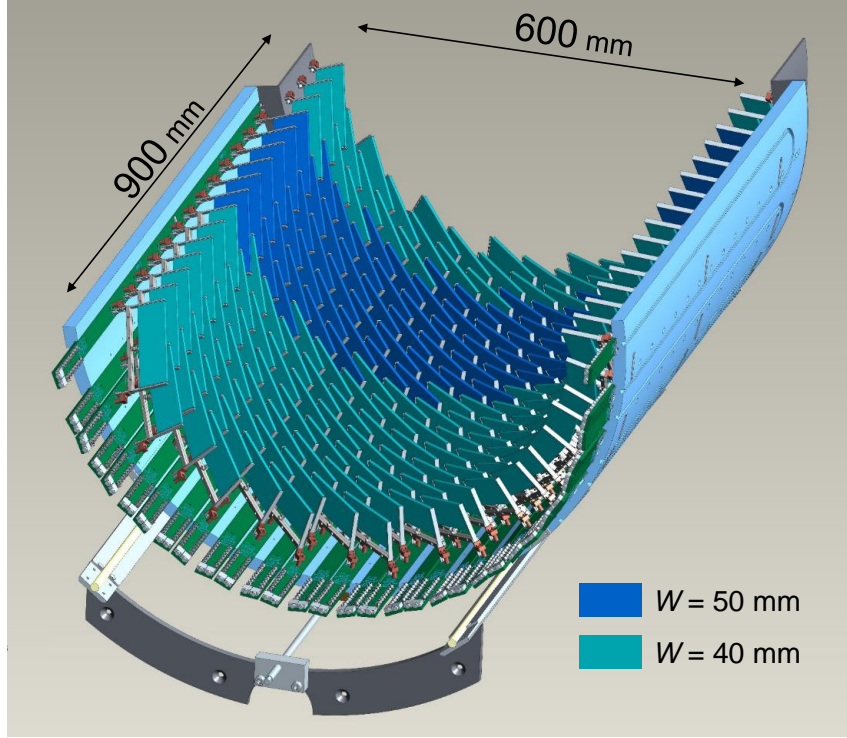
4.3   Design

Figure 4.1: Timing Counter Overview

The positron timing counter consists of two sectors: one on the downstream (DS) and the other on the upstream (US) of the target, which are mirrored each other. They are mounted between the drift chamber and COBRA magnet , and in $23.0 < |z| < 116.7$. Its coverage along ϕ direction is $-165.8° < \phi < 5.2°$ to match the photon acceptance of the Xe detector, . One sector of positron timing counter consists of 256 counters, each of which is composed of a fast plastic scintillator plate ($120 \times 40/50 \times 5$ mm^3) and 6 silicon-photomultipliers (SiPMs) at each end. The six SiPMs at each end are connected in series to obtain sharper signal. Signals from the counters pass through long PCB ($\sim$80 cm) called back plane on which counters directly connected. At the end of the PCB the signals are transmitted by non-magnetic coaxial-cable (RG178) to WaveDREAM, in which the signals are amplified and shaped by pole zero cancellation.

The overall counters configuration and size are optimized for better experimental sensitivity in MC. Fig. 4.2 shows the counter configuration in which the 16-counters are placed with the interval of 5.5 cm along z in each 16 ϕ line at 10.3° interval. Each two ϕ line is staggered to maximize positron detection efficiency. All counters are tilted at 45° so that positrons from the target penetrate the counters perpendicularly. Fig. 4.3 shows a typical signal positron event. The distribution of the incident angles of the signal positrons to the counters is shown in Fig. 4.4.
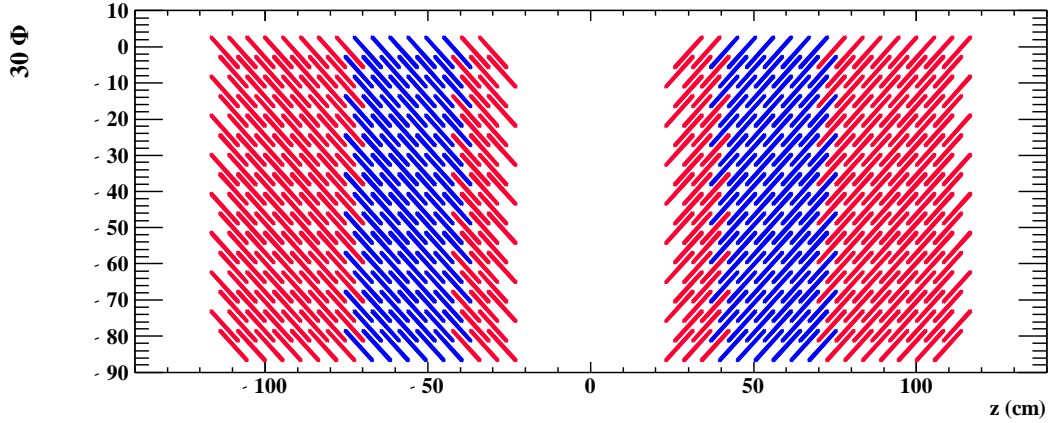
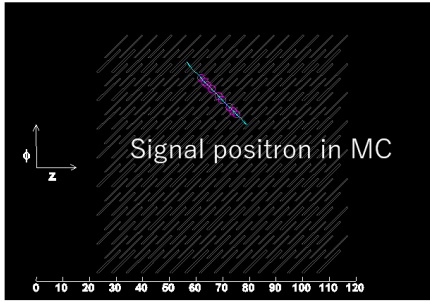Figure 4.2: Counter configuration. Two counters with 40 mm (red) and 50 mm (blue) height are used.

Figure 4.3: An example of typical signal positron event in MC. Signal positrons enter counters perpendicular.
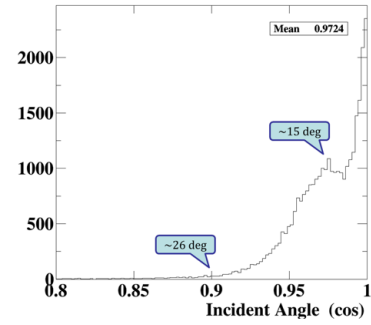

Figure 4.4: Districation of incident angles to counters

4.3.1 Multiple Hit Principle

Thanks to the pixelated design, a signal positron hits several counters as shown in fig. 4.5, which is a typical signal event. Fig. 4.6 shows the number of TC hits from a signal positron in MC simulation, and the average is 8.8 hits.

The overall time resolution is described as a function of the number of hits (N_{hit}),

$$\sigma^2_{\text{total}}(N_{\text{hit}}) = \frac{\sigma^2_{\text{single}} + \sigma^2_{\text{inter-counter}} + \sigma^2_{\text{elec}}}{N_{\text{hit}}} + \sigma^2_{\text{MS}}(N_{\text{hit}}), \tag{4.1}$$

where σ_{single} is a single counter resolution; $\sigma_{\text{inter-counter}}$ is miss time alignment among the counters; σ_{elec} is electronics jitter; σ_{MS} is the effect of multiple scattering,

$$\sigma^2_{\text{MS}}(N_{\text{hit}}) \sim \frac{\sum_{n=1}^{N_{\text{hit}}} (n-1)\sigma^2_{\text{MSsingle}}}{N_{\text{hit}}}, \tag{4.2}$$

where σ_{MSsingle} is time spread after a positron passes through one counter, and is several pico seconds with a 5 mm thickness counter. The effect of jitter and miss time alignment become small by measurement with several counters, thus the overall time resolution is
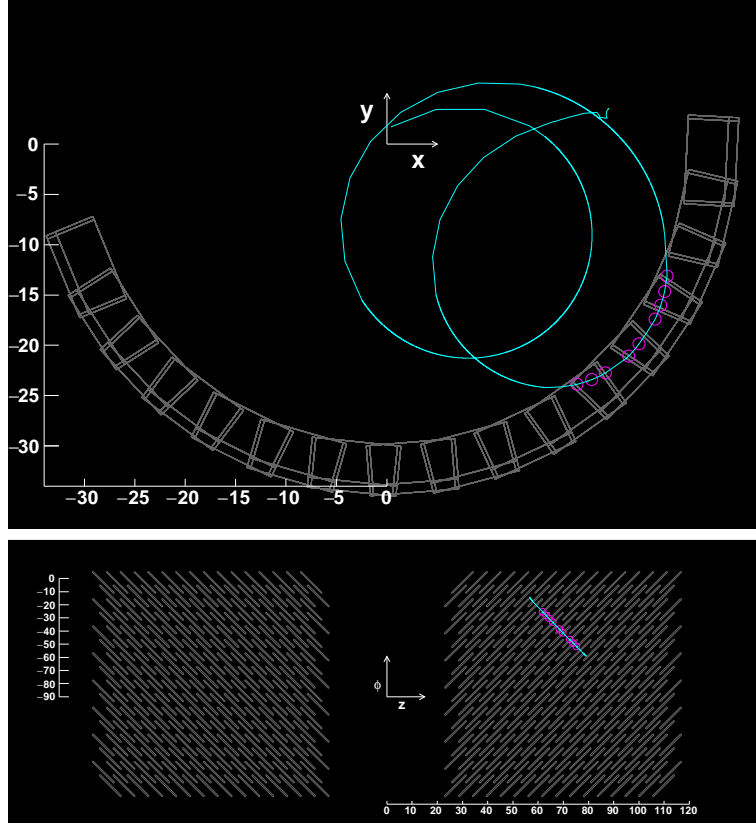
Figure 4.5: A typical signal event in MC. The magenta circles show hits on counters and the cyan line is a trajectory of a signal positron. The top figure is x-y view, and the bottom is z-ϕ view. The trajectory in $28 \leq$ r ≤ 38 cm is described in z-ϕ view.

improved. The estimation of the overall resolution from these formula is showed in fig.4.7. It indicates resolution improvement with a large number of hits.

4.4 Single Counter Design

Concept of single counter design is explained in this sub section. The picture of the single counter with definition of counter local coordinate is shown in Fig. 4.8. We defined the coordinate along length, width, and thickness as (v, u, w), and on both ends along length 6-SiPM-arrays are attached.

The optimized components for single counter are summarized in Tab. 4.1. The resolution depends on photon statistics. Fig. 4.9 shows energy deposit dependence of the resolution. A fast rise time is also required to obtain the ultimate timing resolution below hundred pico-second because scintillator rise time is typically several hundred pico-seconds.

4.4.1 Scintillator

Ultra-fast plastic scintillator is used. The time resolution is affected by photon statistics and rise time, which require large light yield, long attenuation length and fast rise time to scintillator. Since there is trade-off between these properties as summarized in Tab. 4.2,
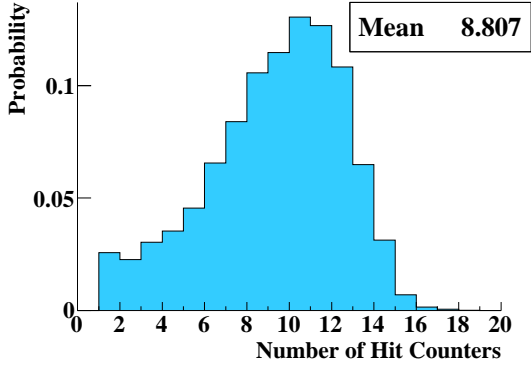
Figure 4.6: Number of hits from signal positron in the same turn.
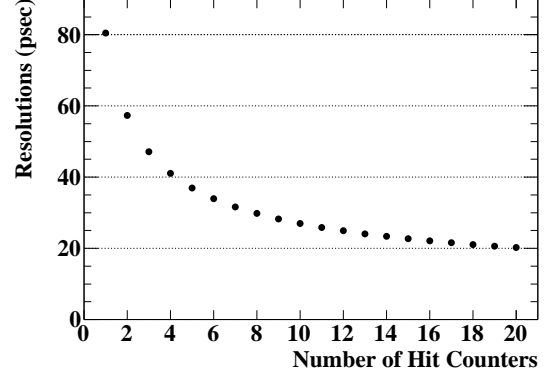

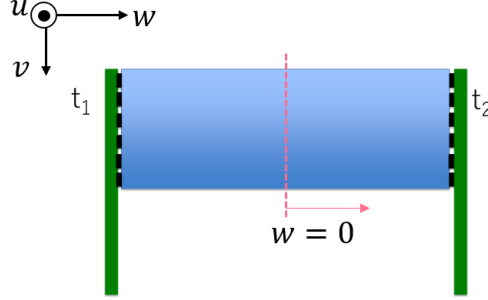Figure 4.7: Overall resolution as a function of number of hit counters

Figure 4.8: Conceptual drawing of single counter

we tested several types of scintillators. The results are also written in Tab. 4.2 and counter made from BC-422 performed best with respect to time resolution. Compared with MEG the size of single detector is small, and that allows for faster rise time scintillator to have good performance against its short attenuation length.

4.4.2 Size

The size is optimized to acquire the best time resolution concerning trade-off between single counter resolution and the number of hits of a positron with the limited number of readout channels. With regard to single counter, a smaller counter has better resolution. Along length, a longer counter has a worse resolution because of attenuation of scintillation light. Along height, a shorter counter increases SiPMs coverage to scintillator surface, which results in better resolution than a taller counter. Several size of counters were tested and the result is shown in Fig. 4.10 [32].

However the overall TC resolution also depends on the number of hits from a signal positron, not only single counter resolution (to be explained in detail in next subsection). A larger counter can cover the TC acceptance region with smaller space among counters and increase the number of hits, and, furthermore, efficiency. These effects are studied by simulation. In particular, height of the counter is well-optimized. Though signal positrons are concentrated around $r \sim 30$ by COBRA magnet, spread of the distribution depends

Components	Optimal	Manufacture
Plastic Scintillator	BC-422	Saint-Gobain
Size of Scintillator	$120{\times}40/50{\times}5$ mm^3	–
Reflector	enhanced specular reflector (ESR)	3M
SiPM	ASD-NUV3S-P-High-Gain	AdvanSiD
Number of SiPMs	12 (6 on each end)	–
Connection of SiPMs	series	–

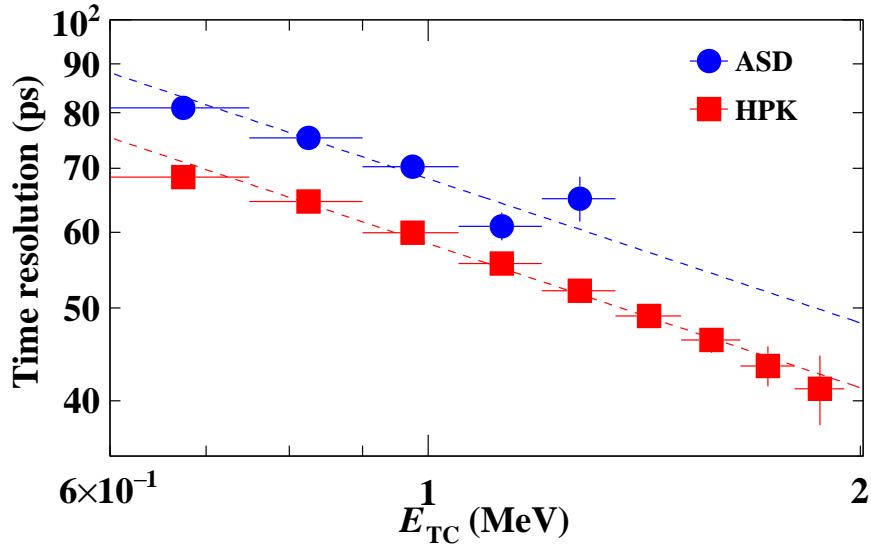Table 4.1: Summary of single counter components optimized by comparison test.

Figure 4.9: Resolution dependence on the energy deposit. Scintillator is BC418 (Saint-Gobain) with $90{\times}40{\times}5$ mm^3. Two type of SiPMs, S10943-2547(X) from HAMAMATSU (Red), and NUV Type from AdvanSiD (Blue), are used. [29]

Table 4.2: Properties of ultra-fast plastic scintillators from Saint-Gobain. The properties of BC-404, which was used in the previous timing counter bar, is also shown for comparison.

Properties	BC-418	BC-420	BC-422	BC-422Q	BC-404
Light Output[a] (% Anthracene)	67	64	55	19	68
Rise Time[a] [b] (ns)	0.5	0.5	0.35	0.11	0.7
Decay Time[a] (ns)	1.4	1.5	1.6	0.7	1.8
Peak Wavelength[a] (nm)	391	391	370	370	408
Attenuation Length[a] (cm)	100	110	8	8	140
Time Resolution[c] (ps)	48 ± 2	51 ± 2	43 ± 2	66 ± 3	–

[a] From Saint-Gobain catalogue [30].

[b] Those values are dominated by the measurement setup. The intrinsic values are much faster. For example, a BC-422 rise time of <20 ps was reported in [31].

[c] Measured value in [32] with $60{\times}30{\times}5$ mm^3 sized counter read-out with 3 HPK SiPMs (S10362-33-050C) at each end.

on z as shown in Fig. 4.11. Hence we found that optimal height is 50 mm for $|z| <\sim 70$ cm
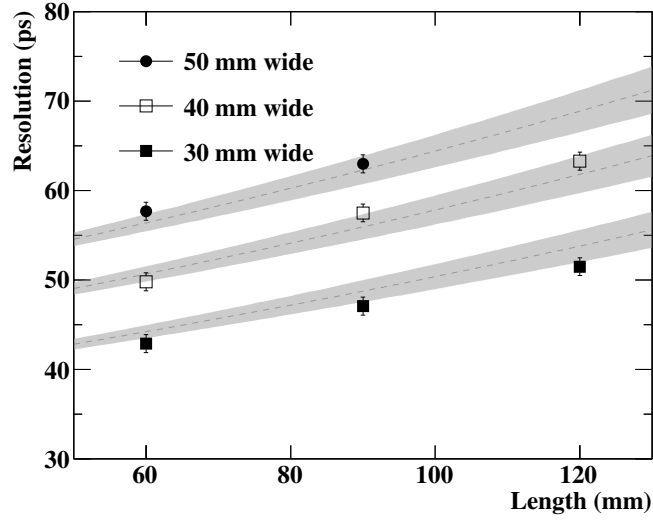
Figure 4.10: Resolution dependence on scintillation size

and 40 mm for $|z| > \sim 70$ cm. In spite of the optimized value, we chose 40 mm-height-counters for $|z| < \sim 40$ cm because of the space limitation from the COBRA magnet. Counter configuration is shown in Fig 4.2.

4.4.3 SiPM

Silicon photomultipliers (SiPMs) are photon-sensors for reading out scintillation light. In principle a counter with more SiPM readouts has larger coverage bringing better time resolution because of increase of photon statistics. However because of a constraint of the number of readout channels ($\sim$1000), all SiPMs on each side of the counter has to be combined to one channel. Both connection schemes of parallel and series are tested and the resolutions are shown in the right figure in Fig. 4.12. As shown in the left figure in Fig. 4.12, waveform from SiPMs connected in series becomes sharper than the others, because total capacitance with series connection becomes smaller than that of individual SiPM while that with parallel becomes larger. The waveform analysis is optimized at each point. (AppendixB)

The scintillation light is in the near-ultraviolet (NUV) range. Therefore the SiPMs for TC should be sensitive to NUV light. The SiPMs based on p-on-n diode are sensitive to the NUV light. We tested the p-on-n SiPMs developed by several manufactures. Fig. 4.13 shows the results. The SiPMs of HAMAMATSU Photonics have the best performance for the time resolution because their photo detection efficiencies are highest in the tested SiPMs. It also indicates that the time resolution depends on photon statistics.

On the other hand, we also confirmed that increasing the number of SiPMs improves timing resolution as shown in Fig. 4.14. The number of SiPMs per counter is limited by cost. Therefore the final design of the single counter is decided on the basis of the balance between cost and quality of the SiPMs. Finally we adopted the 6-series AdvanSiD SiPMs per one side of the counters.
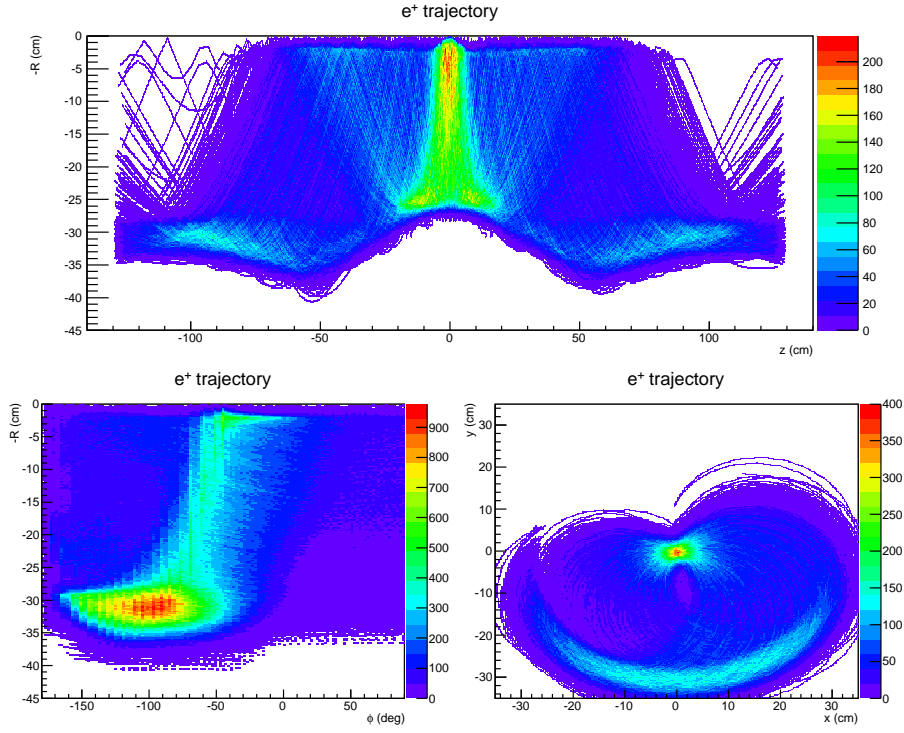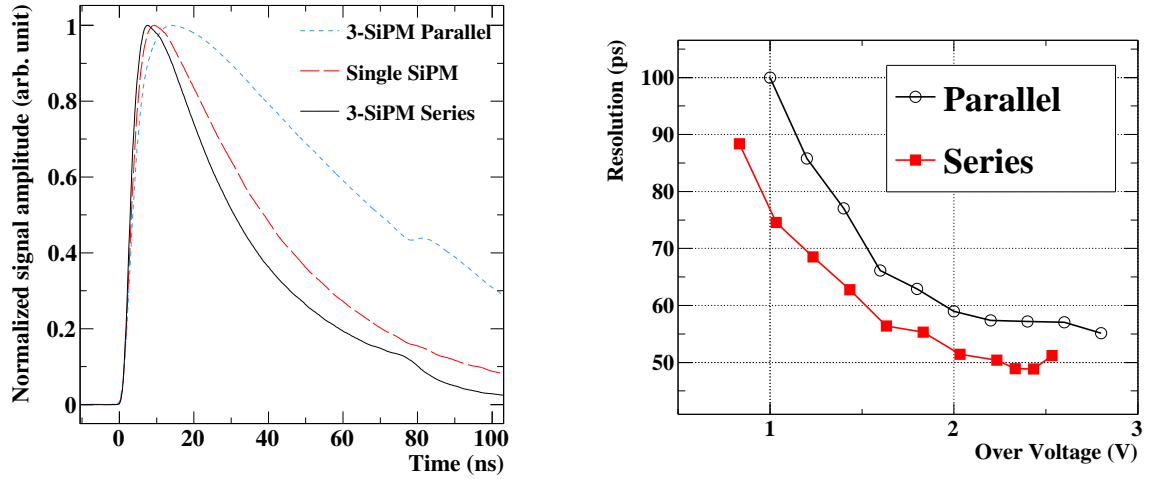
Figure 4.11: Accumulated positron trajectory.

Figure 4.12: Connection comparison with test counter made from $60\times30\times5$ mm^3 BC422 scintillator attached 3 Hamamatsu Photonics SiPMs (S10362-33-050C). Averaging waveforms with several thousand events are shown in left figure [32]. They are normalized by their amplitudes. The resolution comparison between parallel and series connections is in right figure in which over voltage is written as that for one SiPM.
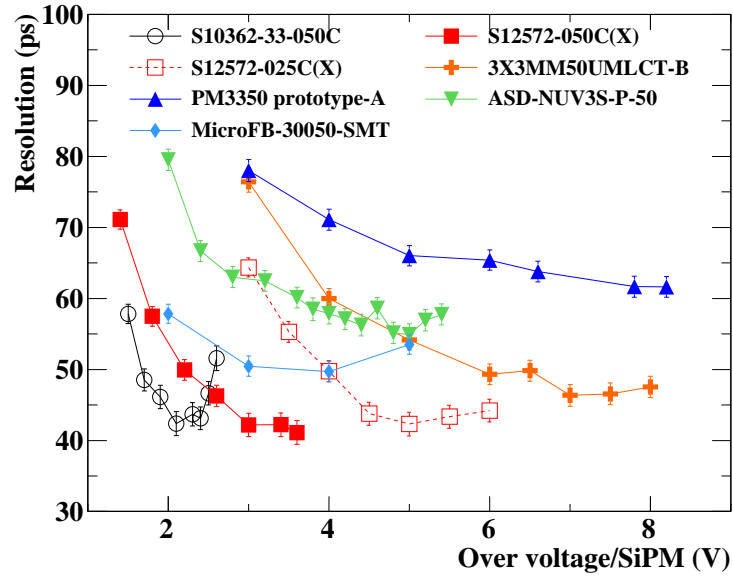
Figure 4.13: Time resolution dependence on manufactures. Scintillator is $60{\times}30{\times}5$ mm^3 of BC422. Three SiPMs are attached at both ends of scintillator.
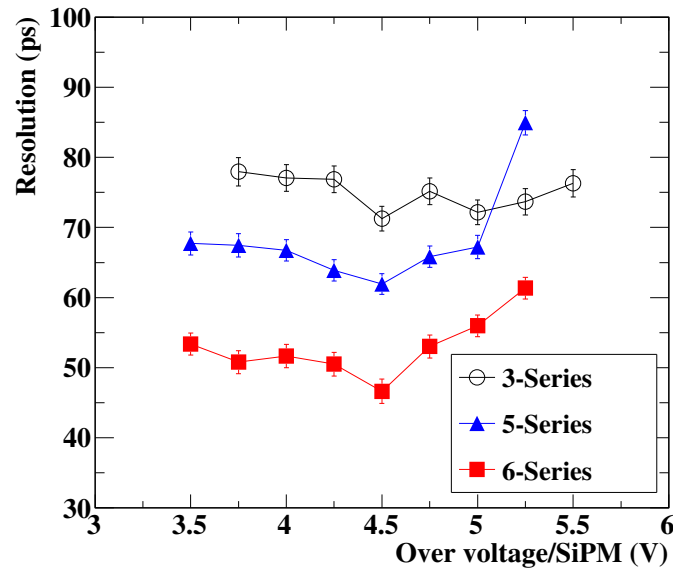
Figure 4.14: Time resolution dependence on number of SiPMs. BC422 scintillator of size of $90{\times}40{\times}5$ mm^3 attached 3, 5, and 6 AdvanSiD SiPMs (NUV3S-P-50) in series.

4.5 Property of Single Counters

In this section, properties of the single counter will be described. Before single counter assembly, each component of the counters such as SiPM, SiPM array, and scintillator is tested. Selecting better stuff by the tests, mass production of the counters is performed. Finally we confirmed the counter property such as time resolution and position dependence by mass test for all the counters.

4.5.1 Measurement of Single Counter Resolution

We started mass production of the counters in 2014. Before that scintillators and SiPMs are tested separately. Here the basic test set up for scintillator, SiPM, and assembled counter is shown before showing each result in detail.

Test counters are irradiated by β-ray from ^{90}Sr sources whose energy is < 2.28 MeV and intensity is 250 kBq or 3.7 MBq. Intensity is tuned to be the same by changing the distance of the source. Set up is shown in Fig. 4.15. By triggering with hits ($E_{deposit} > 0.5$MeV) on a small reference counter ($5\times5\times5$ mm^3) placed behind of a test counter, only electrons penetrating test counter is selected. In MC mean of energy deposit in the test counter is estimated to be 0.95 MeV. The scintillator of the reference counter is BC422 wrapped in Teflon tape, and one SiPM (HAMAMATSU, S10362-33-050C) is attached. The signal is propagated by 7.4 m coaxial cable to an amplifier developed in PSI and then reaches DRS4 digitizer. The circuit of amplifier is described in Fig. 4.16. It is voltage amplifier, and also takes a role of a pulse shaper in which pole-zero cancellation is applied for signal to be sharper. Via the amplifier bias voltage is applied to SiPM arrays by picoammeters (KEITHLEY 6487 PICOAMMETER/VOLTAGE SOURCE).
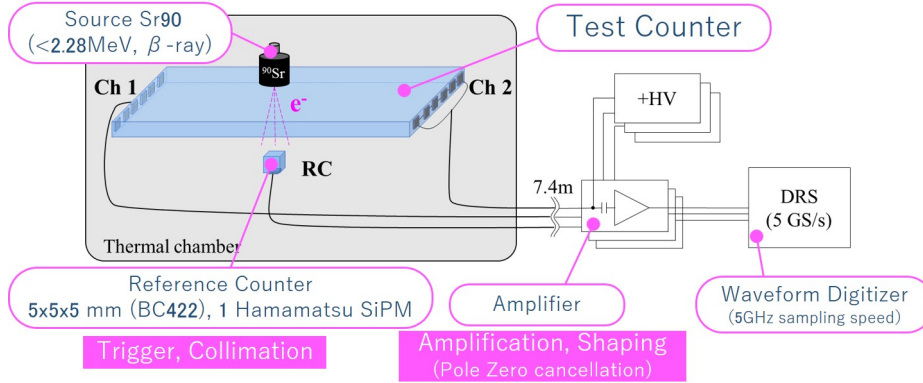

Figure 4.15: Single counter test set up.

In analysis to select the high energy electron from the source, a charge cut in reference counter is applied. The resolution is estimated from the distribution of the time difference between the test counter and reference counter. The resolution of the reference counter is estimated to be 30 ps. Subtracting the reference counter resolution, the resolution of a test counter is obtained.

4.5.2 Scintillator

We obtained 400 scintillator plates of $120\times50\times5$ mm^3 and 600 plates of $120\times40\times5$ mm^3 by cutting 7 original plates. We observed that each scintillator plate has different light yield
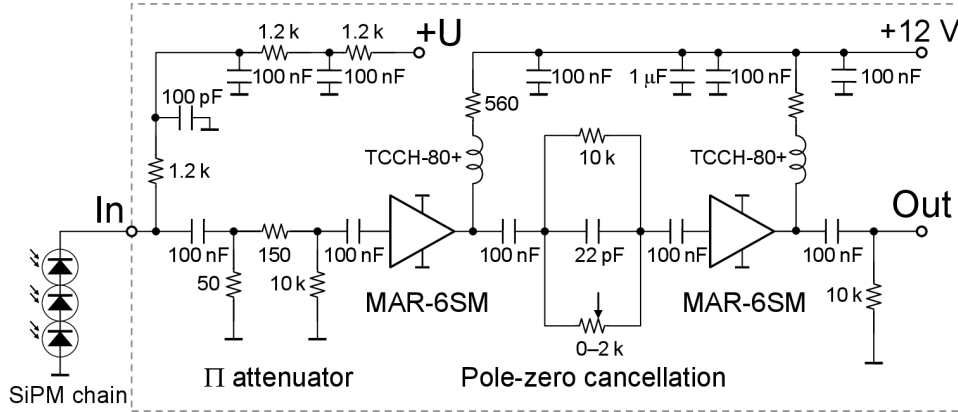
Figure 4.16: Circuit of amplifier developed in PSI.

and the resolution of the counter made of the lower light yield plate was worse as shown in Fig. 4.17. The test set up obtaining the figure is the same as described in Sec. 4.5.1, and test scintillators were attached to the same SiPM array by optical grease. Since it takes too much time to check the resolution of all scintillator plates, one side measurements as described in Fig. 4.18, in which only current readout by SiPMs is checked, are performed at room temperature. The measured currents clearly correlate to the time resolutions as show in Fig. 4.19. The resolutions of the other original plates are also distributed from 60 to 100 ps for 4 cm-height-counters, and from 70 to 110 ps for 5 cm-height-counters. Therefore selection of scintillator plate bases on the one-side measurement by choosing in order from the high current plates.
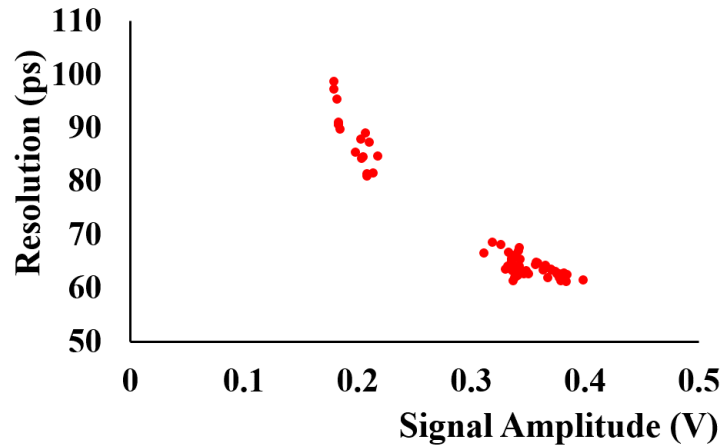
Figure 4.17: Correlation between signal amplitude and resolution with several scintillator plates ($120{\times}40{\times}5$ mm^3) from two original plates. In all measurement of these plot the same SiPM array is used.
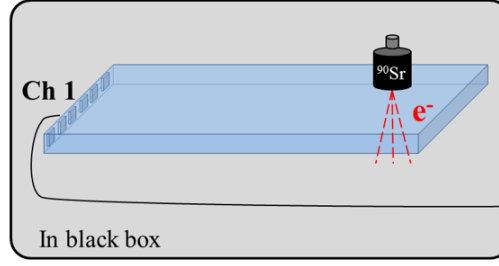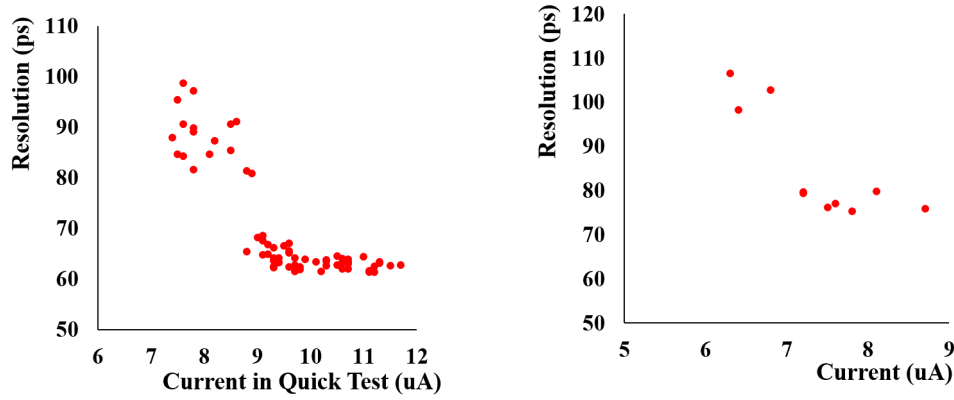
Figure 4.18: Set up for testing the scintillator light yield by SiPM current.

Figure 4.19: Correlation between the resolution measured in counter test set up, and the current from one-side measurement. The size of scintillator is $120\times40\times5$ mm^3 (right) and $120\times50\times5$ mm^3 (left) scintillators from two original plates).

4.5.3   Silicon Photo Multiplier

Single SiPMs

We used two types of SiPM (ASD-NUV3S-P High-Gain(MEG), and ASD-NUV-SiPM3S-P) from AdvanSiD, because the production line of the first type (Type 1) was closed. For almost all counters the first type is used, but SiPMs for 40 counters are second one (Type 2). IV curves are measured for all of single SiPMs. The results of type 1 is shown in Fig. 4.21. We found two different IV behavior in the first version of SiPM though their break down voltages are stable as shown in Fig. 4.20. 45.5 % of Type1 SiPMs show faster brow up of the current than the others because the former has the larger dark current. Fig. 4.22 shows the current at over voltage of 3.05 V. Some group (Type1-1) have lower dark current, but that in the other group (Type1-2) spread in wide range. Therefore optimal operation range of HV for Type1-2 is narrower than that for Type1-1. On the other hand, the current of Type 2 (ASD-NUV-SiPM3S-P) with voltage increases slowly which allows wider operation voltage range as discussed in the next section.

Array of SiPMs

Six SiPMs for an array are chosen to have close current at over voltage of 3 V. The selected SiPMs are soldered to the PCB designed for TC shown in Fig. 4.23. A non-
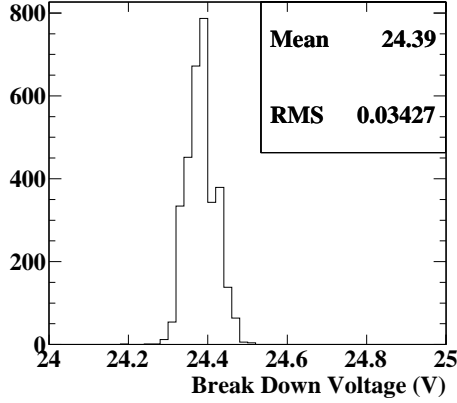
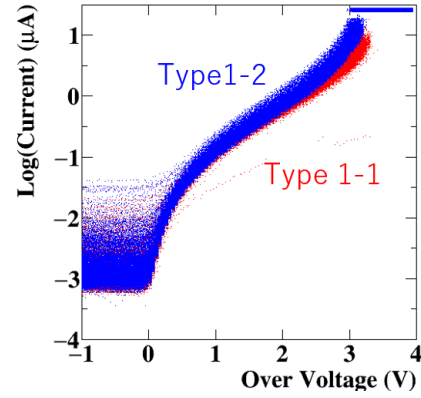Figure 4.20: Breakdown voltage of all the single SiPMs of Type 1.

Figure 4.21: IV curves of all the single SiPMs of Type 1.

magnetic connector is also soldered to a PCB. Three types of the PCB are prepared for straight for 4 cm-height-counter and 5 cm-height-counter, and L-shape for the counters installed inner step of COBRA due to limited space.

IV measurements of the SiPM arrays are also performed for the all arrays. To extract the maximum performance of SiPM arrays, the optimal bias voltage is decided based on results of counter bias scanning with several SiPM arrays. Basically the optimal bias voltage is decided by a trade-off between signal-to-noise ratio and dark current of SiPM. On one hand, low bias voltage makes signal amplitude low and then noise affects the resolution to be worse. On the other hand, high bias voltage increase the dark current which also makes the resolution worse. Therefore the optimal voltage depends on the environment. Though we should tune the optimal voltage in the real experiment site, we performed bias scanning in a different room, which is more quiet than the MEG II experimental site, to decide the nominal operation bias. Fig. 4.24 shows the result with Type 2 SiPM whose resolutions are stable over bias voltage from 3 to 5 V. It means that even if the noise becomes large the best resolution can be kept. On the other hand, Type 1 has steeper IV curve, which result in a narrow optimal range of the bias voltage especially Type 1-2 as shown in Fig. 4.25. Therefore optimal voltages should be decided one by one. After the counters were assembled, bias dependence of the resolution with 16 counters with Type 1 SiPMs were measured as shown in Fig. 4.26. As a result from fitting the dependence with the quadratic function of $a \times (v - p)^2 + q$, where v is over voltage, optimal range is obtained by defining it as a region where the time resolution is within 2 ps from the best value as shown in Fig. 4.27. Since the common region lays in a current range from 3 μA to 5 μA, finally operation voltages are adjusted to the same current point of 4 μA in IV curve.

The variation of SiPM performance is not small as shown in Fig. 4.28. It can be checked by the one-side measurement in Fig. 4.29 same set up of scintillator quality check but by checking its signal amplitude not its current because it depends on each SiPM IV behavior. The result is shown in Fig. 4.30 and we observed the fluctuation of the light yeild. The resolution variation of 5 cm-height-counter is expected about 74-92 ps for example. Though we observed such a large variation of the performance, due to limited number of SiPMs almost all SiPMs are used for the counters. Combinations of two SiPM arrays for each counter are chosen to have similar properties such as IV curve and signal
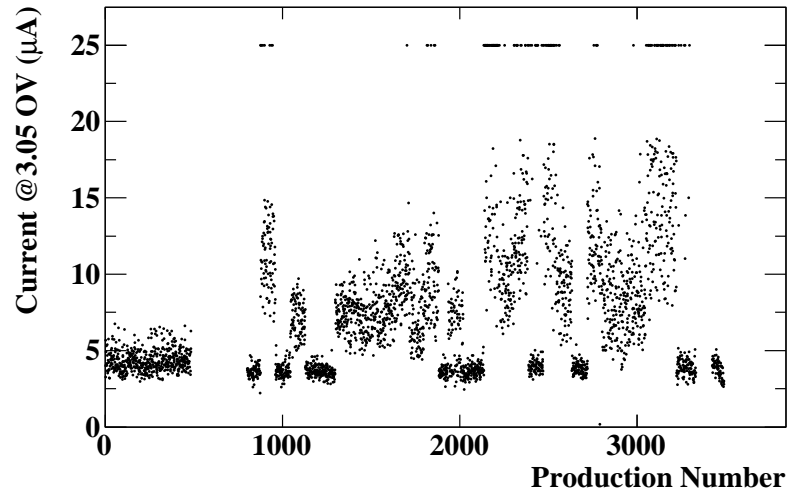
Figure 4.22: Current at OV $\bar{3}$.05 V. Saturated point of the IV measurement is 25 μA.
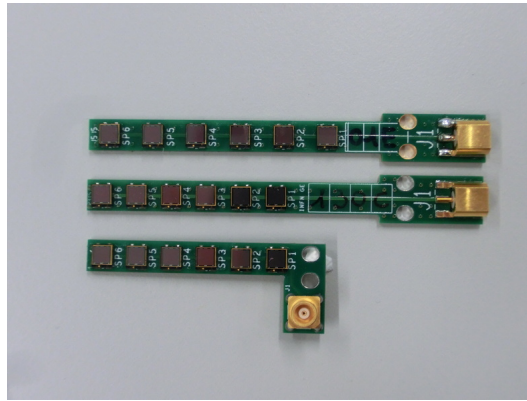

Figure 4.23: PCBs for SiPM arrays. Three types are prepared for 5 cm height (top), 4 cm height (middle), and L-shape (bottom)
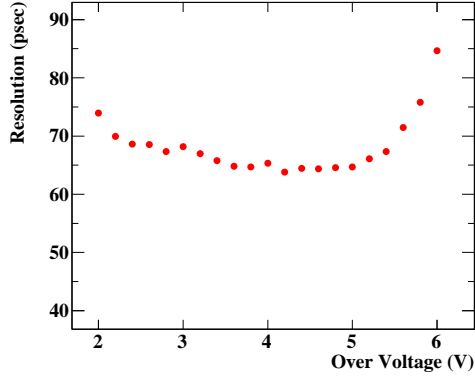
amplitude in one-side measurement.

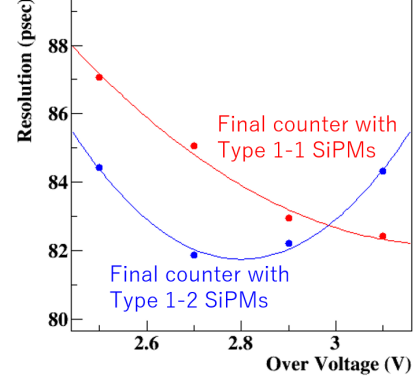Figure 4.24: The resolution dependence on bias voltage of Type 2 SiPM.

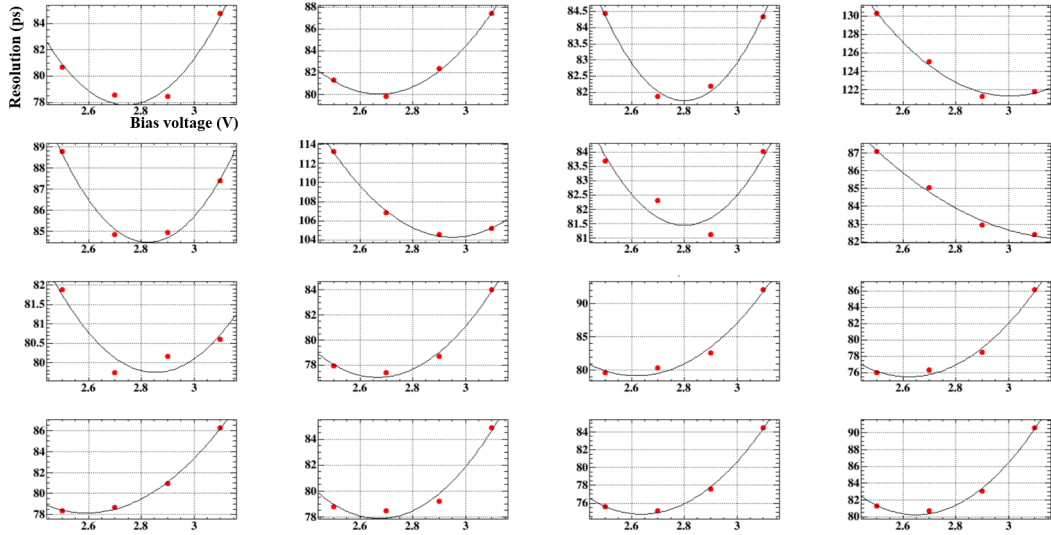Figure 4.25: The resolution dependence on bias voltage of Type 1-1 and Type 1-2 SiPM.

Figure 4.26: The resolution dependence on bias voltage of Type 1 SiPMs. They are fit with $a \times (v - p)^2 + q$ where v is over voltage.
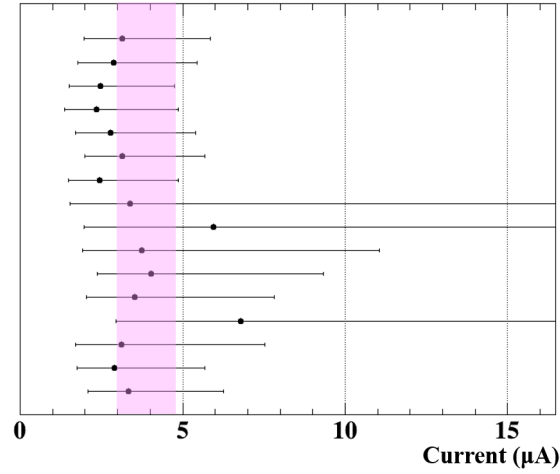
Figure 4.27: The optimal point and range as a function of current in IV curves. Colored band describes common optimal range over all 16 counters.
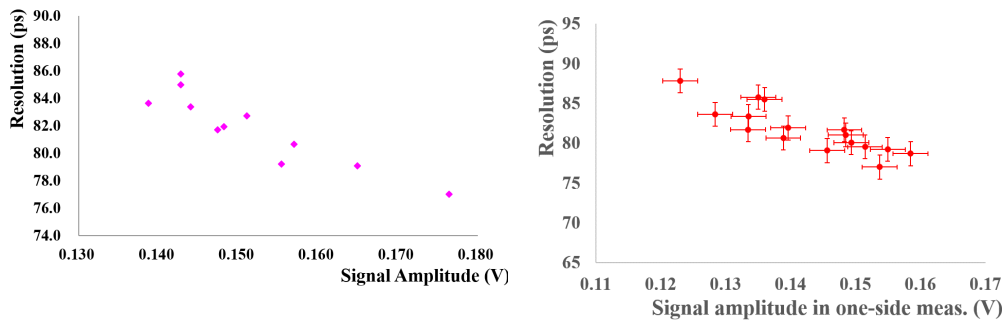

Figure 4.28: Resolution and amplitude of the counters with several SiPM array attached to the same scintillator plate ($120 \times 50 \times 5$ mm^3).

Figure 4.29: Correlation between signal amplitude from the one-side measurement and the resolution.
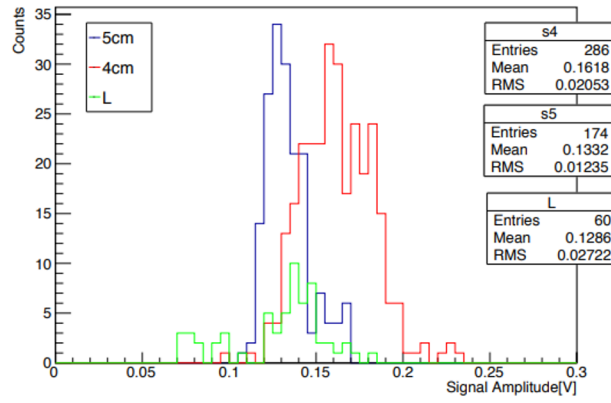
Figure 4.30: Signal amplitude in one-side measurement. SiPMs. Half of all SiPM arrays are measured. Red line shows the result of SiPMs for 4 cm-height counters; blue line for 5cm; and green line for L-shape.

4.5.4   Single Counter Assembly

Single counters are assembled one-by-one by hand. Optical cement (BC600) is used to attach the SiPM arrays to the scintillator. To remove void in the cement, it is evacuated and heated. The schematic of the assembly tool is shown in Fig. 4.31. Taking into account variation of thickness of scintillators, SiPM position is adjusted to be on the center of the scintillator. After SiPM attachment, scintillator is wrapped by the reflector and then the bar for the fiber insertion and the thermal links made of aluminum are attached. At the end, the fibers are installed and light shielding is completed. For the shielding polyvinyl fluoride film (Tedlar®) and black tape are used. These process is summarized in Fig. 4.32.
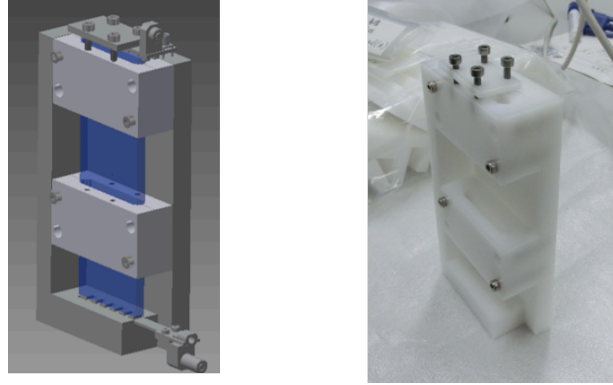

Figure 4.31: Schematic of assembly tool (Left) and its picture (right).
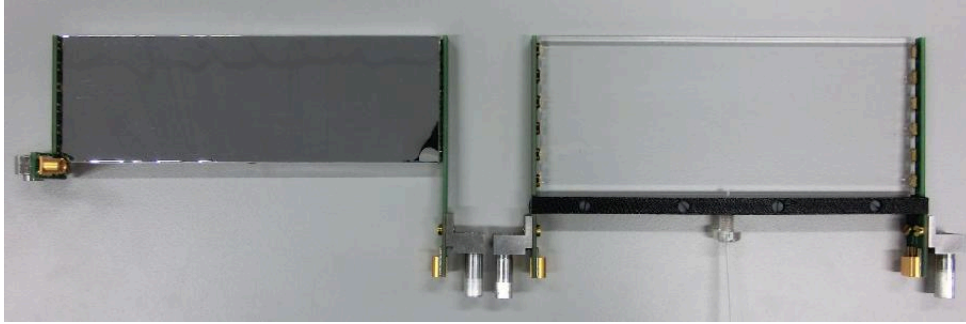

Figure 4.32: Picture of assembled counters.

Detachment Problem

We found detachment between scintillator plate and SiPM array as shown in Fig. 4.35 after the pilot runs in 2015 and 2016. In particular, a lot of 5 cm height counters had the detachment as shown in Fig. 4.33 and a lot of detached SiPMs are located the bottom or the top as shown in Fig. 4.34. The possible reason is the distortion of the SiPM array as described in Fig. 4.36. The mismatch between the counter interval and the connectors on support structure causes the force to peel off the SiPMs. We also find that once small air-gap appears it is easy for SiPM to be detached.

In the last pilot run in 2017 the precision of the support structure was improved (see Sec. 4.8 in detail). Moreover to strengthen SiPM array mechanically against the distortion, additional optical cement is put between some SiPMs and the top and bottom of the array as described in Fig. 4.37. The scintillator surface where the additional optical cement is put is scratched with a thin jig-saw to reinforce the adhesiveness.
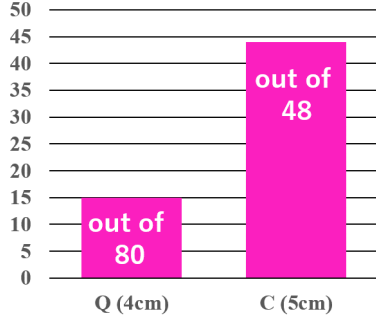

Figure 4.33: Number of detached counters which have more than one detached SiPM.
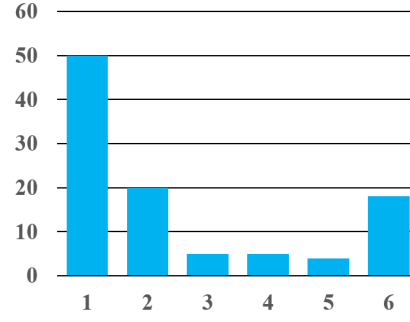

Figure 4.34: Location of detached SiPMs. Numbering is in the order from the bottom.
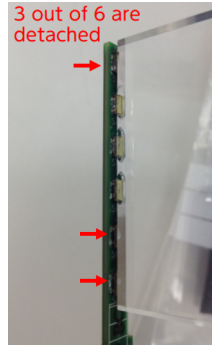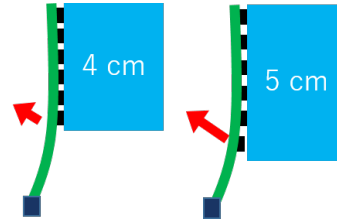

Figure 4.35: Picture of SiPM detachment.

Figure 4.36: Schematic drawing of distortion which induces detachment of SiPMs.

Fiber Insertion

Fibers for laser calibration are inserted to 432 counters which are all counters except for the counters at the inner COBRA step. Since the calibration is sensitive to the amount of inserted light, the fibers need to be inserted stably. A hole is drilled on bottom of the scintillator for the fiber tip. The fibers are fixed by special screws fixed in the bar which is placed at the bottom of the counters as shown in Fig. 4.39. The schematic of the screw is shown in Fig. 4.38.

4.5.5 Single Counter Performance

The final performance of the counters are measured with β-ray from ^{90}Sr source as explained in Sec. 4.5.1. The time resolutions from this measurement is summarized in

Figure 4.37: Schematic of additional treatment against detachment.

Figure 4.38: Schematic of fiber insertion method.

Figure 4.39: Picture of counter inserted fiber.

Fig. 4.40. The mean values of the resolutions are 72.35 ps and 80.70 ps for 4 cm and 5 cm height counters, respectively.

Dead Counters

Out of ∼550 assembled counters, there are ∼20 dead counters except for mechanically broken ones by human error. One of the channels in the dead counters suddenly have no current, no signal or small signal. Some of them are caused by the mechanical force because when we pushed the SiPM array these channels worked properly from the output current point of view. We rejected these counters and the other side channels are recycled to the different counters.
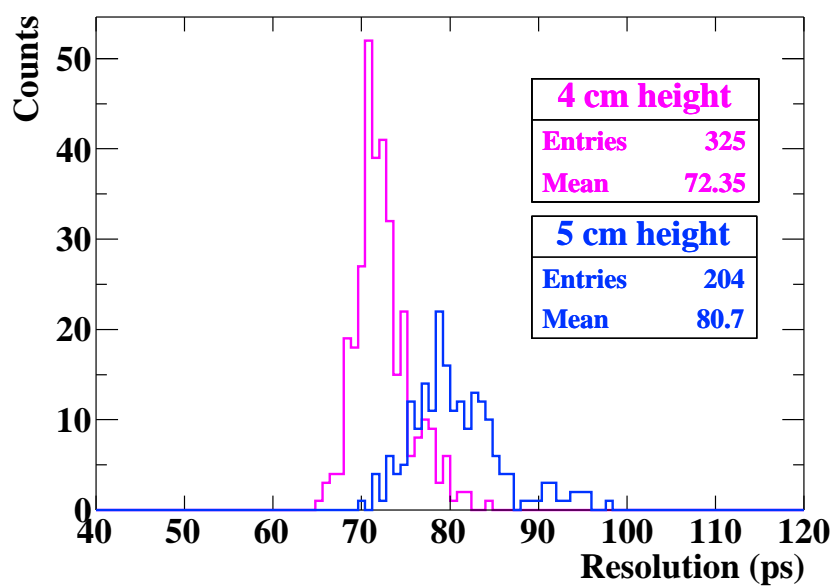
Figure 4.40: Resolution distribution of single counters. Magenta line show that of 4 cm height counter; Blue line, 5 cm.

4.5.6   Radiation Hardness

Generally the radiation damage concerns the high energy physicist. It is known that SiPM are damaged by heavy particles, gamma-ray, and charged particle such as electrons and positrons. TC has the radiation damage from Michel positron at <100 kHz as discussed in Chap. 7. Assuming the total DAQ time in the MEG II physics run to be 75 weeks, the total flux is estimated as 9.5×10^{11} e^+/cm^2. The radiation test is performed with a test beam for Type 2 SiPMs and with ^{90}Sr source for Type 1 SiPMs. The time resolutions of both of the irradiated SiPMs are measured with the same set up as described in Fig. 4.5.1 at 30 degree. The resolution is estimated by the time difference between the reference counter and the irradiated channel.

The irradiation by ^{90}Sr source is separated into 4 times. Since the flux cannot be estimated directly, the increase of the SiPM current becomes the reference of the irradiated flux. In the MEG II environment, the current increase is expected to be ~ 100 μA. Fig. 4.41 shows the IV curves at the each irradiated point. The radiation damage increases the dark noise of SiPM as shown in Fig. 4.42 and Fig. 4.43, therefore the current increases with the radiation damage. The resolution degradation can be seen in Fig. 4.44 and Fig. 4.45.
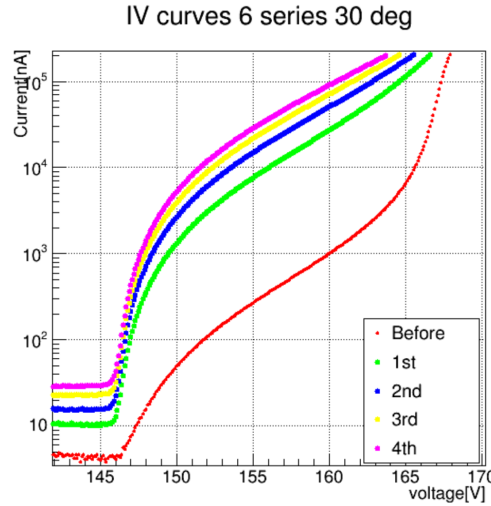

Figure 4.41: IV curves of a SiPM array with irradiation.

On the other hand, the SiPMs of Type 2 are irradiated by the positron beam in Beam Test Facility (BTF) in Italy. The resolutions after irradiation with the total flux of 1.1×10^{12} e^+/cm^2 is shown in Fig. 4.46. Though the total flux is one order of magnitude higher than the MEG II expectation, this resolution level of ~ 140 ps is similar to the 1st irradiation of Type 1 SiPMs as shown in Fig. 4.45. Therefore the radiation damage of Type 2 SiPM is not larger than that of Type 1 SiPM.

In conclusion, the radiation damage makes the resolutions of SiPM worse in the MEG II experiment. However cooling reduces the dark current so effectively the resolution degradation by the radiation damage is reduced by cooling. Fig. 4.46 also shows the time resolutions measured at 10 degree. It indicates that the resolutions improved by cooling down to 10 degree. Therefore the cooling system for TC is installed as described in the following section.
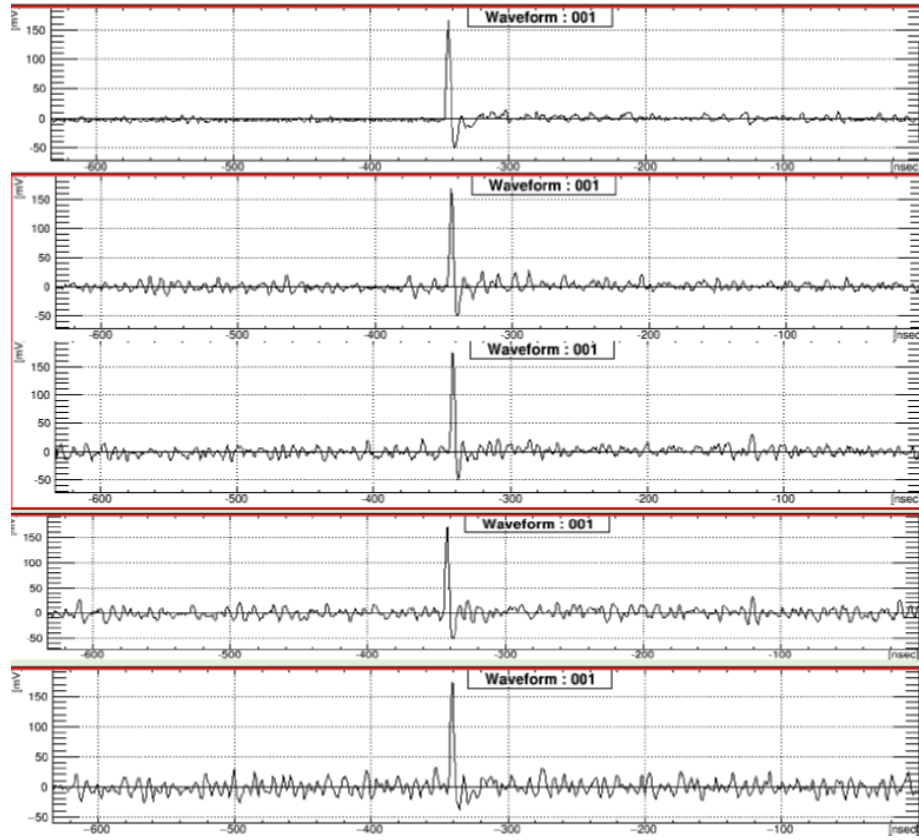
Figure 4.42: Waveforms in Sr radiation test. The top is waveform before irradiation, and the total flux is increased to the bottom.
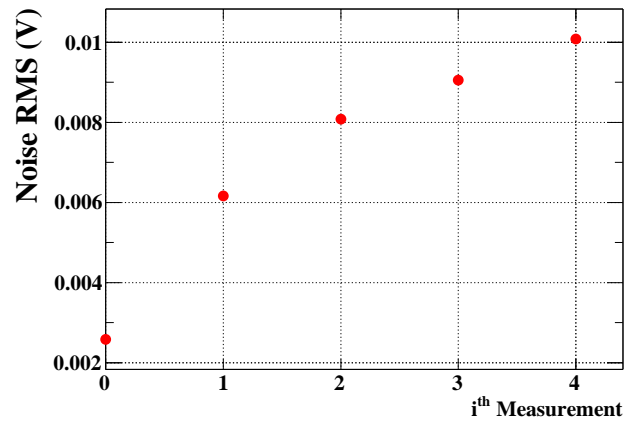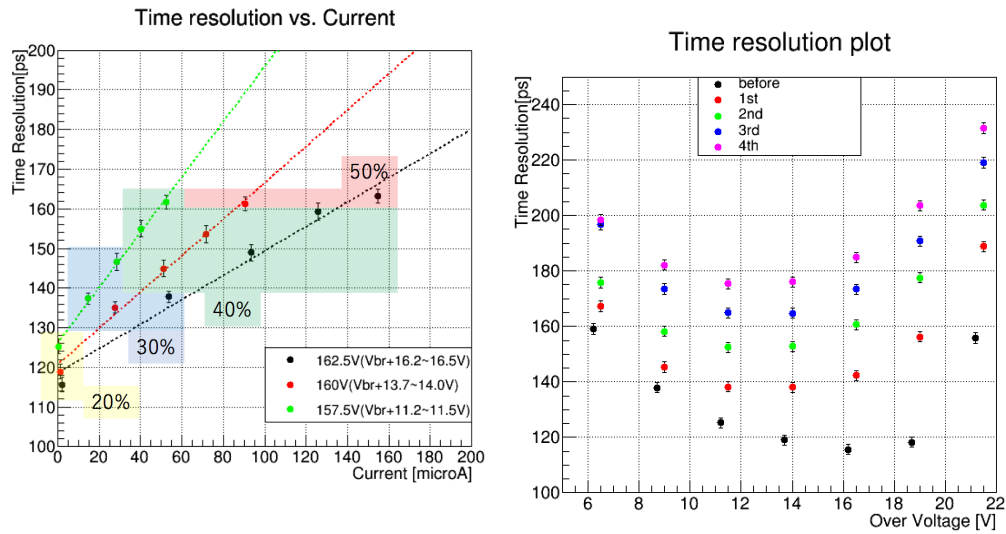

Figure 4.43: Noise level with irradiation.

Figure 4.44: Resolution vs current in ^{90}Sr radiation test. Each color indicates the different applied voltage. Analysis is optimized at the each point.

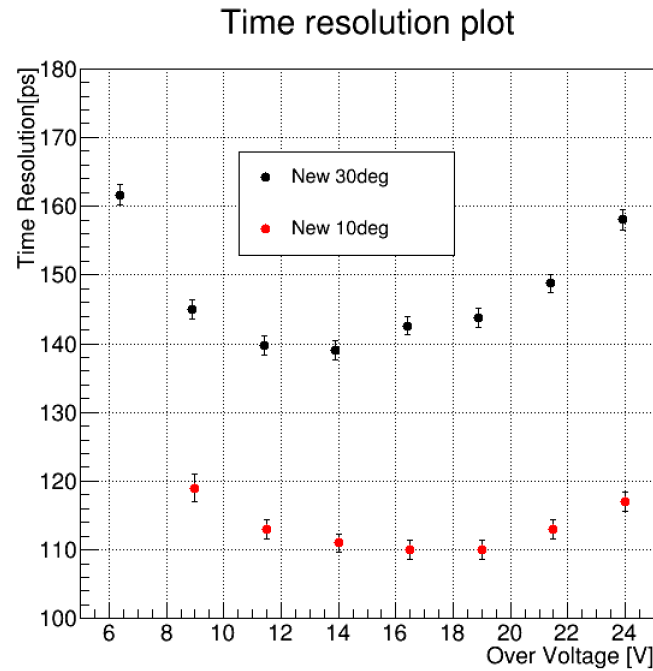Figure 4.45: Resolutions with over voltage with each irradiated point.

Figure 4.46: Resolutions with over voltage of SiPMs irradiated by positron beam.

4.6   Readout Electronics

The signals from the counters are propagated by BP and the 7 m coaxial cables and then amplified, shaped, and digitized in WD as described in the previous chapter. From the TC point of view, the time resolution is most important and set up of WD is optimized to realize the best time resolution. In the WD pole-zero cancellation is applied, because sharper waveform has better time resolution and the smaller tail can suppress pile up effect. Moreover the time resolution depends on the sampling speed of WD as shown in Fig. 4.47. The sampling speed is limited by trigger and it is planned to be 1.8 GSPS.
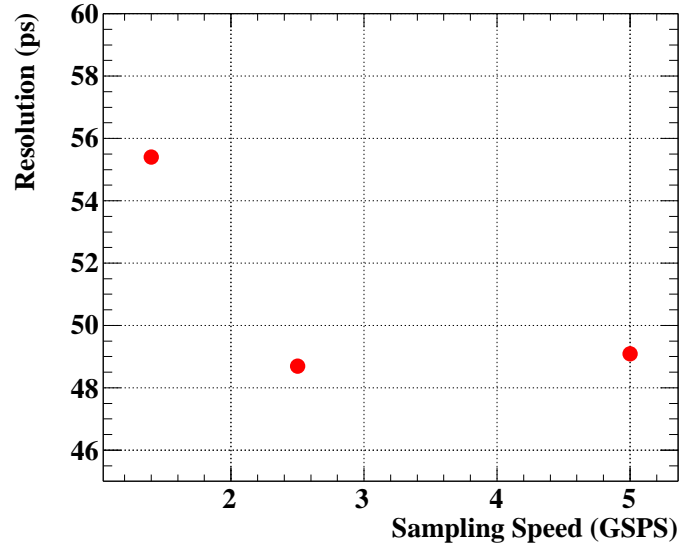

Figure 4.47: Resolutions dependence on sampling speed.

4.7   Laser System

There are two methods for time calibration among counters to be discussed in detail in the next chapter. One method is the laser calibration in which split laser light is injected to bottom of the counters. The overview of the laser system is shown in Fig. 4.48. Limited space at the inner step of COBRA magnet does not allow all the counter to be equipped with fibers, so 432 counters out of 512 counters can be calibrated by the laser calibration. Since the laser power is not high enough to be distributed to all the laser counters simultaneously, an optical switch is used to separate the laser counters into 8 sectors. One sector has 50-60 laser counters. The laser light is supplied to the counters by the optical fibers via the two passive splitters which divide up the light among 64 fibers. After the optical switch placed outside of the experimental area, the laser pulse is transmitted to the first splitter in the experimental area by the 10 m optical fibers and then 2.5 m fibers distribute the pulse to the second splitters and the counters. The laser synchronized pulse is also supplied to the DAQ electronics as the reference time to calibrate the time offset of each counter. To monitor the stability of the laser light, a photo diode is prepared and its signal is also readout. The frequency of the laser pulse and the optical switch are controlled via MIDAS system. To install the laser system in

the limited space, the splitter boxes and winding tool are prepared as shown in Fig. 4.49. For the safety, the fibers are covered by tubes.
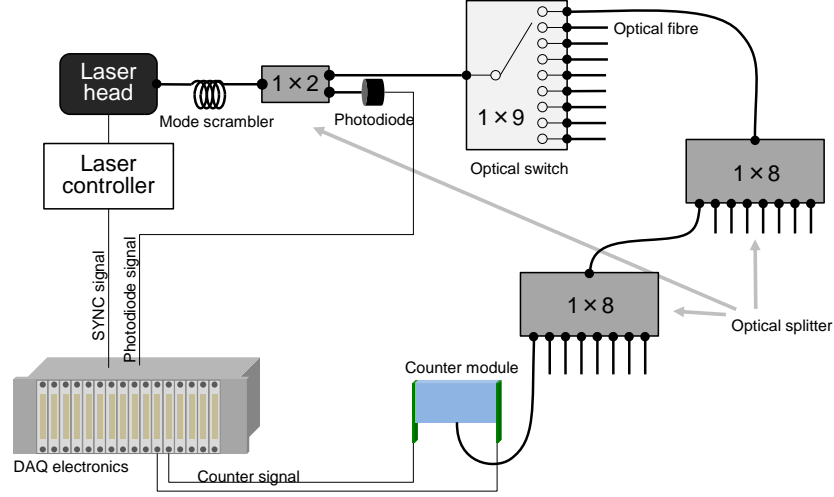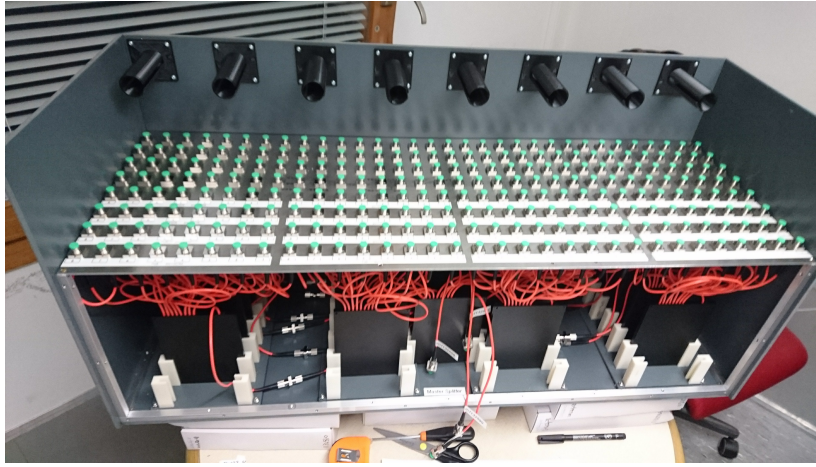

Figure 4.48: Schematic of laser calibration.

Figure 4.49: Picture of splitter box.

4.7.1 Time Offset of Laser System

To subtract the intrinsic time offset from the laser system which comes from the variation of the fiber length and amount of light of the splitter output, the offsets from just after the optical switch to the counters are measured in advance. The result is shown in Fig. 4.50. The splitter output depends on the manufacturing batch, so in US the large fluctuation is observed.
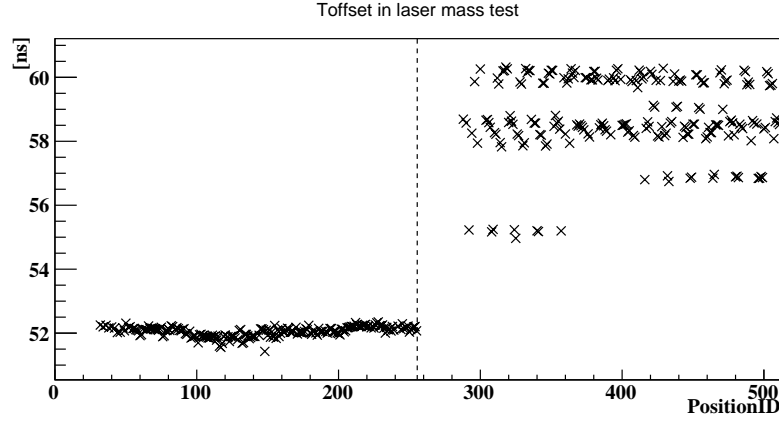
Figure 4.50: Time offset in laser system. The difference of the splitter batch makes the fluctuation of the time offset in US.

4.8   Assembly and Installation

4.8.1   Support Structures

The TC support frame with long PCB (948×25 mm^2) called backplane (BP) are shown in Fig. 4.51. The BP is fixed on the frame by screws. Counters are mounted to non-magnetic connectors on the BPs and also fixed on the support frame by screws via the thermal links.
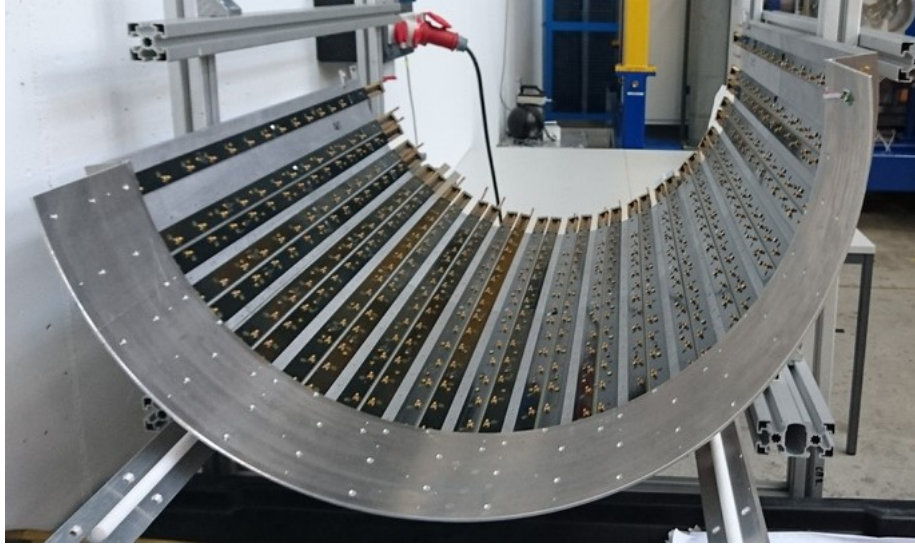

Figure 4.51: The picture of support structures. The backplanes are placed on support frame.

Support Frame

The support frame is made from an aluminum cylinder to achieve high machining precision because the prototype frame which made from a plate had unacceptable distortion. The frame is composed of the 4 parts as shown in Fig. 4.52. Three parts are main part of

TC, while the other is the frame for the counters at the inner COBRA step. The main parts of the frame have the grooves to put the BPs. Fig. 4.53 shows xy view of the frame. Backside of the frame also has grooves for cooling piles as described in detail later. The frame also has screw holes to fix the counters via the thermal links and through holes to insert the fibers for the laser system. Fig. 4.54 shows the backside of TC after finishing assembly. The cooling pipes and fibers are installed.
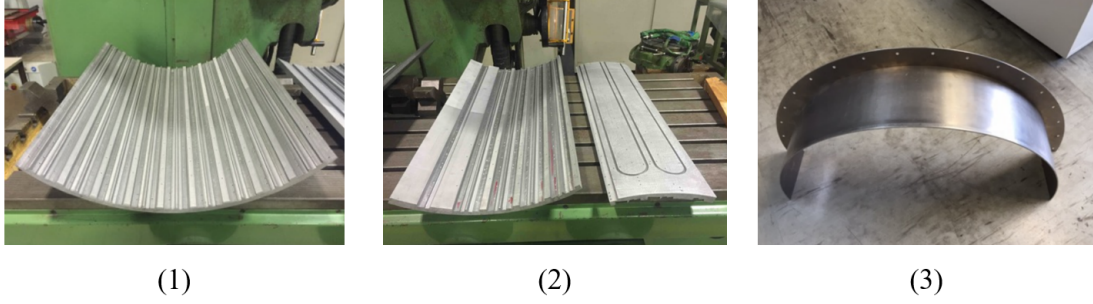

(1)   (2)   (3)

Figure 4.52: Picture of support frame. (1) Middle part ($< \phi <$) in main part of the frame. (2) Smaller (right) and larger (left) ϕ part (ϕ and ϕ). Small ϕ part is turned over. The backside has groove for cooling pipe. (3) Frame for COBRA inner counters.
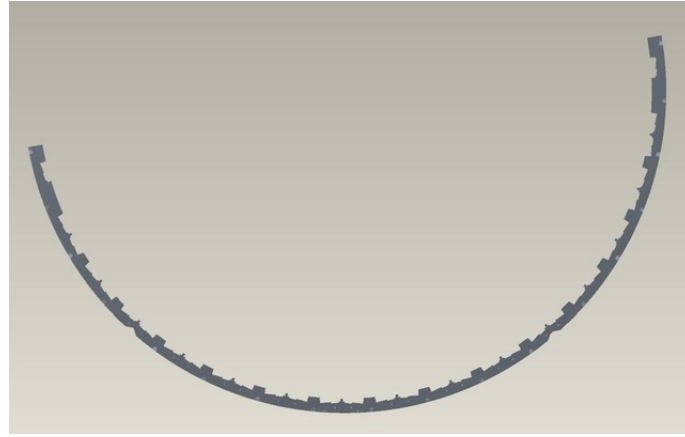

Figure 4.53: xy view of the main support frame.

Backplane

Fig. 4.55 is the picture of BPs and the drawing of the signal line in the BP is also shown in Fig. 4.56. One BP is put along z and transmits the signals from the channels of one side of 16 counters and two additional channels for thermometers and hygrometers (Sec. 4.9 in detail). We put 64 BPs on DS and US support frame. To reduce noise in the signal lines, they are sandwiched with two guard layers as shown in Fig. 4.57. The BP has 18 layers and each of the three layers composed two guard layers and signal layer for three channels. The schematic of the ends of the BP is shown in Fig. 4.58. The signals from counters at the inner COBRA step are transmitted by cables (RG178) to inner end of the

Figure 4.54: Backside of the support. Cooling piles and fibers fixed by tape are installed

BP. The every signal from SiPM arrays are output to cables (RG178) at the outer end of the BP. Every connectors on BP are non-magnetic ones. The cables are 7.4 m long and transmit the signal to the WaveDREAM in which the signals are shaped and amplified.

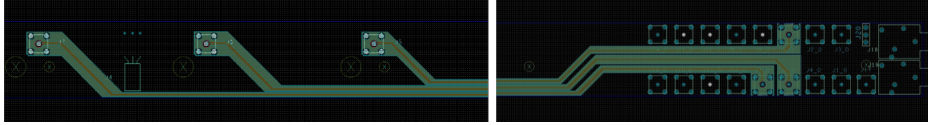Figure 4.55: The picture of the backplane.

Figure 4.56: Signal lines of three channels in the backplane.

4.8.2 Counter Assignment and Assembly

The counter assignment is decided based on the property of the IV curves and the time resolutions. As discussed above the radiation damage of the SiPMs increases the dark noise, which induces the resolution deterioration at the higher over voltage. As a result, the optimal range of the bias voltage defined in the previous section becomes narrower. Therefore at the position having relatively higher rate of Michel positrons, the counters with the smaller dark current SiPMs are assigned. All of Type 2 SiPMs, which have large optimal range, are used for 5 cm height counter. Considering that the voltage can be applied in the range of 4 V in one WD and the difference of the optimal voltage between Type 1 and Type 2 is more than that, Type 2 counters are assigned to the positions with the high Michel positron rate as shown in Fig. 4.59. In the Type 1 SiPMs, as discussed above, Type 1-2 has larger dark current than Type 1-1 has. Therefore, the Type 1-1 counters are assigned to the higher rate positions as shown in Fig. 4.59. In the assignment

Figure 4.57: Three layers of top (red), inner (blue), and bottom (green) layers.

by the type each counter is assigned based on its resolution. With the hit probability of the signal positrons expected from MC, the better resolution counters are assigned to the higher probability position as shown in Fig. 4.60

Following the assignment of the counters, the counters are mounted one by one. The counters with the straight shape of the SiPM arrays are fixed by the two thermal links and the connectors as shown in Fig. 4.61 while the connectors are not used for the L-shape SiPM arrays as shown in Fig. 4.62. The overview of the assembled TC is shown in Fig. 4.63.

4.8.3 Installation

TC is installed by the rail system as shown in Fig. 4.64. The support frame has the two groove for the rail system. By the system the maintenance work of TC is also done independent of DCH easily.

4.8.4 Alignment

For the global alignment of TC to the MEG II coordinate, reference points are attached on the TC support frame as shown in Fig. 4.65. The cube put on the reference points is viewed by laser tracker. On the other hand, for the internal alignment of the each counter, the top of the counters is scanned by 3D scanner.

4.9 Slow Control System

All of slow control system for TC is based on MIDAS system.

4.9.1 High Voltage Control

The high voltage control and the current monitor for TC SiPMs are implemented in the MEG II MIDAS system. IV curves for all SiPM arrays are also obtained simultaneously by the system.
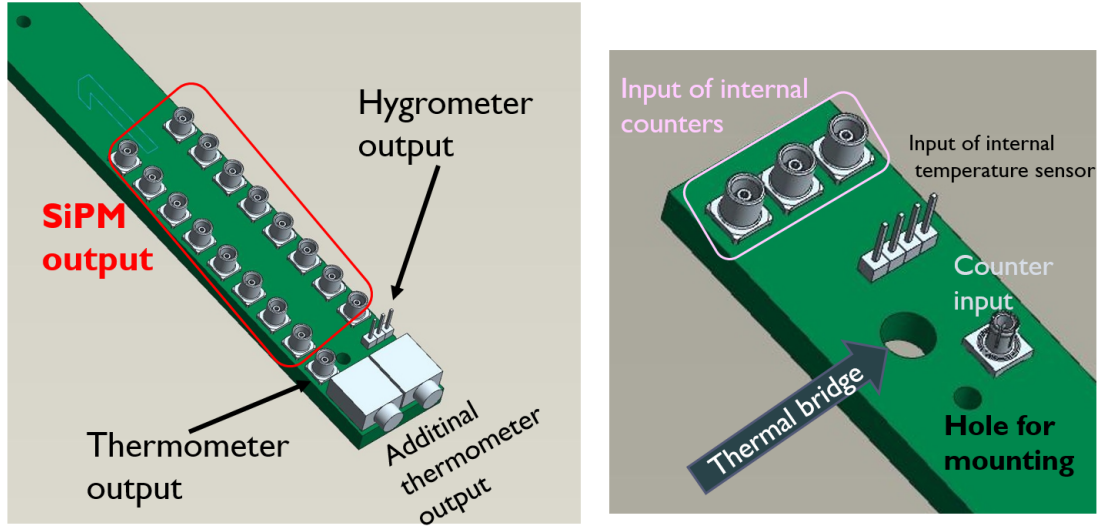
Figure 4.58: Drawing of the BP both ends of outer z side (left) and inner z side (right).

4.9.2   Temperature and Humidity Control

As discussed above, the dark current of SiPMs can be suppressed by cooling. Water cooling system is installed. The chiller (CustomChill, CRAL300-230PE) with 400 W cooling power provides cooled water to the pipes which are placed backside of the support frame. The water cools whole of the support structure and the SiPM arrays is cooled via the thermal link, which touch the support structure. The cooling is possible to increase the humidity of TC. To avoid dewing, dry air is supplied.

The temperature and the humidity in TC are monitored via MIDAS system. Three thermometer are readout via one BP. Two of them are placed around the outer edge and middle point of the BP, and the other is on COBRA inner step. The sensor is 1-wire digital thermometer (DS28EA00) which is a serial protocol used by single line. One hygrometer (HIH4000) is also attached on the middle of the BP.
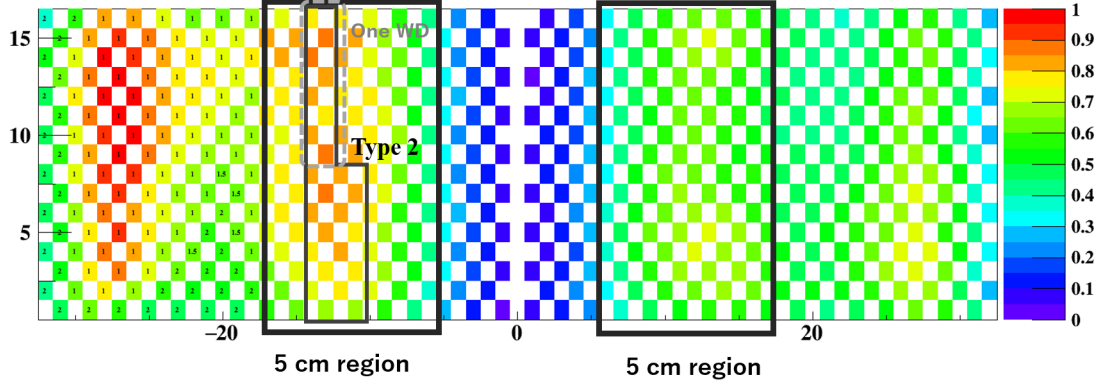
Figure 4.59: Counter assignment in US with Michel hit probability map. Each colored cell corresponds to a position of a counter. The color shows the rate of Michel positron rate scaled by the number of hits on the maximum hit counter. Numbers in the cell means the type of Type 1 SiPMs; 1 means Type 1-1; 2 for Type1-2; and 1.5 for Type 1-1 and Type 1-2 mixed counters.
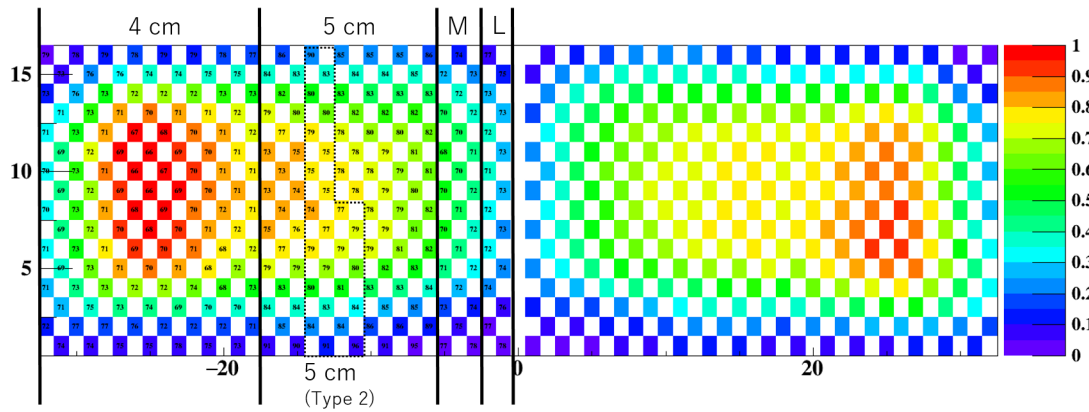

Figure 4.60: Hit probability of signal positron which gamma is accepted in LXe region. They are scaled by the number of hits of maximum hit counter. Written numbers are the time resolutions measured in the mass test with ^{90}Sr.
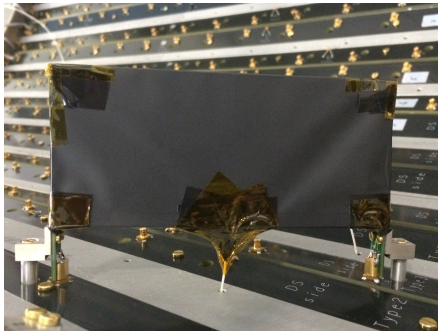
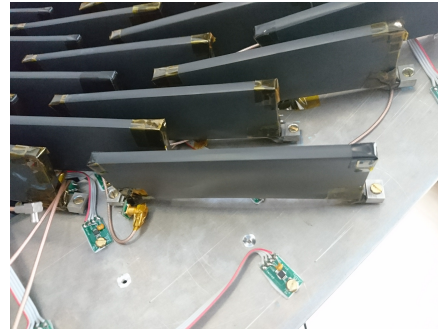Figure 4.61: Picture of the assembled counter.

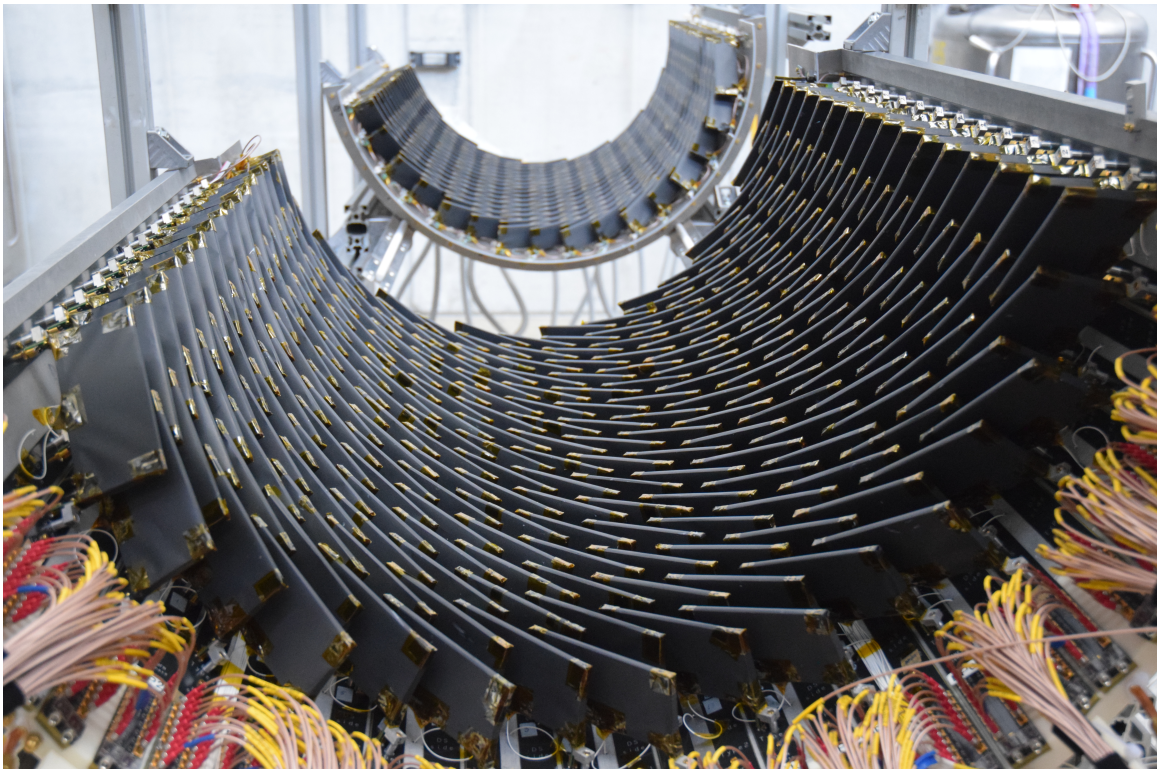Figure 4.62: Picture of the assembled COBRA inner step counter.

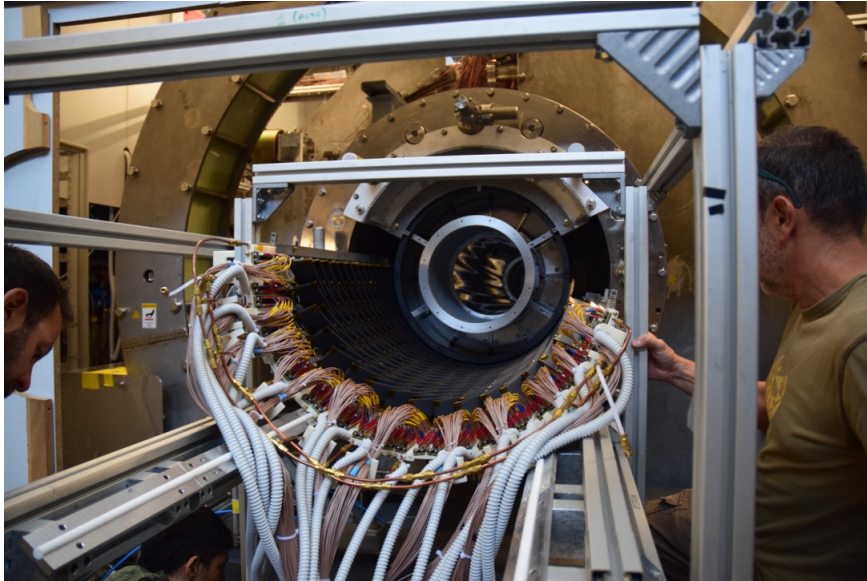Figure 4.63: Picture of overall view of TC.

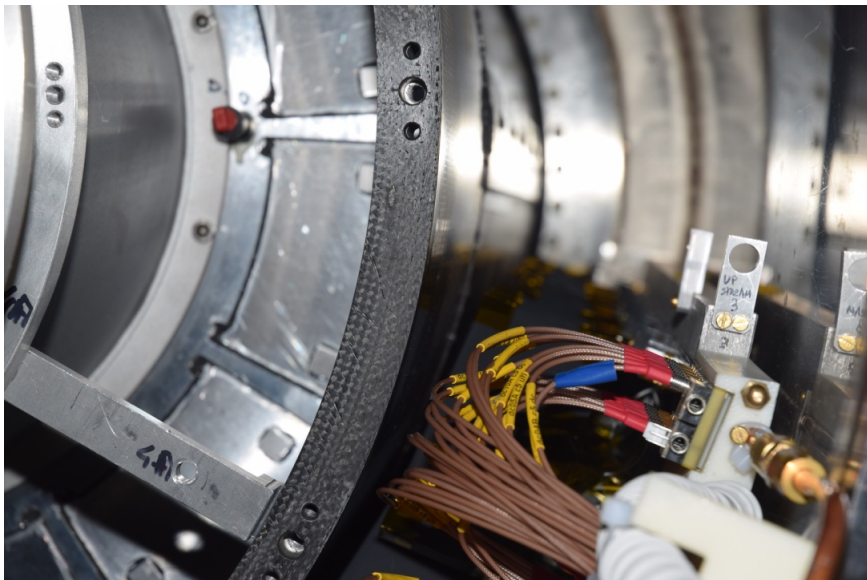Figure 4.64: Installation of TC into COBRA magnet by rail system.

Figure 4.65: Reference point for global alignment.

Chapter 5

Timing Counter Analysis

5.1 Time Reconstruction for $\mu \to e\gamma$ Search

One of the physical quantities reconstructed in the $\mu \to e\gamma$ search is $T_{e\gamma}$; which is the difference between reconstructed time of photon and positron $(T_\gamma - T_e)$ on the vertex. As discussed in Sec. 3.1, the precision of the time measurement is directly reflected in the sensitivity of the $\mu \to e\gamma$ search. While the photon time is reconstructed by the LXe photon detector alone, the positron time is reconstructed by combining the information of two detectors as,

$$T_e = \frac{\Sigma_i^n (t_i^{TC} - l_i/c)}{n} - L^{DCH}/c, \tag{5.1}$$

where i is a hit counter in TC when a positron hits n counters; l_i is the path length from the first hit counter in TC to the ith hit counter; L_{DCH} is path length from vertex to the first hit counter in TC reconstructed by DCH; and t_i^{TC} is the time measured by the ith counter in TC. Therefore the requirements for the TC analysis are

- Precise time extraction from the individual counters,

- Careful treatment of multiple hits,

Moreover though basically DCH reconstructs positron trajectory including l_i, there is room for a further improvement by utilizing the TC hit positions which are able to recover scattering effects on the reconstruction of the path length. From these points of view, reconstruction and calibration algorithms have been developed. The detail will be discussed in the following sections.

5.2 Reconstruction

Fig 5.1 shows overview of the positron reconstruction chain. At the beginning TC and DCH reconstruct positrons independently. When DCH finds tracks after the hit reconstruction, an initial time is needed and it is supplied by TC. On the other hand, the path length among the hit counters in TC cannot be reconstructed by TC itself. Therefore the tracks reconstructed by DCH is used in precise time reconstruction in TC. In this section, the time reconstruction in TC will be focused on. The overall positron time reconstruction will be discussed Chap. 8.
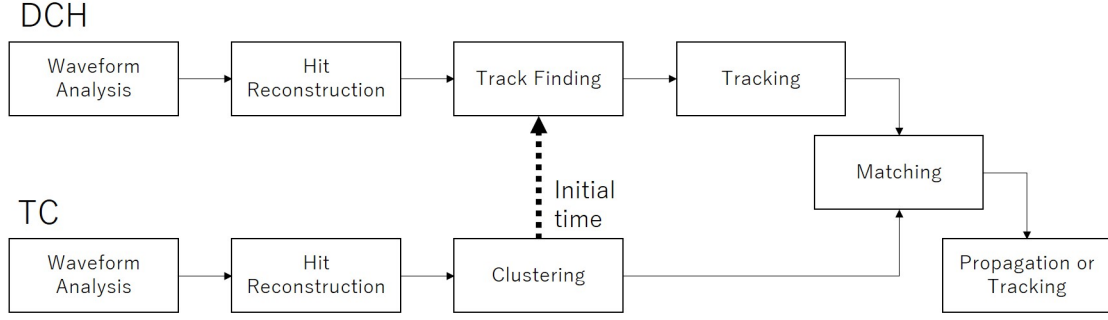
Figure 5.1: Overview of positron reconstruction chain.

5.2.1 Waveform Analysis

In the MEG II experiment, the raw waveform (Fig. 5.2) data of the detector signals are taken so that we can directly analyze them to extract the signal time, charge, amplitude and so on. At the beginning, peaks are searched for by setting a threshold. To avoid double counting a pulse, only one maximum peak is found in a fixed local region of 10 ns. To obtain the baseline of the waveform, at first, the amplitude at every sampling point is put in a histogram and then the average around its mode is calculated as the baseline. It is a stable way to get baseline against pile up and spike noise. The bin size of the histogram and the region for the average from the mode is optimized to give the best time resolution. The signal amplitude is defined as the difference between the found peak and the calculated baseline. The signal charge is obtained by integrating the pulse for a fixed region, 20 ns. To obtain the time, a digital constant fraction method is used. We define the signal time as the time at a fixed ratio to the signal amplitude. The optimal ratio depends on the signal shape and noise situation. Therefore, we optimized that in each test. Typically it is 20-30%. Depending on the noise situation, a moving average low pass filter is applied.
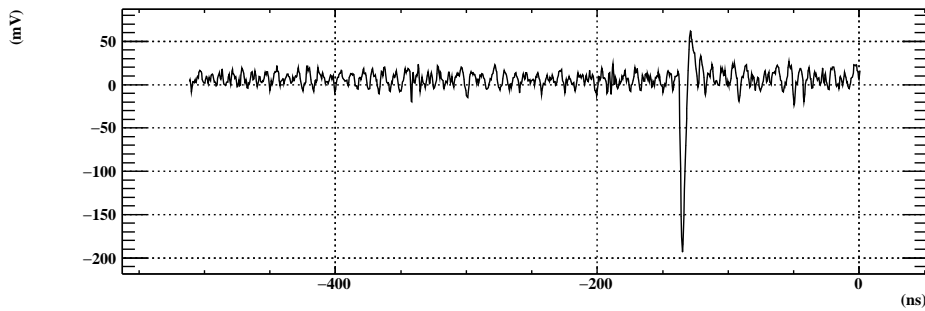

Figure 5.2: Typical waveform from single counter.

5.2.2 Hit Reconstruction

A hit time and position in each counter are reconstructed based on the results from the waveform analysis in the two channels. Matching of signals in the first and second

channels is based on the signal time. If signal times in the two channels are in 4 ns, they are regarded as a signal from the same hit. The hit time is defined as the average time of the two channel times, that is,

$$T = \frac{(t_{ch1} + t_{ch2})}{2} \tag{5.2}$$

where t_{ch1} and t_{ch2} are the reconstructed times in the first channel and the second channel respectively. The hit position is also reconstructed from the times of the two channels. The effective velocity of light, v_{eff}, in our counter is obtained formerly by position scanning with a ^{90}Sr source as explained in the next chapter in detail. Using it the hit position can be obtained as

$$x = \frac{v_{eff}(t_{ch1} - t_{ch2})}{2} \tag{5.3}$$

We also tried to use the pulse charges to reconstruct the hit position, but the position resolution is worse than that of the former way because of a short attenuation length (8 cm) of the scintillator.

5.2.3   Clustering

Since a signal positron leaves several hits on TC and in parallel pile up positrons may often hit TC, we should distinguish which hits belong to which positron. Moreover even one positron is able to make a tail event when its second turn is small and hits on the same counter hit in the first turn or its close counter, which is called double turn hits.

Two methods have been developed to make clusters of the same positron hits. One is so-called local clustering: this algorithm simply checks a hit in geometrically next counter from a counter having a fastest hit time, and make a chain to the next counters if a hit in the next counter is found. Fig. 5.3 describes typical hit patterns. If one finds a hit, these three patterns are all to be checked. In this process, a timing cut which rejects the hits far from the first hit more than 1 ns is also applied. In contrast, the other method constructs clusters globally. As the fastest hit is a seed, this algorithm uses the correlation between counter positions and time in the counters. We defined *geometrical order* which is the order for a positron to hit as shown in the left figure in Fig. 5.4. The right of Fig. 5.4 shows the correlation between the geometrical order and the time. By fitting it with a liner function, we obtained the slope. With the slope every hit time is projected as shown in Fig. 5.5 for an example. Peaks are searched for from the projected histogram, and become cluster seeds. A cluster consists of the hits in 1 ns from the seed time.
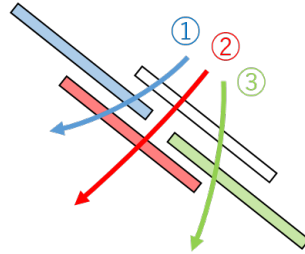

Figure 5.3: Schematic of three possible hit patterns.

We adopted the global clustering for the final analysis for the TC because it succeeded in removing tail events as shown in Fig. 5.6 and 5.7 which is obtained with the data obtained in a pilot run of TC described in Chap 7 in detail. The global clustering improves
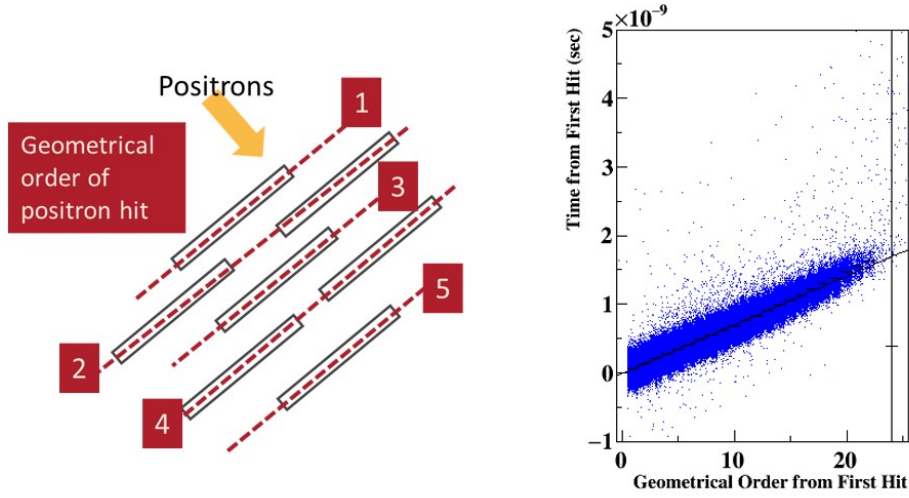
Figure 5.4: Drawing of the counter geometry and hit order (left) and the correlation between the order and time (right).

the time resolution as shown in Fig. 5.6 by reducing the tail events as described in Fig. 5.7 for an example.

5.3 Calibration

5.3.1 Timing Calibration

In the $\mu \to e\gamma$ search, $T_{e\gamma}$ is reconstructed and time coincident events are searched for. Therefore the coincident window should be known in advance. This global time offset between the positron spectrometer and the LXe photon detector can be calibrated by using the radiative decay of muon, $\mu^+ \to e^+ \nu_e \bar{\nu}_\mu \gamma$ (see Tab. 3.1). The decay emits a photon and a positron simultaneously, and thus the peak from the decay in the $T_{e\gamma}$ window enables us to calibrate the global time easily.

On the other hand, it is also important to calibrate relative time offsets inter counters in TC. We use the following two methods. One is track-based calibration. In the MEG II experiment we have abundant calibration source of positrons from Michel decay. Subtracting known path length by simulation or reconstructed track by DCH, the relative time offset can be extracted. In addition, there is an advantage that even during the data taking we can check the time offsets. The other method is laser calibration in which laser light is injected into the counters simultaneously. The relative time offsets can be obtained by using the counter signal generated from the laser light. Short DAQ time for the laser system ($\sim$30 minutes) without a need for beam is an advantage of the laser calibration. Since the track-based calibration need ~ 2 days for obtaining enough data, the laser calibration is useful to monitor time dependence. These two methods are independent of each other.
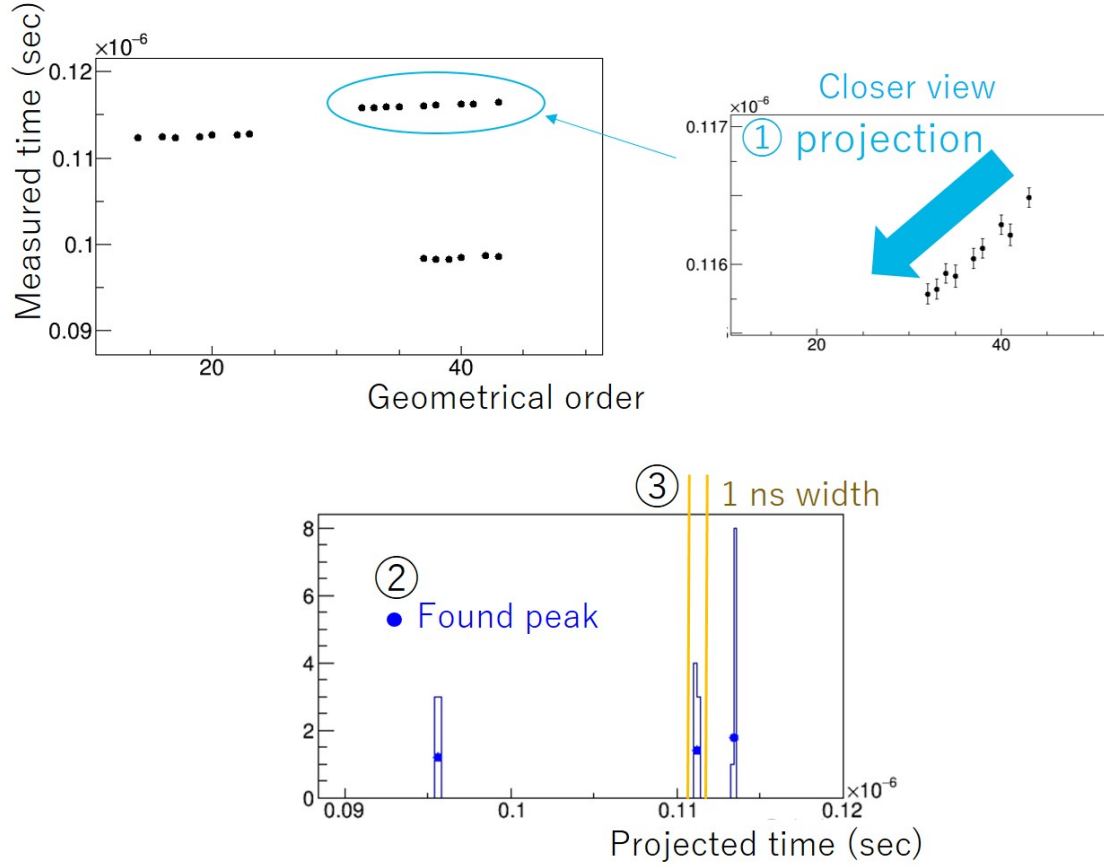
Figure 5.5: Explanation of the clustering with an example event. Correlation between geometrical order and measured time (top) and projected time distribution in the event. (1) The measured times are projected, (2) peaks are found in the projected time distribution as seeds, and then (3) clusters are made within 1 ns width from the seeds.

Track-based Calibration

The relative time offsets are obtained to minimize χ^2 as,

$$\chi^2 = \Sigma_i^{N_{\text{event}}} \Sigma_{j=1}^{N_{\text{hit}}} \left(\frac{T_{ij}^{\text{meas.}} - T_{ij}^{\text{expec.}}}{\sigma} \right)^2 \tag{5.4}$$

$$T_{ij}^{\text{expec.}} = T_{i1}^{\text{meas.}} + TOF_{ij} + \Delta T_j \tag{5.5}$$

where $T_{ij}^{\text{meas.}}$ is the measured time on the jth hit counter in the ith event, TOF_{ij} is time of flight from the first hit counter to jth counter, and ΔT_j is the intrinsic counter time offset which are the target to be known in the calibration. To calculate this, Millepede II [33] is used. It calculates the linear least squared with the local parameters that is event-by-event parameters such as trajectories and the global parameters such as the counter time offsets simultaneously. The key of the track-based calibration is to estimate time of flight (TOF) between counters which is basically given by DCH.
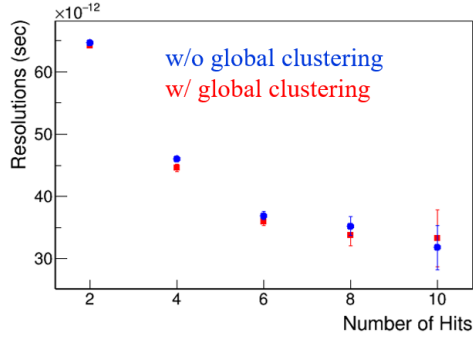
Figure 5.6: Resolutions dependence on number of hits with and without global clustering
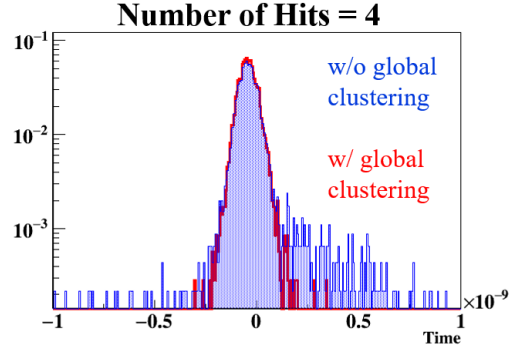

Figure 5.7: Time distribution with 4 hits with and without global clustering

Laser Calibration

The detailed set up is already showed in Sec. 4.7. The time offsets are obtained relative time to the time from laser synchronized pulser.

5.3.2   Position Calibration

The hit position is reconstructed by the time difference between the two channels as discussed above. The calibration of the two channels time offsets is performed by comparing the simulation and data. Simulated distribution of the hit position is shown in Fig. 5.8.
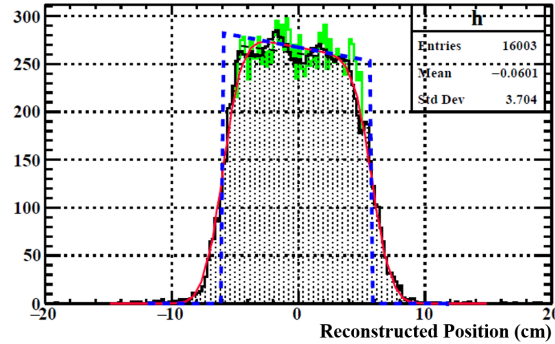

Figure 5.8: The distribution of the hit position on a counter. The green line show the original distribution and the black is after taking moving average. By convolving a trapezoid (blue and red lines) with Gaussian, the distribution of the hit position is fit.

5.3.3   Energy Calibration

The energy deposited into the counter by a positron hit is reconstructed by the pulse charge. In principle, the time resolution of a single counter depends on the energy deposit and including this dependence in the likelihood analysis for the $\mu^+ \to e^+\gamma$ search improves the sensitivity of the experiment. Conversion factors from reconstructed charge to energy

deposit are calibrated so that the distribution of the reconstructed energy deposit fits to that of the MC simulation described in the next section.

5.4 Simulation

The software for MEG II is composed of three parts, named GEM4, MEGBARTENDER, and MEGANALYZER. The first one is for generating events and simulating any interaction in our detectors. The second one takes the two roles of event mixer and waveform simulator. The last one is analysis software for the output data from both of the real experiment and the simulation.

5.4.1 Event Generation and Interaction

Events in the simulation are generated in GEM4 based on Monte Carlo simulation software, GEANT4 [34], written in C++. Muon decays of Michel, radiative, and $\mu^+ \to e^+\gamma$ are prepared in GEM4. We can choose the kinematic of these decays if needed. The event generation also can start from the muon beam not from the decay on the target to simulate the background from the beam. The starting point is -564.70 cm at the z-coordinate which corresponds to just after the last magnet of Triplet II (see Fig. 3.15). This is such that the collimator system is included.

Any interaction in our detectors is also simulated in GEM4. The geometry and materials in the experiment including degrader in BTS are implemented.

Simulation of Positron Track

The positron track and the secondary particles are simulated based on the tracking in GEANT4. Interaction between the injected particle and material in the electromagnetic such as bremsstrahlung, multiple scattering, and photo-electric effect are included. Track momenta and positions at each step are recorded and when a particle goes into a detector sensitive volume step size becomes small to simulate detector response precisely. Once a particle interacts with the volume, the hit information is also recorded.

Simulation of Interaction in TC

When a positron or a secondary particle reaches scintillator part of TC, scintillation photons are generated and they are tracked in the simulation. These processes take into account the known scintillator properties which are amount of light yield, rise time, reflectivity, and attenuation length. If a scintillation photon reaches SiPM region, its time is recorded. This information is used in the waveform simulation explained following sub-section.

5.4.2 Event Mixing

To know the pile up effects, MEGBARTENDER is developed for MEG and MEG II. It makes events mixture of different type of events. For example we can simulate signal events with Michel background events at a certain rate using output files of GEM4.

5.4.3 Waveform Simulation

In MEGBARTENDER, a waveform simulation including pile up is performed using the information from the optical photon tracking in GEM4.

TC Waveform Simulation

Scintillation photons that reach a SiPMs are converted to a waveform signal based on the response of the 6-SiPM-array which can be obtained from single photon data. However the signal from a single photon is too small to measure because of the series connection as explained in Sec. 4.4. Therefore an electronics simulation software SPICE (LTspice® IV [35]) is used. The equivalent circuit to a SiPM pixel is described in Fig. 5.9. First we measured the response of a single SiPM from the single photon data to decide parameters for the electronics simulation. Tab. 5.1 shows the used values in the simulation which reproduce the measured waveform. Using these parameters the single photon output from 6-SiPM-array is simulated by the SPICE. The distribution of the arrival time of the scintillation photons is convoluted with the single photon response. In this way, the waveform from a counter is simulated. At the end white noise and noise originated from SiPMs are added. The noise from SiPMs are also measured and the parameter values are summarized in Tab. 5.2.
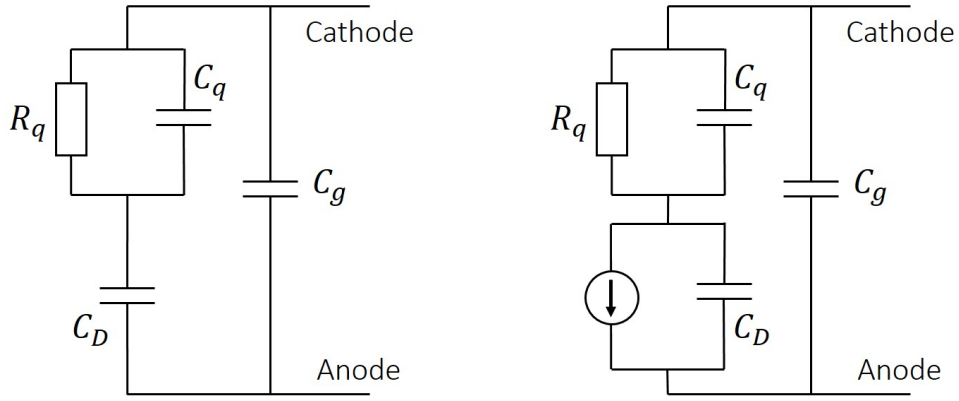

Figure 5.9: Equivalent circuits of pixels in a SiPM which are not fired (left) and fired (right). R_q is quench resistance, and its capacitance, diode capacitance and global stray capacitance are written as C_q, C_D, and C_g, respectively.

Table 5.1: Parameters for waveform simulation in SPICE.

Parameters	
R_q	1150 kΩ
C_q	14.0 fF
C_D	97.0 fF
C_g	141 pF

Table 5.2: Measured parameters for SiPM noise.

Parameters	
Dark Current Rate	1.4 MHz
Recovery Time	185 ns
Cross Talk Probability	8.6 %
After Pulse Probability	31.6 %
After Pulse Time Constant	115 ns
Delayed Cross Talk Probability	22.6 %
Delayed Cross Talk Time Constant	86 ns

Chapter 6

Performance of Multiple Hit Scheme

We performed several beam tests to confirm that multiple hits improve the overall resolution of TC. First, two beam tests in ideal environment were performed by using a beam delivering positrons at a fixed momentum. Secondly, another beam test was performed in high-rate environment to study the pile up effect on the time resolution. In this chapter, we describe these beam tests and the results, which demonstrated the multiple hits scheme. Based on the success of these beam tests, the design of TC such as counter design and readout scheme, was finalized.

6.1 Multiple Hit Scheme in Clean Environment

We had the two beam tests to confirm the multiple hit scheme. In this section we focus on the first test beam in 2013, since the obtained results is similar to that in the second test beam from the multiple hit scheme point of view though the counter design and the electronics are different from those in the final configuration.

6.1.1 Set up

The beam test is carried out at the Beam Test Fasility (BTF) of the INFN Laboratori Nazionali di Frascati in Italy [36]. The beam is monochromatic positron beam at 48 MeV, which is similar to the signal positron energy of 52.8 MeV. There are 1–3 positrons per bunch at 50 Hz. The beam spot is $\sigma_x \sim 15$ mm and $\sigma_y \sim 5$ mm as y is direction from bottom to top, z is the same as the beam axis, and the rest axis is x.

The schematic of the set up is shown in Fig.6.1. Prototype counters are placed on the beam line and in front of the counters one or two time reference counters are also prepared. The scintillator of the prototype counters is $90 \times 40 \times 5$ mm^2 BC418 from Saint-Gabain Crystals wrapped in a reflector of 3 M radiant mirror film. We prepared counters with two types of SiPMs: eight counters with S10943-2547(X) from Hamamatsu Photonics K.K. and six counters with ASD-NUV-SiPM3S-P from AdvanSiD.

One reference counters is composed of $5 \times 5 \times 5$ mm^3 scintillator of BC422 coupled to a Hamamatsu Photonics K.K. SiPM (S10362-33-050C), and the other is $25 \times 12 \times 5$ mm^3 scintillator of EJ232 (BC422 equivalent) with two Hamamatsu photonics SiPM (S10362-33-050C) connected in series on each side. This second reference counter is used only to estimate the time resolution of the other reference counter. On the other hands, the first

reference counter is not used only as a time reference but also as a collimator by triggering by itself.
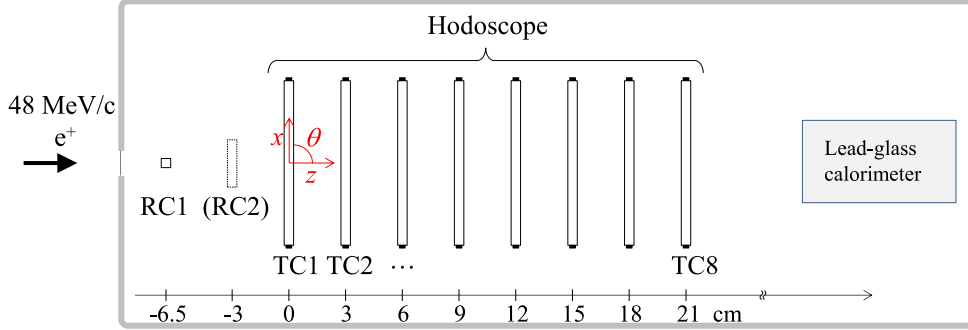

Figure 6.1: Set up in the beam test in Frascati.

The signals are transmitted on a 7-m long coaxial cable (without using the Back Plane) to amplifiers developed by PSI which is the same ones used in mass test as described in Chap. 4.

The transmitted signals are digitized by the DRS4 evaluation board V4 [37, 38] which has 4 channels. The sampling speed is set at 2.5 GSPS. For the prototype counters and the reference counter, we used the six boards. To synchronize among the boards, the sine waves divided by passive splitters are inserted into one channel in each board.

6.1.2   Analysis

Synchronization

Synchronization between DRS boards is important to obtain good time resolution. Originally the time difference among the boards is several hundred ps. In this beam test, we inserted sine wave, fit it and obtained time offset of each board event by event. A higher signal-to-noise ratio allows better quality of the fit. However, since the dynamic range of DRS is tuned to the counter signal, which is from -0.05 to 0.95 V, only positive side of sine amplitude is used for synchronization analysis, while negative side is saturated as shown in Fig. 6.2. Each DRS board is synchronized by the maximum point obtained by fitting.
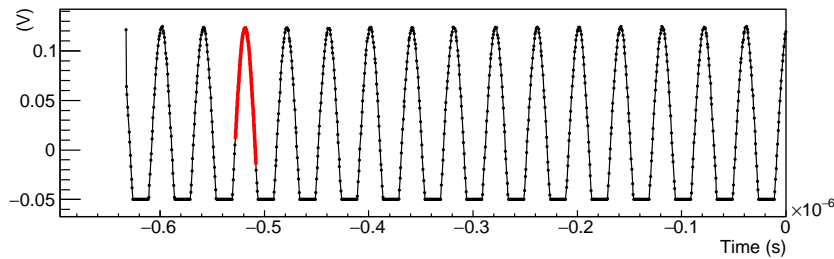

Figure 6.2: Inserted sine wave for the synchronization. Since the dynamic range is limited, we fit only positive part of the sine amplitude. Red line is the fit sine.

Event Reconstruction

The reconstruction of single counter hit is the same as the final way as described in Chap. 5. A hit time is reconstructed by taking average on two channels in a counter. To eliminate the pile up hits, clusters are made, so that each hit time in a cluster is into 1 ns. Fig. 6.3 shows an event which has two pile up positrons as an example and they are successfully separated by the clustering.
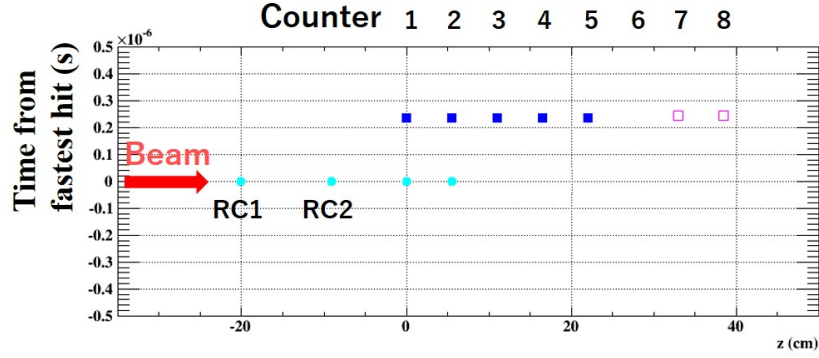

Figure 6.3: An example of a pile up event. Cyan markers show the hits from triggered positron which hits to the reference counters. On the other hand, blue and magenta markers describe hits from pile up positrons. Using reconstructed time, we can separate these pile up events.

Tracking by using reconstructed hits is also applied after clustering. The tracking is based on Kalman Filter [39] assuming straight positron trajectory as an initial state. Far hits from reconstructed trajectory are removed.

6.1.3 Event Selection

Multi-positron events are removed by energy deposit cut for former two counters as shown in Fig. 6.4. .
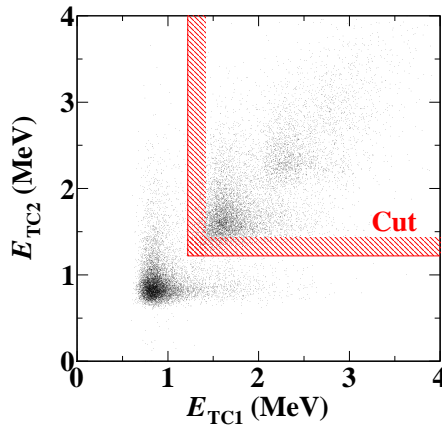
Figure 6.4: Distribution of energy deposit on first counter and second counter.

Estimation of Time Resolution

Simply the overall time with n hits can be obtained as,

$$\frac{\sum_i^n T_i}{n}, \tag{6.1}$$

where T_i is time of ith counter.

Estimating the overall resolution of prototype counters, we performed two analysis methods. One is reference counter analysis in which resolution is estimated by σ of

$$\frac{\sum_i^n T_i}{n} - T_{RC1}, \tag{6.2}$$

where T_{RC1} is the reference counter time. At the end, the resolution of reference counters, which is estimated to be 30.3 ps, should be subtracted .

The other analysis is even-odd analysis which takes the difference between average time of even counters and odd counters, that is,

$$\frac{\sum_j^{n/2} T_{2j}}{n/2} - \frac{\sum_j^{n/2} T_{2j+1}}{n/2}, \tag{6.3}$$

The σ of this time distribution is the same as that of Eq. 6.1 if there is no correlation between each T_i. This analysis is independent with reference counter analysis.

6.1.4 Resolution Improvement with Multiple Hits

The overall timing resolutions of the counter arrays as a function of number of hits are shown in Fig. 6.1.4. The result is fit by a function of $\sqrt{\frac{\sigma_{singleall}^2}{N} + \sigma_{const}^2}$. In principle of multiple hit scheme, the σ_{const} is zero. With the reference independent analysis it is zero, which means multiple scheme works well. On the other hand, the result by analysis with reference counter, the best fitted function has constant term of 8.0 ps in Hamamatsu counters. However it is negligibly small and we demonstrated the resolution improvement with increasing number of hit counters.
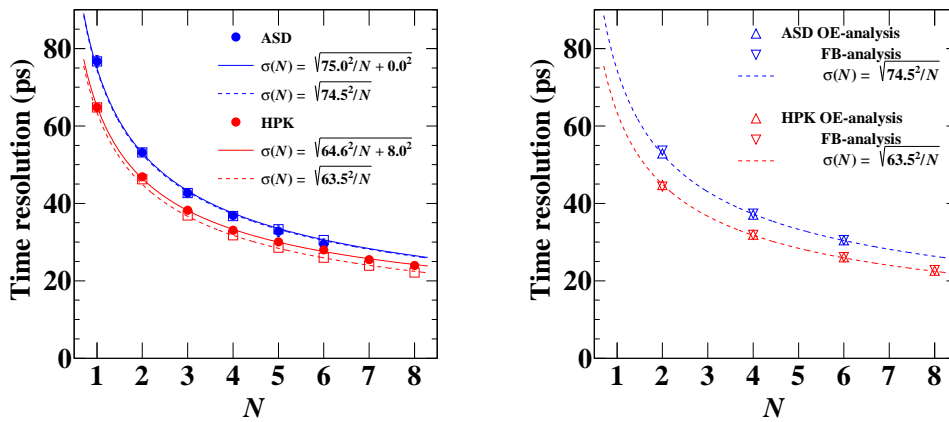

Figure 6.5: Overall resolution vs. number of hits (N) obtained by analysis with reference counter (left), and even-odd analysis (right).

6.2   Rate Dependence

In MEG II environment TC will have positron backgrounds at 50–170 kHz. To estimate the effect, we performed a beam test at piE5 beam line in 2014.

6.2.1   Set up

Overview of the beam test are described in Fig. 6.6 and Fig. 6.7.
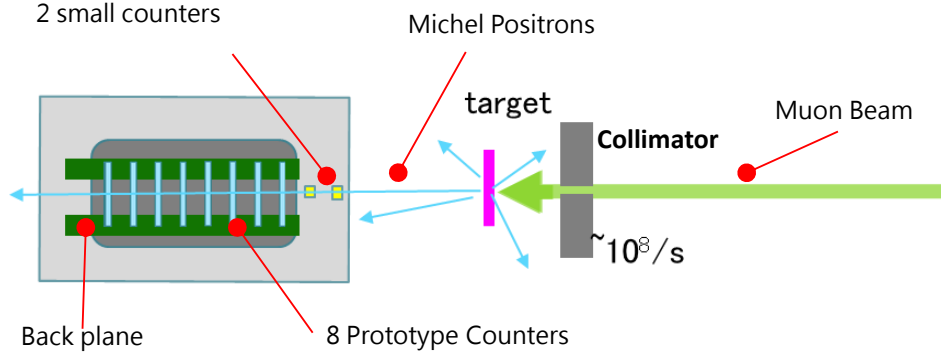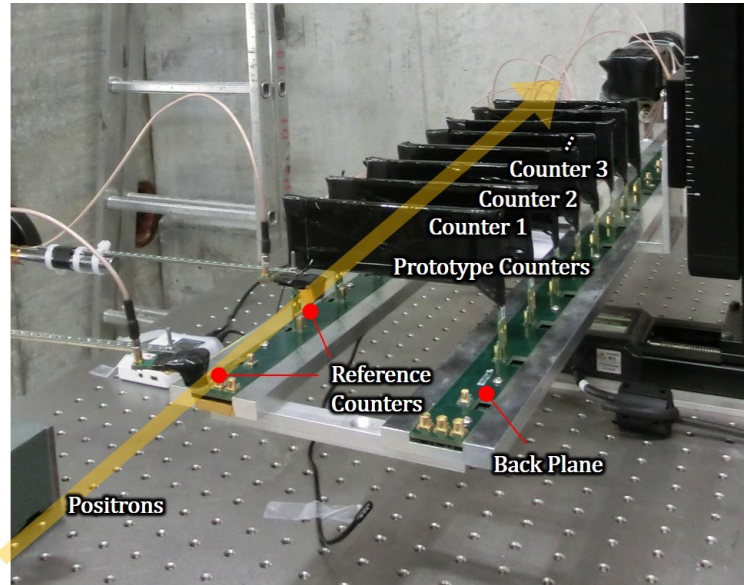

Figure 6.6: Set up of the high rate test in PSI

Figure 6.7: Picture of set up in beam test for checking rate dependence in PSI

The test beam is performed in front of the MEG II experimental area where is out of the COBRA magnet. The muon beam line is the same as described in Sec. 3.2. The muon rate is $\sim 10^8$ Hz. After a collimator the Michel positrons are generated on a target. Therefore, we obtained a time uniform Michel positron background. We placed two

reference counters each of which consists of $5 \times 5 \times 5$ mm^3 plastic scintillator (Saint-Gobain BC422) attached by 1 SiPM (HAMAMATSU S10362-33-050C, 3×3 mm^2, 50 μm-pitch) with Teflon wrapping in front of the prototype counters. Using them for coincidence trigger we selected straight positron events. The distance between the two counters is 3 cm. They also give us the reference time in time analysis explained later on.

Eight prototype counters are placed 8.5 cm behind the latter reference counter. These are put at an interval of 5.5 cm. Scintillator is EJ232 from ELJEN which is not the final one (BC422) but have the same characteristics: the attenuation length is 8 cm and the rise time is 0.35 ns. The size of the first six counters is $120 \times 40 \times 5$ mm^3 and that of the last two counters is $120 \times 50 \times 5$ mm^3. The six SiPMs (AdvanSiD NUV type) connected in series on the final version of PCB are attached to the scintillator at the both ends. The configuration of the prototype counters are almost the same as the final version. However the scintillator and SiPMs have a bad performance due to quality control issues of vendors and the single counter resolution of these prototype counters are ∼90 ps in pre-test with ^{90}Sr source evaluated in the same way as described in Sec. 4.5.1.

Counters connected to Back Plane which is also prototype for the final detector. The signals from counters are read by 7 DRS evaluation boards with 1.6 GSPS. A DRS evaluation board has 4 channels and sine wave is inserted to one channel in each board for offline synchronization among boards. We also recorded the RF signal from the cyclotron to eliminate positron contamination originated in the beam.

6.2.2 DAQ

We took data at three different hit rates, 18–64 kHz, 53–166 kHz, and 89–290 kHz by changing a slit in the beam line. The rates in latter counters become lower due to the smaller solid angle. Furthermore low momentum positrons can be scattered largely on the former counters and then they does not hit on latter counters. The detailed hit rates in each counter are shown in Fig. 6.8. These values are estimated by random trigger data. No-signal events are counted and converted to hit rate by Poisson distribution. (The expected hit rate in MEG II from an MC study is 20–100 kHz depending on z.) The trigger rate was 55 Hz.

The waveforms of a reference counter and a prototype counter are shown in 6.9 as an example. We found that the prototype Back Plane picked up noise and made resolution bad.
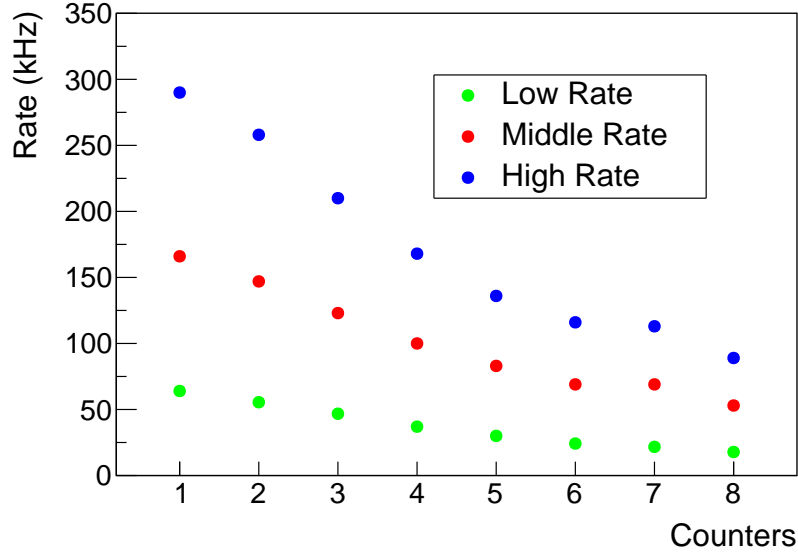
Figure 6.8: Hit rate in each counter in each configuration. Since the height of counter 7 and 8 is larger than the others, their rates are relatively high.
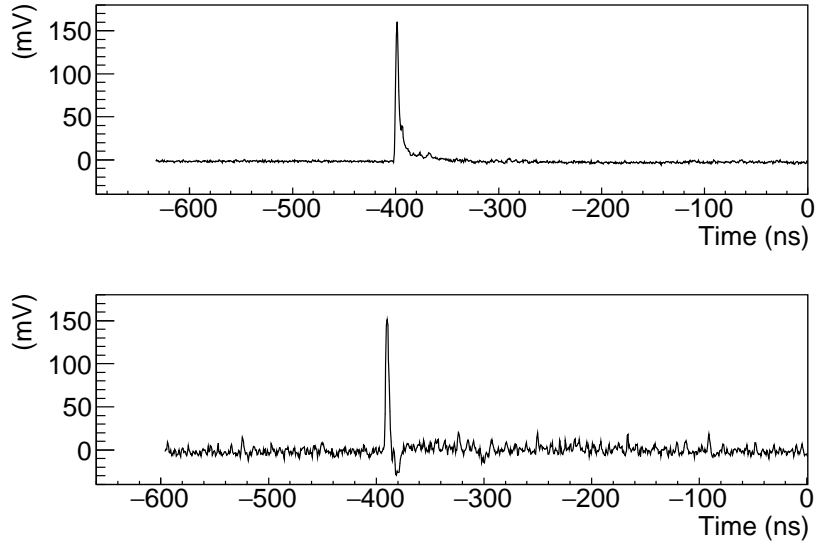

Figure 6.9: Waveform of a reference counter (top) and a prototype counter (bottom)

6.2.3   Analysis

Event reconstruction and synchronization is the same as the Frascati test beam as described in Sec. 6.1.2, but reference time is calculated by the two counters as $\frac{T_{RC1}+T_{RC2}}{2}$. The resolution of the reference time is estimated to be 32 ps as shown in Fig. 6.10. Since reference counters are small enough and far enough from each other, the resolutions do not change in the different hit rate environments. Thus, the single counter resolution is estimated with the two reference counters in the same way as Sec. 6.1.2.
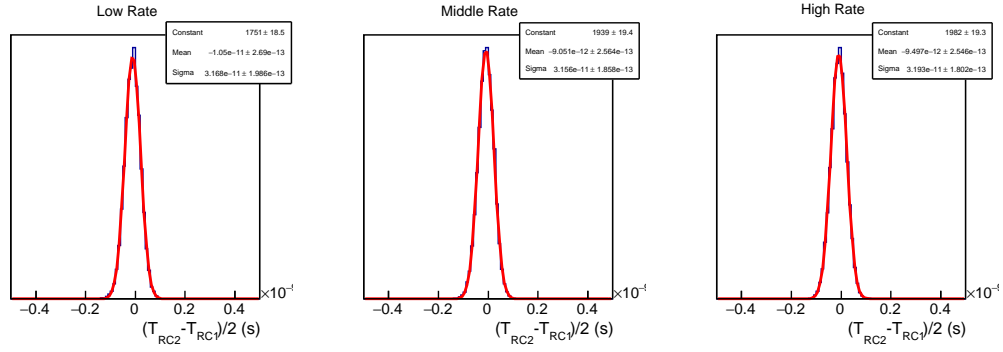
Figure 6.10: Time difference between two reference counters.

Event Selection

We took average on times of the two reference counters as reference time. The muon beam had positron contamination, and we could recognize it by looking the time distribution between the reference time and RF time as shown in Fig. 6.11. The positron from beam itself makes a peak, while the positron generated in the target from muon beam distributes uniform. The red colored region in the figure is used.
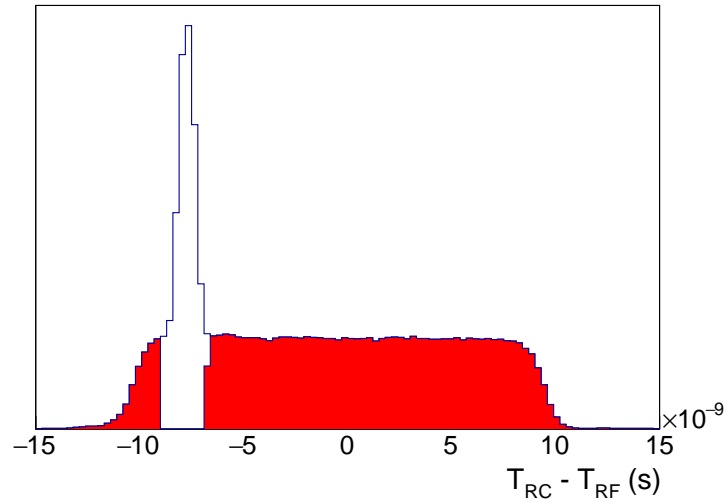

Figure 6.11: Time difference between the reference counter and the RF signal. A peak comes from the positron contamination in the beam and red colored region is selected for analysis.

To select straight positron events a strict cut for charge of the reference counters is also applied. Fig. 6.12 is the distribution of the charge and the region filled with red is selected. The peak values are different between the two reference counters by a factor of 0.62, and these red region in the two distributions are the same range after correction.

In addition, the events which have enough energy deposit in all the counters are used for following analysis to select good straight events. The amplitude distributions in each channel are shown in Fig. 6.13. The hits having more than 0.04 V signal are used in the
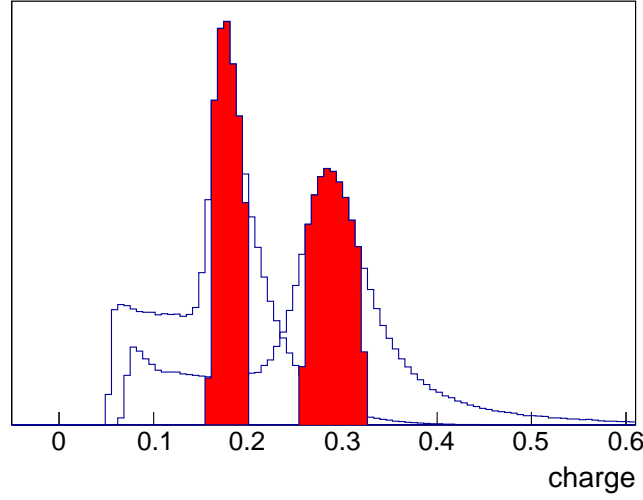
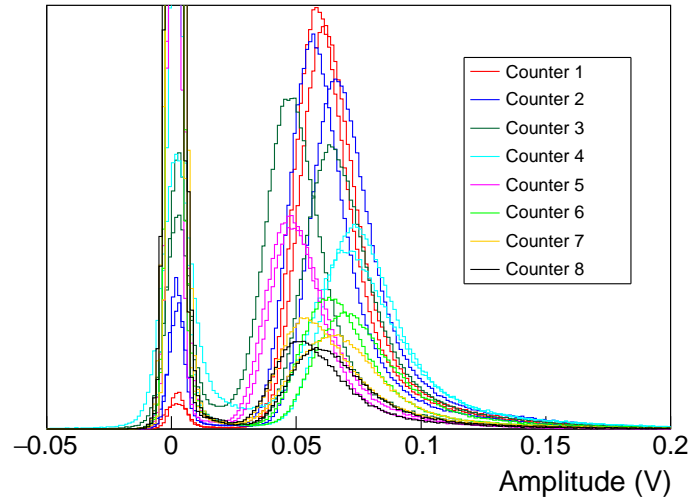Figure 6.12: Charge of reference counters. Red region is selected for analysis.

figure.

Figure 6.13: Amplitude of each channel of all the counters. We set the threshold at 0.04 V.

6.2.4   Electronics Jitter

The electronics jitter is estimated by inserting pulses from a pulser into different channels by dividing passively. The pulser is NIM Pocket Pulser MODEL 417 from PHILLIPS SCI-ENTIFIC whose pulse width is 6 ns and repetition rate is at 10 kHz. The synchronization effect is also included in the result. The jitter between reference counters and prototype counters should be subtracted to evaluate the overall TC performance. On the other hand, the jitter intra prototype counters should be taken into account. Tab. 6.1 shows

the measured jitter for estimating single counter resolutions. They are obtained from the time distribution of $(T_{ch1} + T_{ch2})/2 - (T_{RC1} + T_{RC2})/2$ for jitter from the reference, and $T_{ch1} - T_{ch2}$ for the jitter intra prototype counter.

Table 6.1: Electronics jitter (ps)

Counter	1	2	3	4	5	6	7	8
b/w RC and prototype counter	21.9	19.3	22.1	22.3	18.8	21.8	19.7	26.3
intra prototype counters	7.3	13.1	6.2	7.8	13.2	6.8	7.1	6.7

6.2.5   Time Resolutions

Single Counter

The single counter resolutions are estimated by the reference counter analysis. The time distribution of each counter is shown in Fig. 6.14. Fig. 6.15 shows the result from the beam test and precedence tests with ^{90}Sr source. Since energy deposit in the beam test and ^{90}Sr source test is different, the resolutions from the ^{90}Sr test are corrected by scaling the resolutions with the square root of the ratio of the energy deposit difference expected by MC. In the figure the resolutions of the latter three counters are consistent with those in the ^{90}Sr test but the other resolutions are worse than those in the ^{90}Sr test. Since the former counters have higher hit rates as discussed above, their resolution become worse.
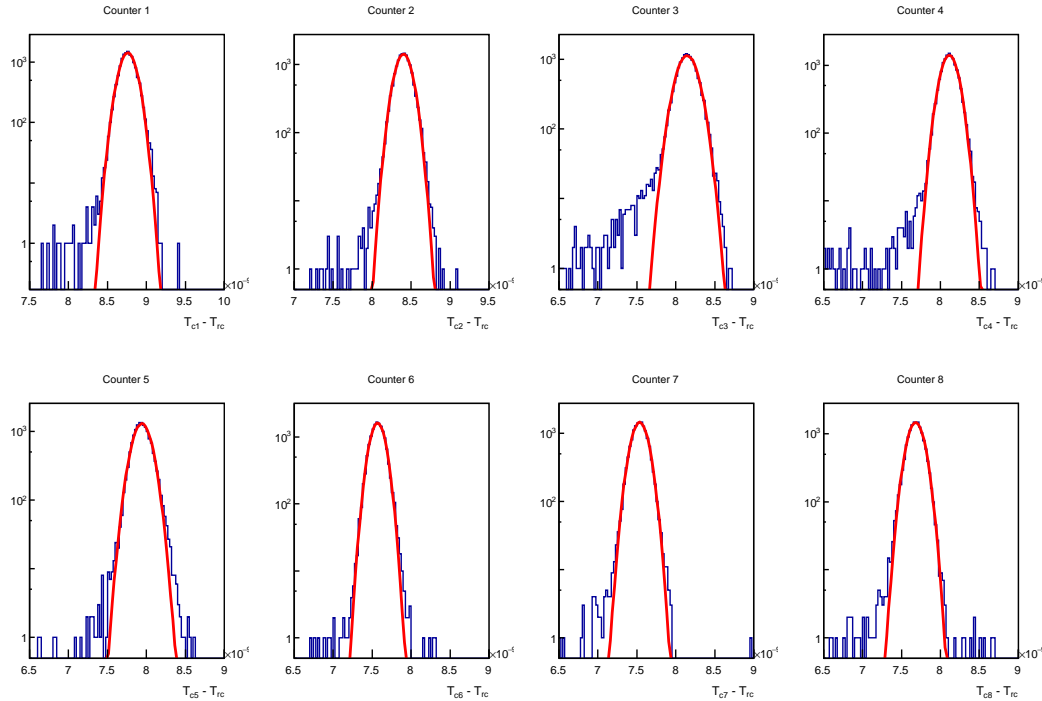

Figure 6.14: The time distribution of each counter.

Fig. 6.16 shows the resolution dependence on the hit rate in each counter. Though the resolution degradation at higher rate is observed, it is negligible and the different between
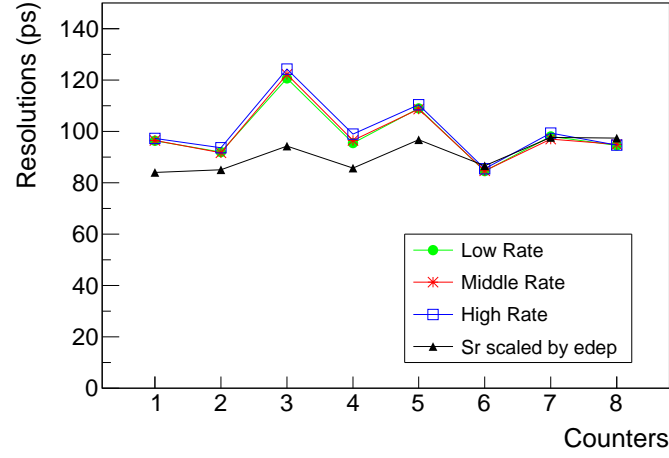
Figure 6.15: The single counter resolutions with ^{90}Sr test results which are scaled by energy deposit.
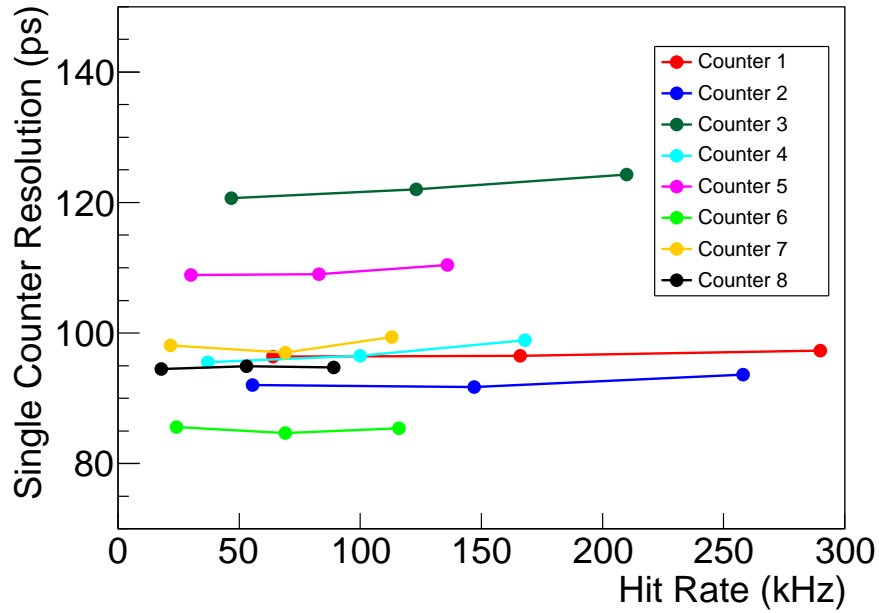
the counters are much larger than that.

Figure 6.16: The single counter resolution as a function of hit rate in each counter.

Noise

The distribution of noise RMS in each counter is shown in Fig. 6.17 and it indicates some of channels have larger noise than that in the others. By fitting with Landau function convoluted with Gaussian the peaks of noise RMS are obtained as described in Fig. 6.18. Noise of Counter 3 and Counter 4 is slightly larger than that of the other counters, and we

identified that the noise is picked up by back plane by swapping several channels. After the beam test, we decided to add layers of electronic shielding to each signal line in the back plane and thus we did not observe channel-dependent-noise from the back plane.
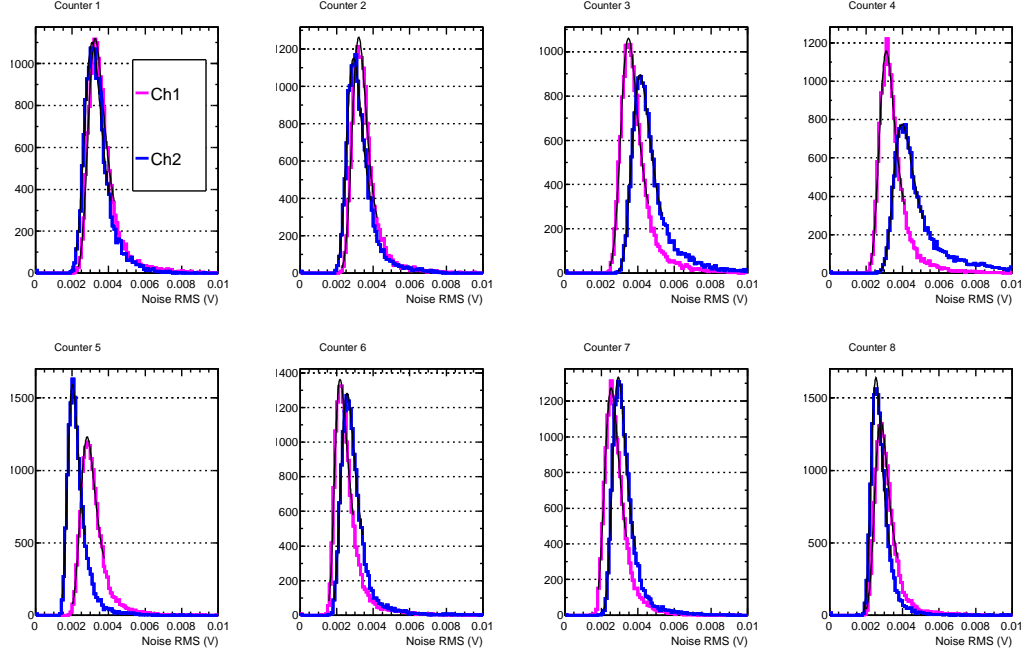
Figure 6.17: Distribution of Noise RMS in each counter. Their peaks are obtained by fitting with Landau convoluted with Gaussian which is drown in black line. Even in the same counter, the noise situation of the two channels is not the same.
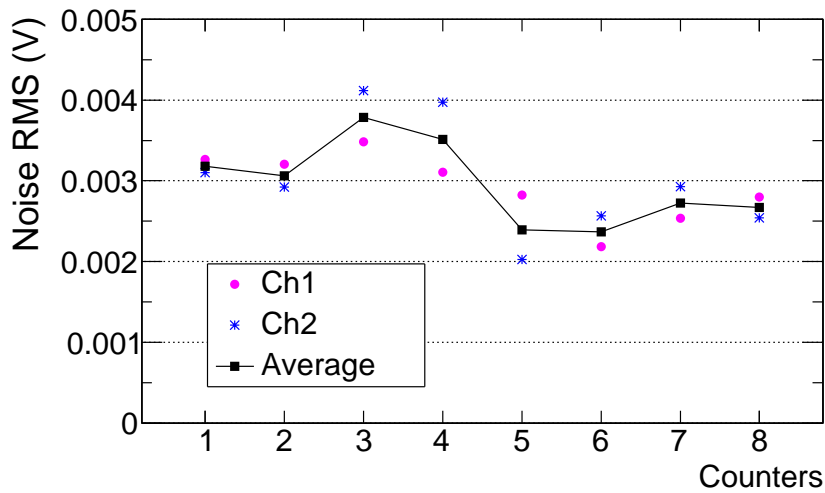
Figure 6.18: Noise RMS obtained from Fig. 6.17.

Fig. 6.15 also indicates hit rate dependence of the single counter resolution. In the

high rate environment, a small degradation of the resolutions can be seen because tails of signal from pile up positrons make noise situation worse as shown in Fig. 6.19. Higher noise is observed in the high rate environment, while they are almost same in middle and low rate environment. It is consistent with tendency of the rate dependence of single counter resolutions.
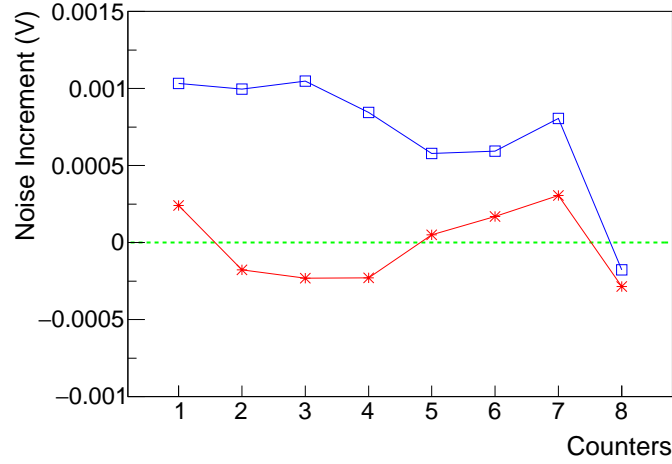

Figure 6.19: Noise increase in each counter in middle rate (Red) and high rate (Blue) from low rate environment (Green).

Clear correlation between noise and resolution degradation is observed in Fig. 6.20. The variation of single counter characteristics is largest effect on its resolution as indicated in Fig. 6.15. However the resolution degradation in high rate environment can be seen after subtracting the variation obtained by ^{90}Sr test.
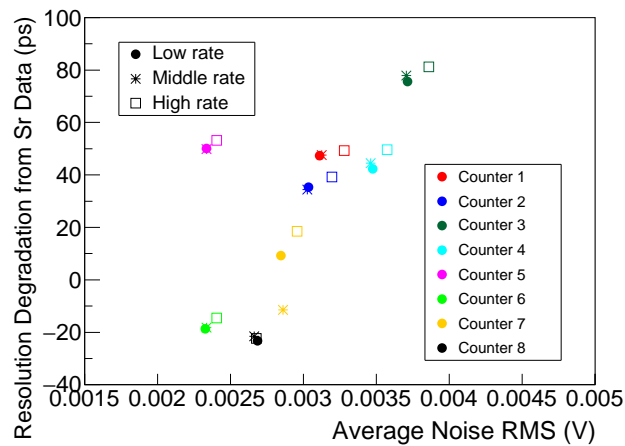

Figure 6.20: The correlation between noise and degradation of single counter resolution from ^{90}Sr source test.

6.2.6 Multi-Counter Resolutions

The overall resolution as a function of the number of hits are estimated as described in the analysis section. Overall resolutions obtained by two analysis and expectation from single counter resolution is shown in Fig. 6.21. The resolutions are consistent with expectations. The total effects of the high rate environment can be seen in Fig. 6.22. At the high rate the small deteriorate of time resolution is observed. We consider two reasons: pile up positron make noise situation worse as discussed above; and pile up makes tail of time distribution measured by several counters. For the TC this deterioration is not crucial. Moreover in the MEG II experiment the expected positron rate is less than 100 kHz and in middle environment is similar situation to MEG II. In conclusion, we demonstrated that excellent timing resolution with multiple hits can be obtained in the MEG II experiment.
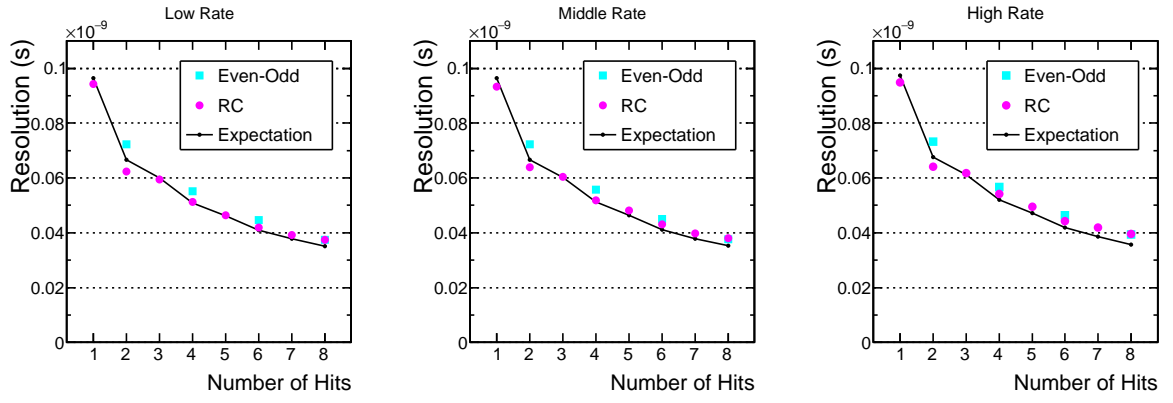

Figure 6.21: Overall resolution comparison among two analysis results and expectation.
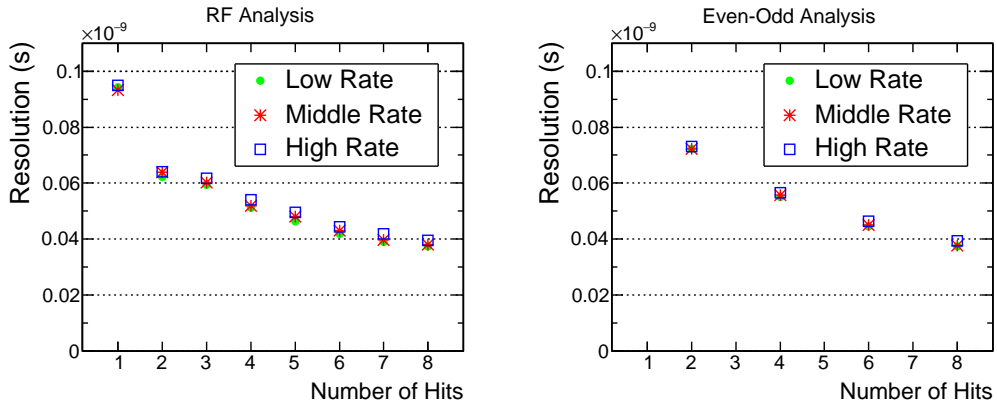

Figure 6.22: Overall resolution in each rate with RF analysis (left) and Even-Odd analysis (right).

Chapter 7

Timing Counter Performance

The final detector was constructed and installed as described in Chap. 4. We performed three pilot runs from 2015 to 2017 at the MEG II beam line. Moreover in 2017 laser test runs with the final DAQ system was also performed. This chapter will discuss the overall TC performance obtained by these runs.

7.1 Pilot Runs

We had three pilot runs in 2015, 2016, and 2017, and the run for the test of laser system and final DAQ in summer 2017 before the final pilot run in November and December 2017. The main differences includes the number of the counters and the fibers, the DAQ electronics, and the beam set up as summarized in Tab. 7.1. Only half of the downstream (DS) counters (128) was installed and tested in 2015 and 2016. The counter configurations in 2015 and 2016 are the same, but the number of the laser system was increased in 2016. From 2016 to 2017 all counters were dismounted and assembled again. During this re-assembly period, we installed the full laser system, and added the thermal links on all the counters and the additional optical cement for the counters to be mechanically strong. The counter assignment in 2017 was totally changed in the re-assembly. In particular, all counters used in 2015 and 2016, which were installed to DS, were assigned to US . The detailed set up will be described following each subsection.

Table 7.1: Summary of difference among runs for TC.

Year	2015	2016	2017 Laser	2017
Number of Counters	128	128	256	512
Number of Fibers	8	40	216	432 (Full)
Number of DAQ channels	256	256	512	512 (Half of all)

Counter assignment and the definition of position identification is described in Fig. 7.1. In 2015 and 2016, we installed and tested counters from the row of 5 to 12.

7.1.1 Pilot Run 2015

The first pilot run with the 1/4 counters was performed in December 2015. Beam set up was the same as MEG II one whose muon rate is 7×10^7 on the target. Because of a delay of the DAQ system meaningful data taking was only for 10 hours. This is not enough to
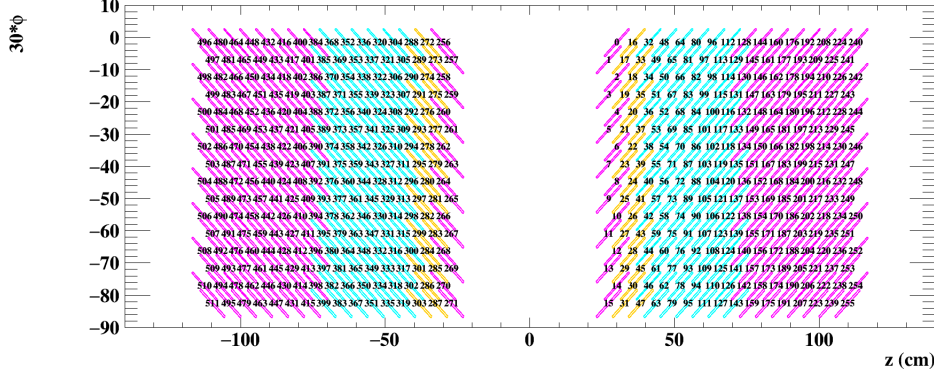
Figure 7.1: Counter assignment and position IDs. Counters colored cyan are 5cm-height-counters, and the others are 4cm-height-counters. In them, outer ($|z| > 70$ cm) counters colored magenta are attached straight SiPM arrays, and inner is L-shape ones, and yellow colored ones are mix counter in which one SiPM array is L-shape and the other is the straight. Positions are counted along ϕ decreasing starting most inner DS counters.

estimate overall timing resolution with several counter hits. Moreover data quality is not good such like large noise, poor dynamic range, and lack of online synchronization.

However it is the first installation of TC, and test of several triggers for TC is performed in this pilot run. We prepared four types for TC. Three of them is for positron data taking as single counter trigger, multi-counter trigger, and track-like trigger. Single counter trigger is the coincident trigger of two channels for a counter with certain threshold for the signal amplitude. We can trigger OR for all the single counters or for only specific counters. Multi-counter trigger is based on the single counter trigger, and namely threshold for number of hits in certain time window can be applied for triggering. Moreover, to take into account geometrical order of hit counter, track-like trigger is implemented. In addition, pedestal trigger was also implemented. Every triggers can be mixed each other with scaling as needed.

7.1.2 Pilot Run 2016

Since the beam time was not enough in 2015 due to the DAQ debugging, the second pilot run was performed. We modified several problems of the DAQ system written above, and moreover the increased number of fibers for laser calibration as shown in Fig 7.2.

7.1.3 Laser test with the final DAQ

Before the pilot run 2017, the laser system in DS got ready to test except for the switching device. Therefore we operated it without any beam to check its stability.

7.1.4 Pilot Run 2017

We mainly use the data in 2017 to estimate TC performance. Here detailed set up of the pilot run will described.
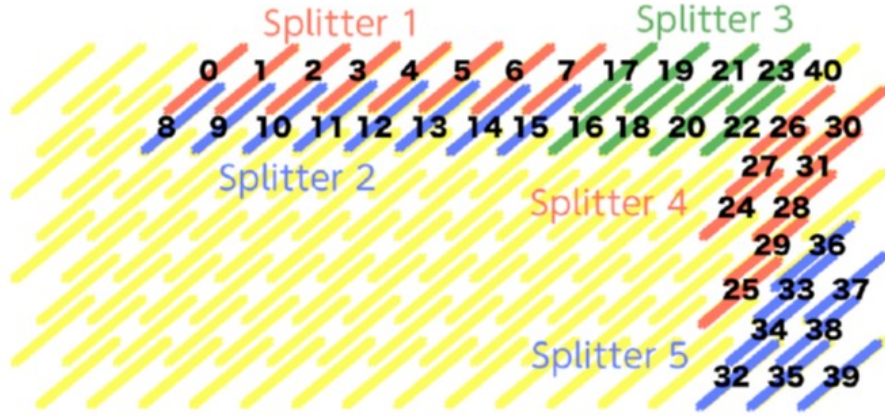
Figure 7.2: Configuration of the counters with laser fiber in 2016

Beam and Target

The overview of the beam line was already described in Sec. 3.2. Since the spallation target, SINQ, was removed, the proton current was set to ~1500 μA or ~1380 μA which is lower than planned value of 2200 μA in the MEG II experiment. To recover the lower muon yield due to the lower proton current, the muon beam rate at the center of COBRA magnet was tuned to be 30 % higher than the nominal MEG II value (~8.1×10^7 μ^+/s at 2200 μA). The absolute stopping rates were ~6.1×10^7 μ^+/s at 1500 μA and ~5.6×10^7 μ^+/s at 1380 μA respectively with the assumption of 85 % stopping efficiency on the target which is estimated by MC study. They were still 13 % and 20 % lower rate than the expected stopping rate in MEG II, ~7×10^7 μ^+/s.

The beam center is -2.1 mm along X direction, and -12.2 mm along Y direction spreading 11.3 mm and 11.2 mm (σ) respectively. These beam parameters are measured by a 5 mm Raster scan of ~270 point measurements. Fig. 7.3 shows the result of the Raster scan. We use a scintillator target in the run. Thickness of the targets is not uniform.
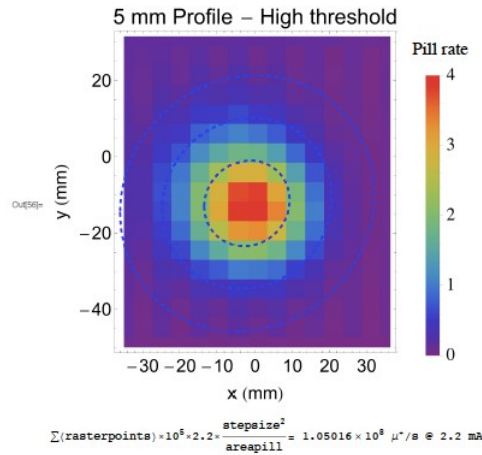

Figure 7.3: The result of Ratter scan of beam.

DCH Mock up

A mechanical mock up DCH is installed. Its outer frame made from 2-mm thick carbon fiber and inner frame made of 20 μm thick Mylar film is installed. One sector of the anode wires and related electronics are mounted. To operate and test gas system of DCH, aluminum spacers fill the remaining empty sectors. Therefore end-cap material is not the same as the final DCH, while the chamber gas is the same.

DAQ Electronics

We use the final electronics, WaveDREAM. Since mass production of all channels is still under way, data taking of upstream and downstream are separately performed by re-cabling. Some connectors of WaveDREAM are fragile and their ground line are unstable. It made noisy channels or dead channels not applied bias voltage correctly. It is soldering problem and will be fixed. The sampling speed is 2 GSPS. The gain of the amplifier in WaveDREAM is set 100 for the normal SiPM counter and 50 for the high gain SiPM counters.

One crate has 16 slots each of which has 16 channels placed on 2 chips. Two channels in a counter are connected to the same chip. Defining Z inner channel as a first channel, every channels connected to WaveDREAM in order of position ID. In summary, every two slots correspond to outputs from counters in the same column.

Synchronization

For synchronization between chips, a main clock signal is supplied to each WaveDREAM board. Then a PLL chip control the synchronization of the two chips. Though the PLL synchronization accuracy is abour 10 ps, the online synchronization is limited by intrinsic jitter from DRS4 to around 60 ps. Therefore a sine wave generated from the PLL output is inputed to DRS4 to synchronize between every chips in offline analysis.

Trigger

The single counter trigger is used. It requires one or more counter hits as explained above
.

Counter Operation

Though we lost a few signal or observed the deterioration of the time resolution in some counters due the fragile connector of some of WaveDREAM channels, from the counter view points all counter except for one counter worked properly, which is confirmed by swapping the noisy or dead channels for a normal channel. One channel of the broken counter was a short circuit and the current was saturated when the bias voltage was applied. Therefore we turned off the channel during the run.

Temperature Control and Monitor

Temperature control was a new system in 2017 run. We use a water cooling system.

Data

We take Michel positron data, $\sim$932 kilo-events for downstream; $\sim$1,333 upstream.

7.1.5 MC

An MC simulation for the pilot run 2017 is prepared. The muon beam is generated from $z = -564.7$ mm, just after the last magnet of Triplet II (see Fig. 3.14), so that BTS contribution and the off-target muon decay are taken into account. Fig. 7.4 shows the decay points of muons in MC. As defining target region $|z| < 15$ cm, the stopping efficiency, which is defined as the ratio of the number of muons decaying on the target to the total muons decaying on the target and in DS, is estimated as 85.7 %. The muon polarization is set 0.9. The triggered event is defined as the event whose Michel positron from the muon beam remains a hit on TC. Background events, which is not required TC hit, are mixed with the triggered event at 7.16×10^7 Hz. In addition, all the frames of the final DCH are also implemented. Notice that the implemented materials are not exactly the same as mock up DCH. In MC final DCH is implemented; there is all wires, and the end-cap material corresponding to the electronics for the wires.
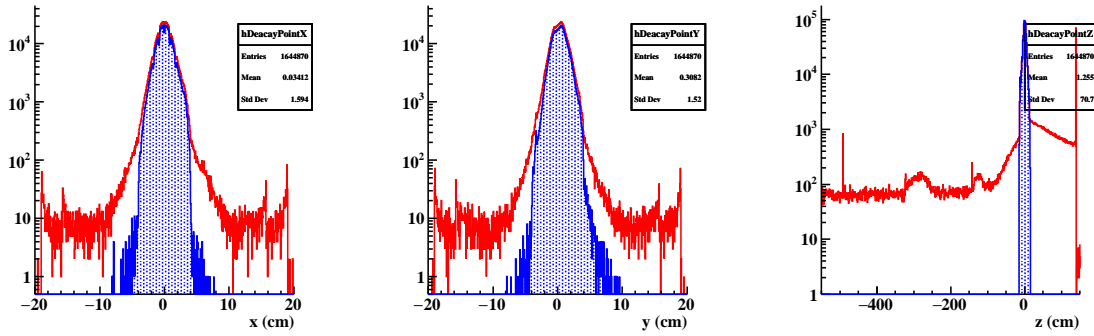
Figure 7.4: Muon decay point in MC. Region colored blue is the vertex of the muon decaying on the target.

7.2 Trigger

7.2.1 Discriminator Threshold

The trigger rates strongly depend on the discriminator threshold as shown in Fig. 7.5. The pedestal trigger is flat at several thresholds. To check the laser trigger we flashed the laser at 10 Hz. It is clear that the rate becomes stable once the threshold crosses the laser signal. On the other hand, with the triggers for the positron signals, the rates gradually go down because of signal amplitude depends on energy deposit. From a result of the laser trigger, we choose the value of 1000 for threshold.

7.2.2 Online Time Resolution

Fig. 7.6 shows the distribution of the online time difference between two adjacent counter. The resolution is ~590 ps, therefore the online time resolution of the single counter divided by $\sqrt{2}$ is estimated to be ~415 ps. The clock speed is 800 MHz, that is the time width of 1.25 ns from which the intrinsic resolution of ~360 ps is expected by dividing by $\sqrt{12}$. The difference between the intrinsic and observed time resolution comes from the electronics jitter on FPGA processing.
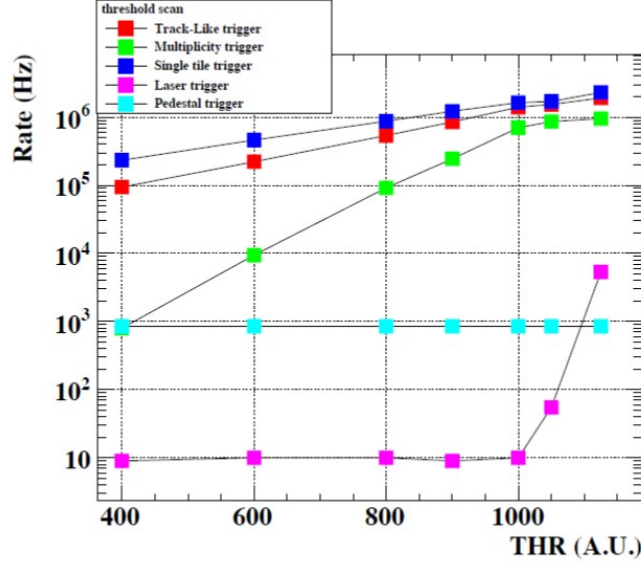
Figure 7.5: Scanning of discriminator threshold. Laser is flushed at 10 Hz. The threshold setting parameter has an offset. Higher value means lower threshold.

This online time resolution reduces the trigger rate in MEG II effectively. Fig. 7.7 shows the online positron time distribution in the MC simulation. Since the positrons hit TC in several times of turns, there are several peaks in the distribution. The sigma of each peak is ∼460 ps and the intervals are 2–3 ns. Taking into account the photon online time resolution (284 ps) estimated by MC, the sigma of each peak is 560–600 ps. Finally the trigger efficiency is obtained as Fig. 7.8 The figure also shows the efficiency in MEG. Since the single channel resolution was ∼2.5 ns in the MEG experiment, the effect of multi-turn is smeared. Therefore the online time resolution itself limited the $t_{e\gamma}$ trigger window for $\mu \to e\gamma$ decay.

In MEG the trigger efficiency was 99 % with 20 ns trigger time window. To achieve the same trigger efficiency in MEG II, the trigger window is 14 ns in MEG II from Fig. 7.8. This reduction of the trigger time window from MEG to MEG II corresponds to the reduction of the trigger rate of a factor 1.5–2.

7.3 Analysis

7.3.1 Optimization of Waveform Analysis

The fraction to the signal amplitude for the constant fraction analysis in the waveform analysis should be optimized in each environment, because optimized value strongly depends on the noise situation. The time resolutions with several fraction are studied by checking the time distribution of adjacent two counters $((T_{i+1} - T_i)/2)$. Fig. 7.9 shows dependence of the average resolution of the two hits on the fraction in the pilot run 2017. The dependence is also checked for specific counters in 2015, 2016, and pre-test with ^{90}Sr source before the installation as shown in Fig. 7.10. Since the noise situation in the experimental site is worse than that in a room for the pre-test, higher fraction should be set. Finally we use the fraction of 20 % for 2017 data, and 35 % for 2015 and 2016 as the optimal fraction.
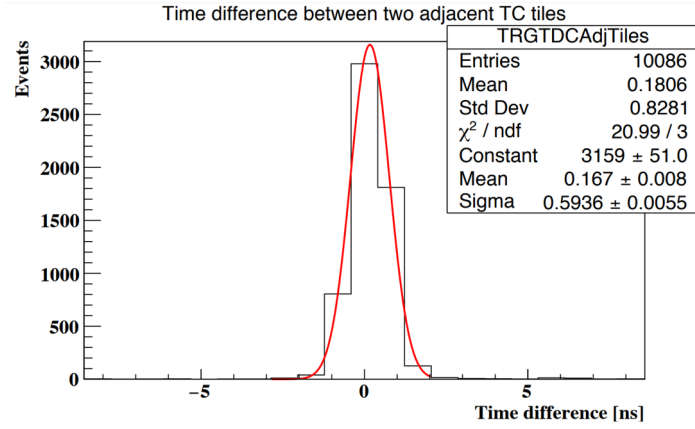
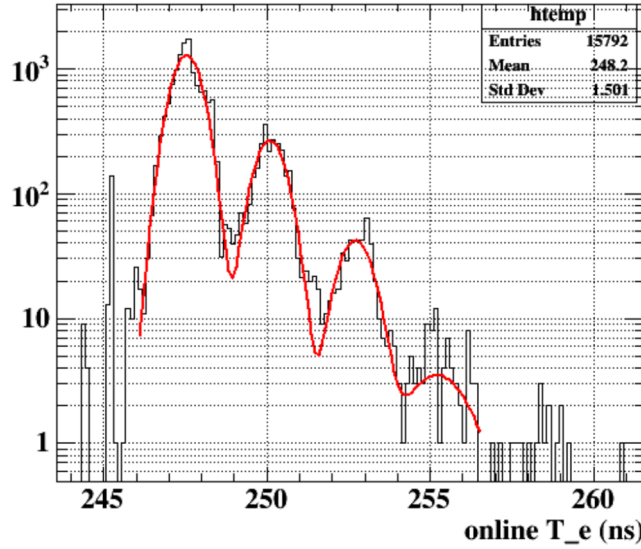Figure 7.6: Online time resolution distribution.

Figure 7.7: Online positron time distribution in MC.

Moreover Fig.7.11 indicates that the optimal fractions depends on counters, especially counters with Type 2 SiPMs (position ID is ∼100), which have larger signal amplitude, requires smaller fraction because of signal and noise ratio is better than the others. On the other hand, if there is a noisy channel, the optimal fraction becomes higher.

7.4   Hit Rate

The hit rate on each counter is calculated by counting pulses measured in an off-trigger window in the single-hit trigger data. The distribution of the reconstructed hit times on DS counters is shown in Fig. 7.12. The peak is from the triggered signal and before them no signal is observed because of trigger bias, that is, triggered signal should be first signal in a certain time window, otherwise the forward signal should be triggered. Thus, only the region after triggered signal can be used for counting random backgrounds. The region from -280 ns to -100 ns is defined as pedestal region. Because of the limitation
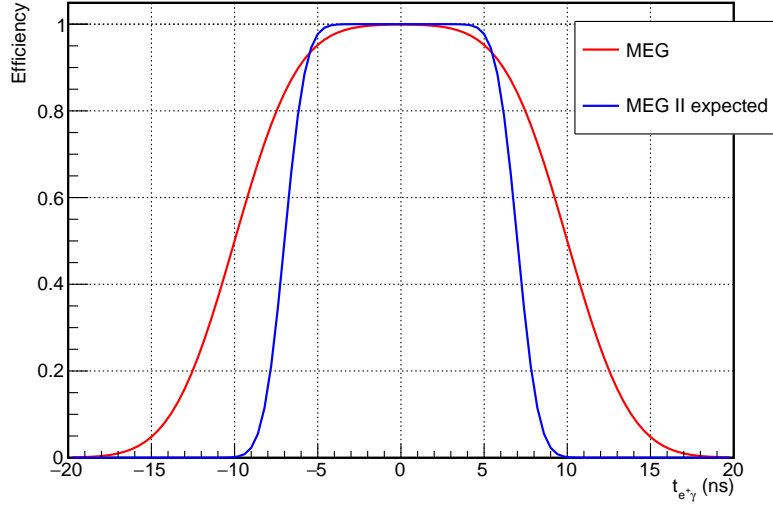
Figure 7.8: $t_{e\gamma}$ trigger selection efficiency.

of signal separation, ratio of no signal events are calculated and translated to the hit rate by assuming Poisson distribution.

The hit rates on every counter are shown in Fig. 7.13 with MC results. Moreover the average hit rate over the same Z position counters is shown in Fig. 7.14. The hit rates are less than 100 kHz. In $|Z| >\sim 100$ cm, hit rates in data is larger than simulated ones because of the mock-up DCH end-cap is not simulated and is expected less material than the final (and MC) DCH. However basically the behavior of the background rate is consistent with MC result, and we did not find any strange background in our experimental environment.

This background rate also indicates that DS has more background than US does. The reason is studied by MC in detail and muon decays in flight remain more background to DS counters. Fig. 7.15 shows the Z position of the muon decays and indicates more muons decay in DS than in US. As a result almost all backgrounds in US come from muons decaying on the target, while backgrounds of 20-60 %, depending on z, in DS are originated from muons decaying off target as shown in Fig. 7.16, and 7.17. Remaining asymmetry between DS and US as shown as blue marker in Fig. 7.17 comes from the polarization of muon.
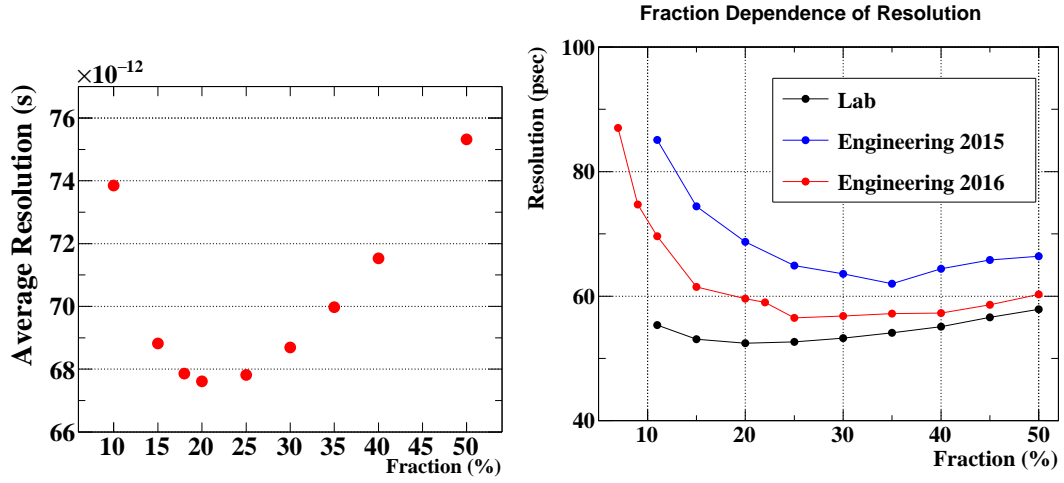
Figure 7.9: Resolutions with several fraction for the waveform analysis in pilot run 2017. The result of all DS counters are averaged.

Figure 7.10: Resolutions with several fraction for the waveform analysis in pilot run 2015, 2016 and pre-test with ^{90}Sr source. Expected resolution decreasing from energy deposit point of view is 5-10 %.
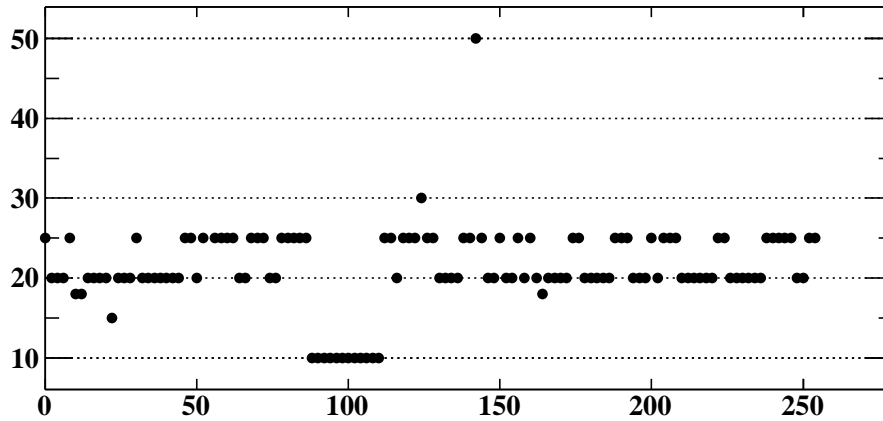

Figure 7.11: Optimized fraction (Y-axis) of each counter combination in fractions of 10-50 %. Numbers of X-axis correspond to position ID of a first counter of the two counter combinations.
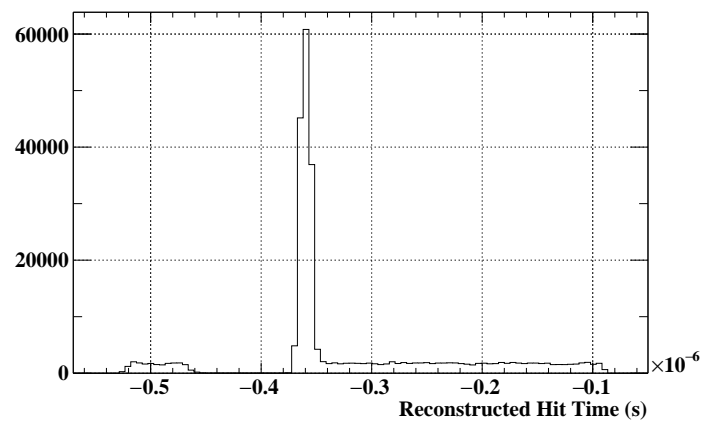
Figure 7.12: Reconstructed hit time in DS counters.
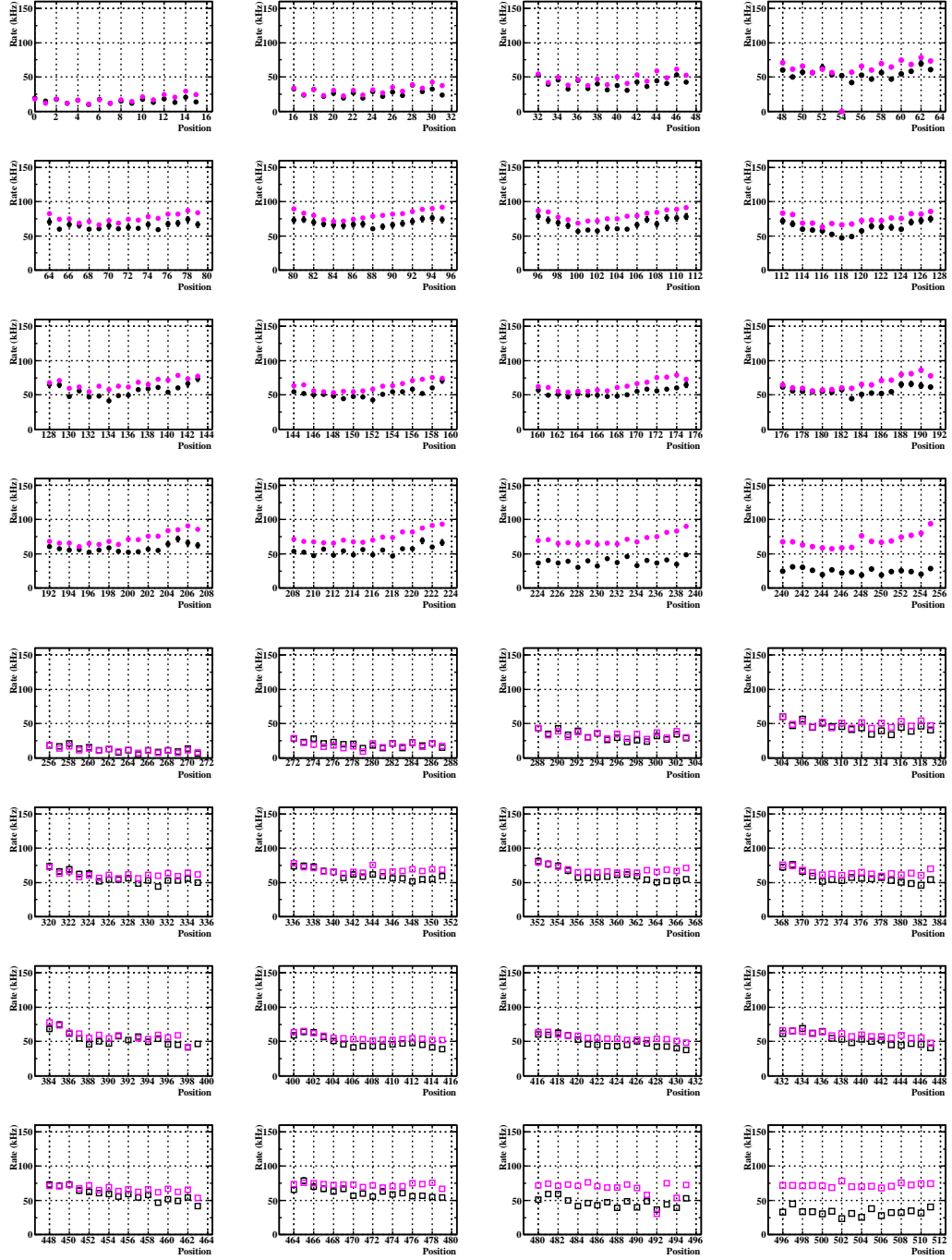
Figure 7.13: Hit rate on every counters calculated with data (Magenta), and MC (Black).
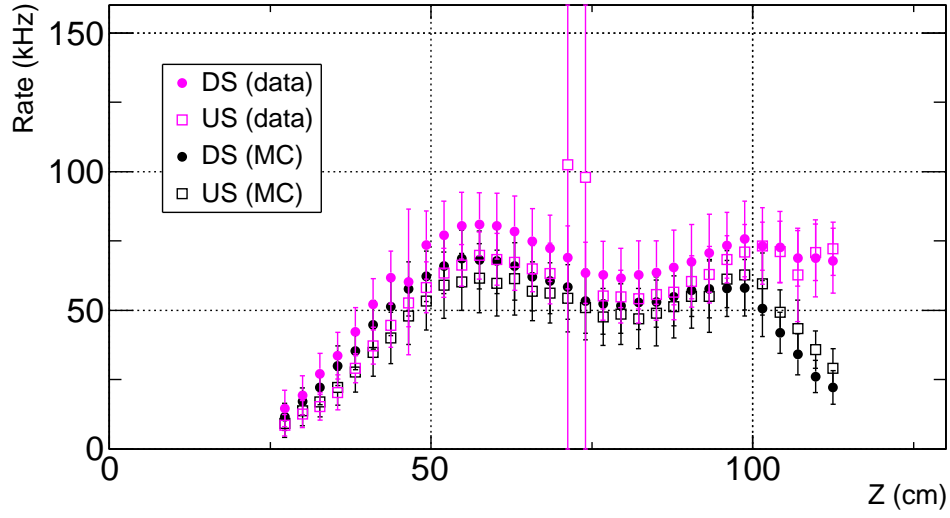
Figure 7.14: Z dependence of hit rate. Large rates on $Z \sim 70$ cm come from counters which DAQ channels are noisy.
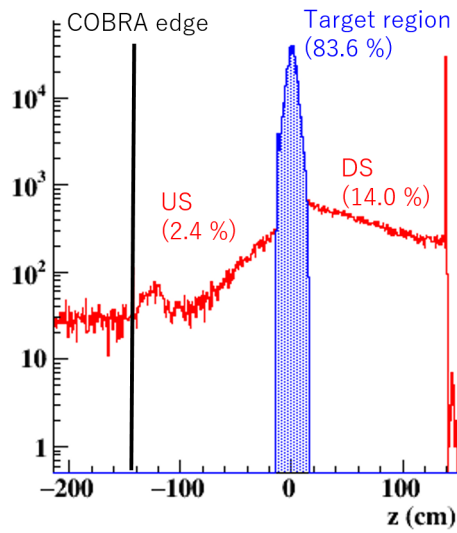
Figure 7.15: Muon decay point (Z) in MC)
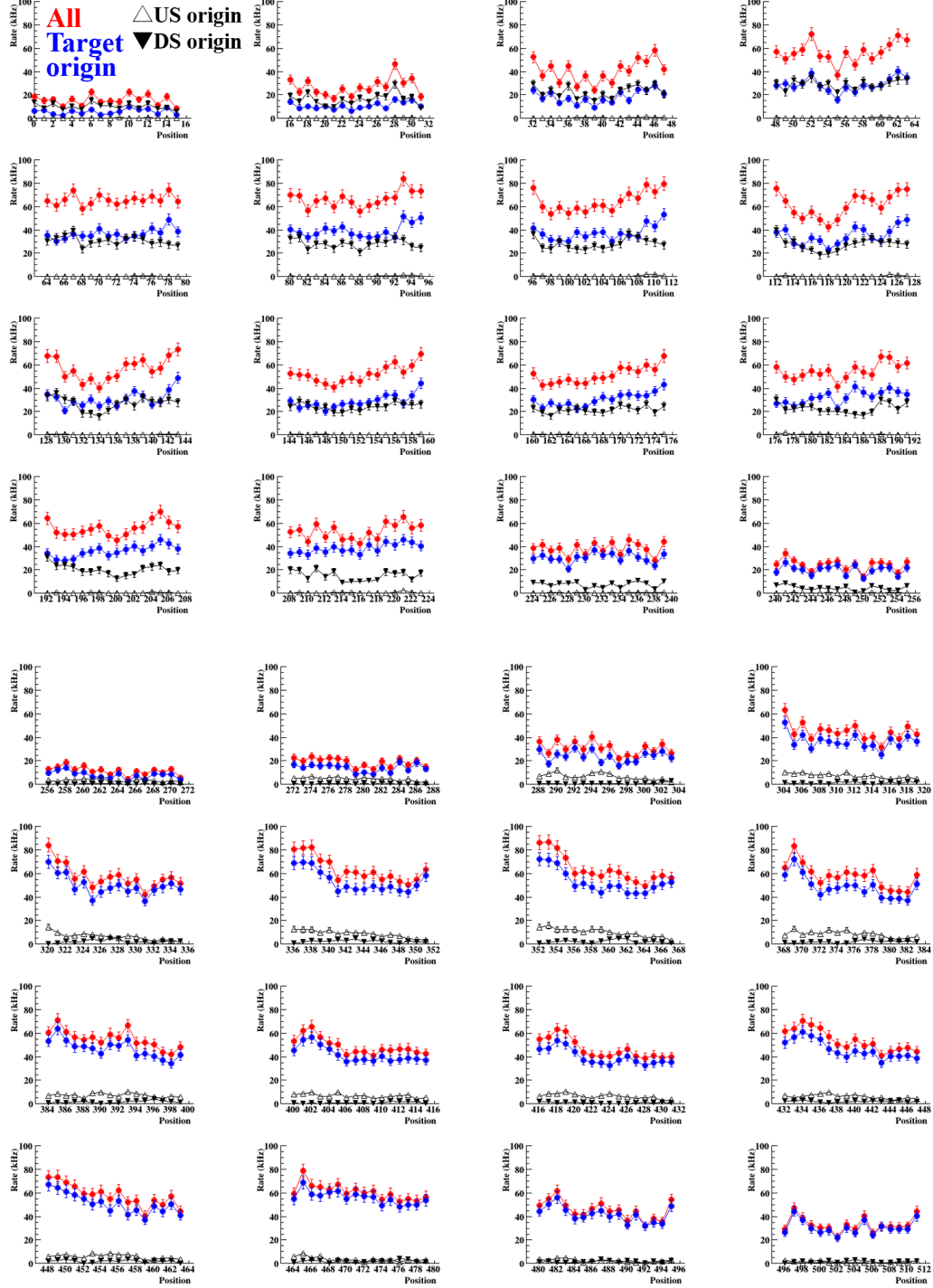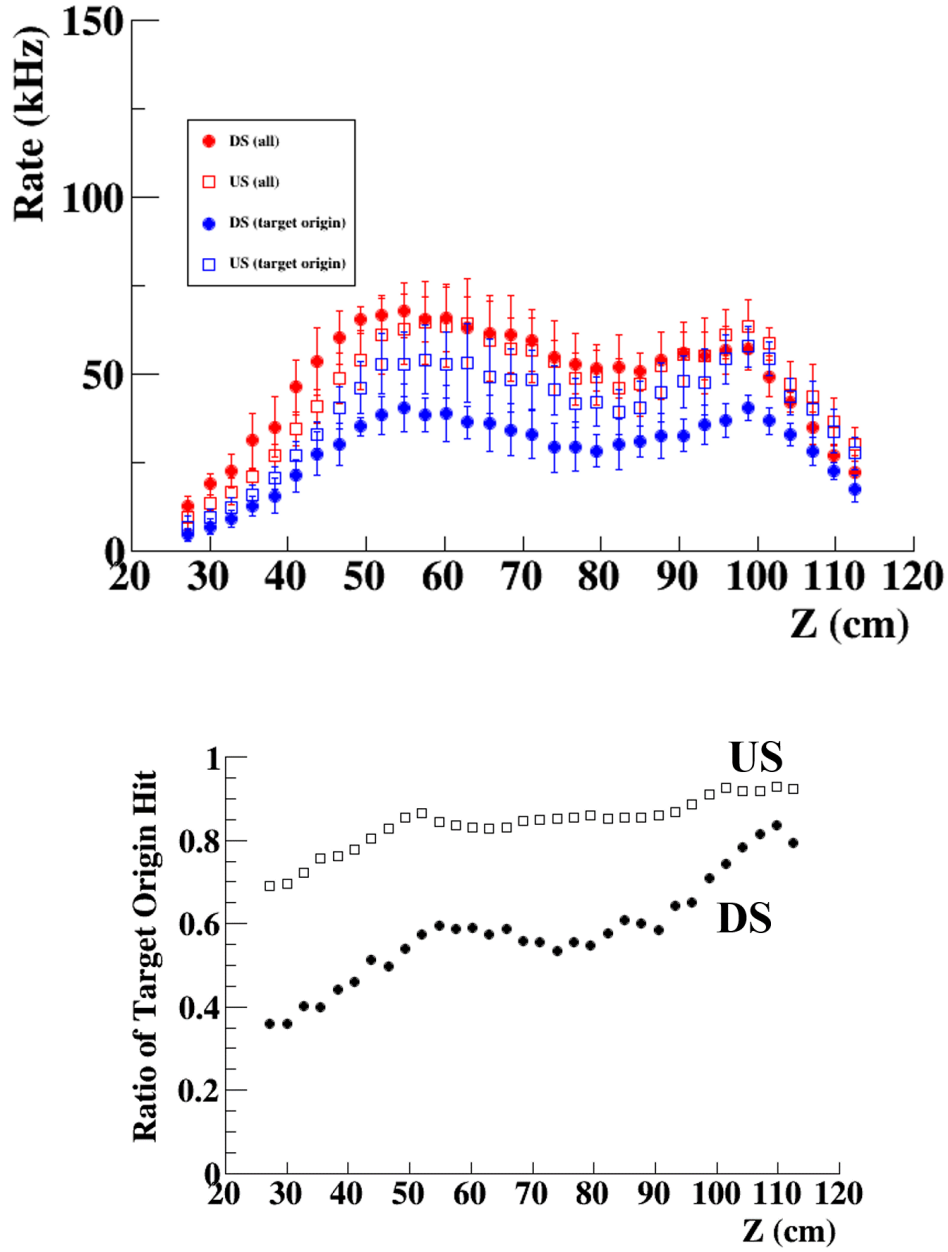
Figure 7.16: Hit rate in MC.

Figure 7.17: Top figure shows Z dependence of hit rate from all background (red), and from on-target muon decay (blue). Bottom figure shows the ratio of them.

7.5 Time Calibration

As explained in the previous chapters, there are two ways for the inter-counter time calibration. In pilot run 2017, we operated the laser system. The measured laser signal times on counters relative to the the laser emission time are stable for about one month as shown in Fig. 7.18, and the average fluctuation in sigma is 2.5 ps. By subtracting the optical length variation for the laser system components such as splitters and fibers from the measured laser signal times, time offsets in signal lines are obtained. The result of the calibration is shown in Fig. 7.19.
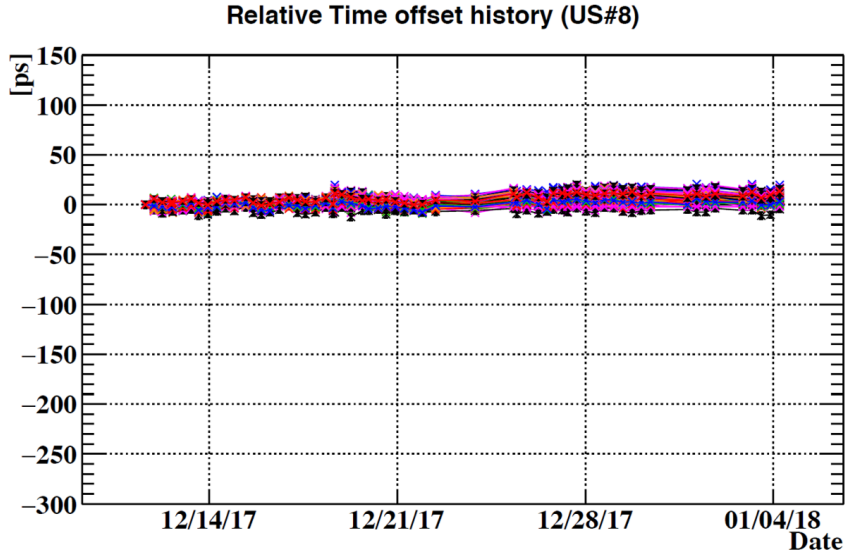
Figure 7.18: History of time offset with one splitter for an example for a month.
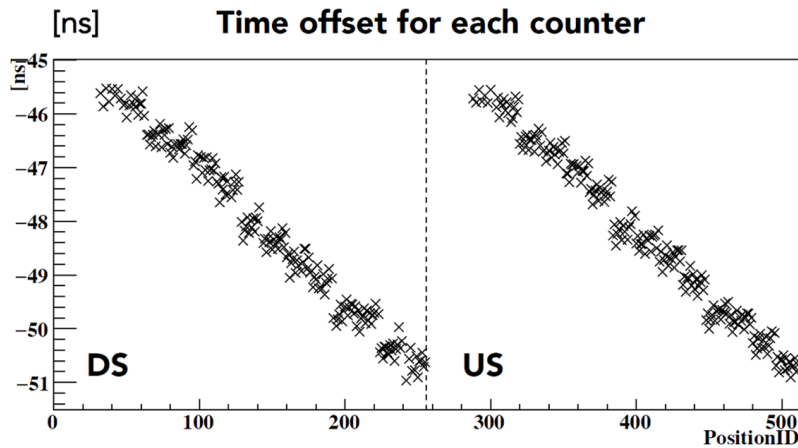

Figure 7.19: Time offset obtained by laser system.

On the other hand, track-based calibration is also tested. Because of absence of track information from DCH, expected time of flight (TOF) for each counter combination in

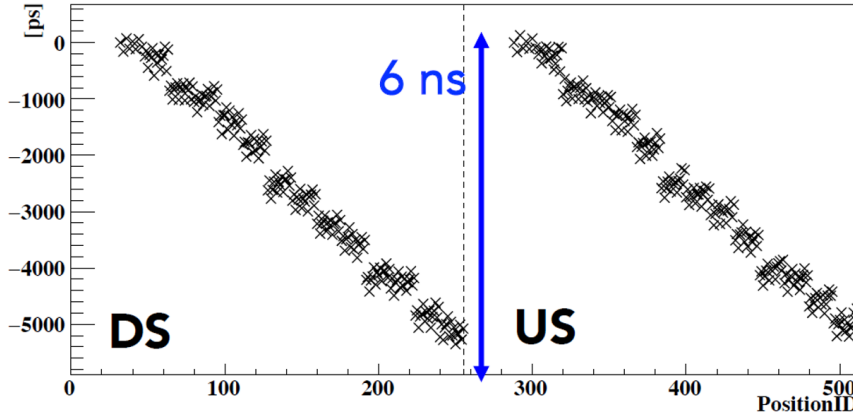MC is used. The obtained time offsets are shown in Fig. 7.20.

Figure 7.20: Time offset obtained by track-based time calibration.

The difference between these two methods is shown in Fig. 7.21. We observed global bias of ~60 ps in the calibrated time along z. The difference between the true TOF and the estimated TOF is expected to make the global bias in the track-based calibration. The time offsets among far counters are never calibrated in one event, that is, the far counters are never fit simultaneously. Therefore, a mis-calibration in a front counters seems to be accumulated to the rear counters. The detailed MC study for the bias is shown in Appendix A. Even if there is the global bias, in MEG II this bias can be corrected by using radiative muon decay (RMD) events. Since RMD emits a photon and a positron simultaneously, it makes peak in the relative time between a photon and a positron as shown in 3.55. Therefore, the time offset bias for the counter position can be observed directly and corrected. The calibration accuracy summed up both of laser and track-based calibration accuracy is estimated to be 61 ps for DS, and 52 ps for US.

7.6   Basic Properties of Counters

At the beginning, the time resolutions of two counters ($\sigma_{(T_i - T_j)/2}$) is discussed for checking the basic property.

7.6.1   Time Resolutions

To obtain time resolutions with two hits, adjacent counters, which position IDs are i and $i+1$ (i is even) or j and $j-15$ (j is odd), are selected. These combinations of two counters are the geometrically same but their channel assignments are different.Fig. 7.22 shows the resolutions of all these combinations. Mean value of the time resolutions are 67.2 ps for the combination in the same chip, and 67.5 ps for that in different chips. Considering fluctuation of the resolution of each counter, the difference from expected resolution from pre-test is also checked as also shown in Fig. 7.22. The differences from the expectation are 36.7 ps in same chip and 38.6 ps in different chips. These difference may come from larger noise situation than that in pre-test. Furthermore comparing between these combinations, an effect of synchronization between different slots can be seen. The difference between same chip combination and different chip configuration is small that means the synchronization system works well.
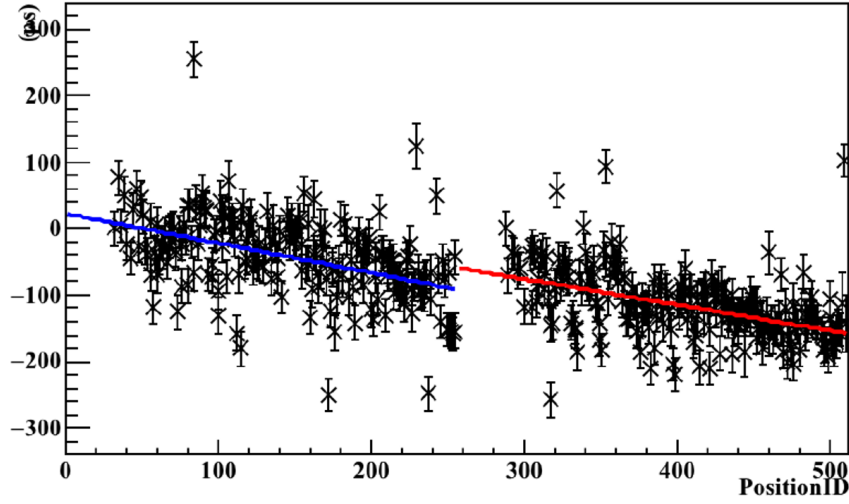
Figure 7.21: Time offset difference between laser system and track-based calibration. Lines are fit results with linear function

In addition, since two type of 4 cm and 5 cm height counters are installed, the resolutions map shown in Fig. 7.23 have position dependence as expected.

7.6.2   Energy Dependence

Fig. 7.24 shows the distribution of the energy deposit. The calibration factor from signal charge to energy deposit is decided by comparing with a peak value of energy deposit in MC. The measured time and resolution depends on energy deposit on counters. In Fig. 7.25 and 7.26, the dependences are indicated with each heights of counters and each channel assignment. The time walk with energy dependence is observed in the figure. In main energy region of 0.5–1.5 MeV it is about several tens of pico-seconds. It is not large but correction of this effect will improve the time resolution. Concerning time resolution with energy deposit is also changed. In principle, the time resolution with larger energy deposit becomes better because of larger photon-electron statistics. However, in Fig. 7.26 it is not in the case from ∼13 MeV. It may come from pile up events in which two hits in the same counter are merged and the reconstructed energy looks large. Utilizing this resolution dependence on energy deposit to make probability density function event-by-event for likelihood analysis, final physics analysis in MEG II will be improved.

7.7   Overall Time Resolution

To estimate TC overall time resolution, even-odd analysis is applied as described in Sec. 6.1.2. Distribution of number of all hits is shown in Fig. 7.27. To eliminate pile up positrons, clustering is applied. The number of obtained clusters and the number of hits in a cluster is shown in Fig. 7.28.

Since we do not have any track information from DCH, we can not precisely reconstruct event-by-event trajectory in TC. Instead, we evaluate the multiple-hit time resolution
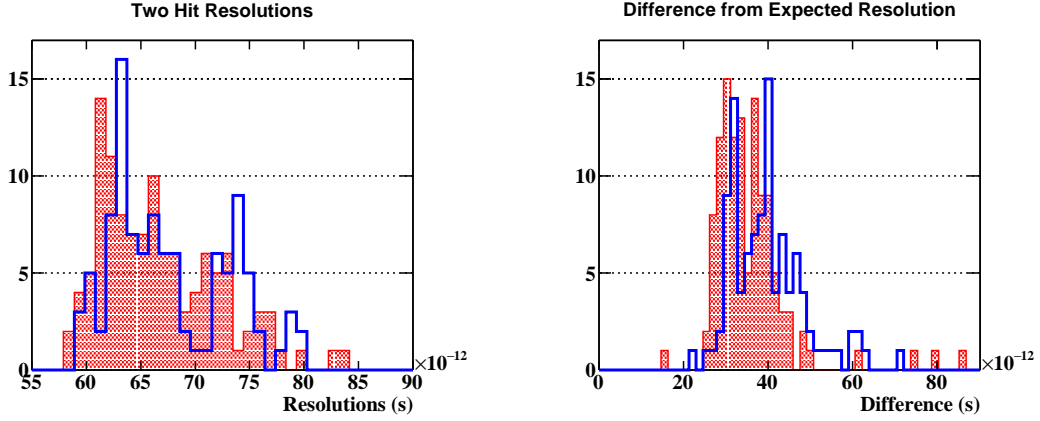
Figure 7.22: Resolutions of two counter hits (left) and resolution difference from the expectation of pre-test with ^{90}Sr source. The expectation values are corrected with energy deposit difference.
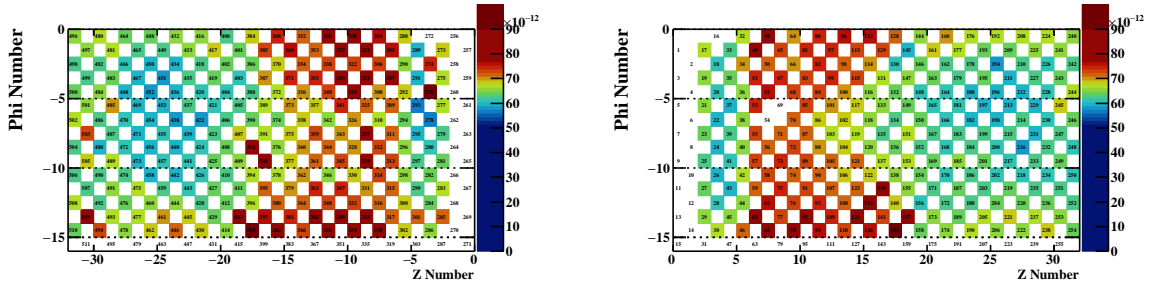

Figure 7.23: Resolutions map with two counter hits. Left is US result, and right is DS result. Numbers are position IDs of counters.

using fixed combinations of counters and the even-odd analysis. Each counter combination consists of counters with position IDs $(i, i+1, i+16, i+17, i+33, i+18, i+49, i+34, i+50, i+51)$ when i is even, and $(i, i-15, i+16, i+1, i+17, i+18, i+33, i+34, i+50, i+35)$ when i is odd, as shown in Fig. 7.29. We evaluate the N_{hit} resolution using events with hits on the first N_{hit} counters in each counter combination, and then, average them for all the combinations to get the overall time resolution for N_{hit}. The result as a function of N_{hit} is shown in a blue line in Fig. 7.30. In addition, we evaluate the overall time resolutions in a different way: we accumulate the fit Gaussian functions over all the combinations and fit the accumulated distribution with a Gaussian to get the overall resolution, as shown in Fig. 7.31. In this way, the local contribution of time calibration error can be taken into account because the center values of time difference distribution for different combinations vary due to the errors on the counter time offsets. It is to be noticed that the global bias effect is not seen in even-odd analysis in which the global bias is canceled out in the subtraction. As discussed in Sec. 7.5, the global bias can be corrected by the RMD events.

The red line in Fig. 7.30 shows the result. These two curves are fitted by $\sqrt{\frac{\sigma^2_{\text{single-all}}}{N_{\text{hit}}} + \sigma^2_{\text{MS}}}$ where $\sigma^2_{\text{single-all}} = \sigma^2_{\text{single}} + \sigma^2_{\text{inter-counter}} + \sigma^2_{\text{elec}}$ in Eq. 4.2. When just average of sigmas
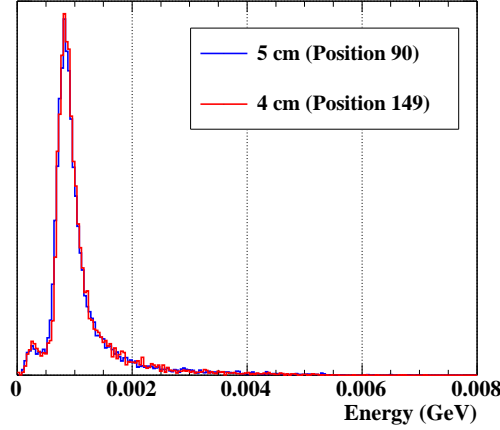
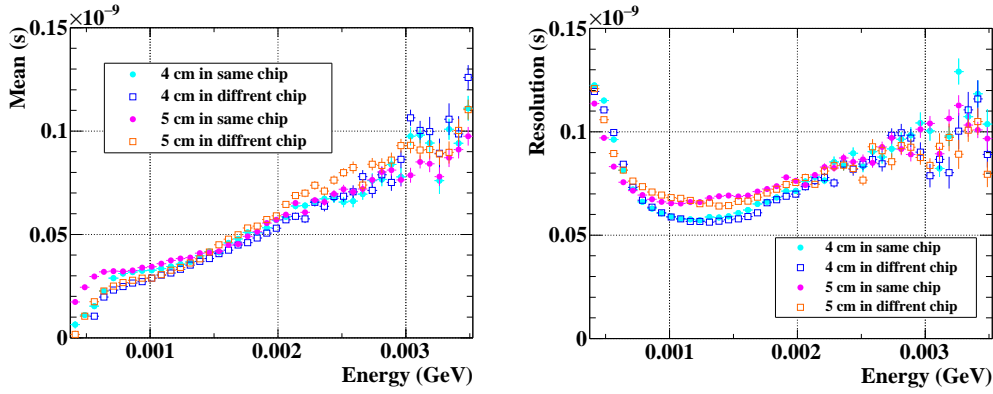Figure 7.24: Distribution of energy resolution in 4 cm (red), and 5 cm (blue) height counter.

Figure 7.25: Measured time as function of the energy deposit.

Figure 7.26: Time resolution as function of the energy deposit.

is taken, $\sigma_{\text{inter-counter}}$ is zero. The fit results are $\sigma^2_{\text{single-all}} = 96.4$ ps for average overall resolution, and $\sigma^2_{\text{single-all}} = 98.1$ ps for the overall resolutions by Gaussian accumulation way with negligibly small σ_{MS}. Consequently, $\sigma_{\text{inter-counter}}$ is estimated to be 18 ps from the difference between the two fit results.

The overall resolutions in 2017 pilot run are still worse than expectation from the mass test with ^{90}Sr source as shown in Fig. 7.30. The expected σ_{single} is 80.1 ps. Therefore additional contribution (calculated as the difference in quadrature) is 53.6 ps including electronics jitter. The electronics is measured before the pilot run in 2017, and it is ~20 ps. After subtracting the jitter, the difference between the pilot run and the Sr test is ~50 ps. This deterioration of the time resolution comes from the difference of the noise situations. Fig. 7.32 shows an example of the noise in two counters in the pilot run and the Sr test. The noise in the pilot run is ~5 mV which is doubled from that in Sr test. In Sec. 6.2.5, we observed that the noise affects the time resolution deeply. Fig. 6.20 indicates that doubled increased noise is possible to worsen the time resolution by several tens of ps.
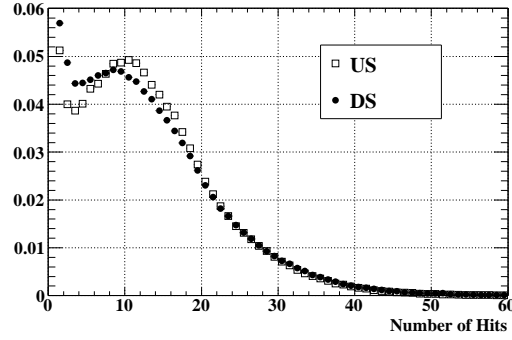
Figure 7.27: Number of hits distribution.

However even though the single resolutions are worse than the expectation, thanks to multiple hit scheme the degradation is suppressed by $\sqrt{N_{\text{hit}}}$ as shown in Fig. 7.33 and Fig. 7.34.

Finally the overall resolution for signal positrons is estimated to be 38.5 ps by weighting with the number of hits distribution of the signal positrons obtained by MC. The distribution is shown in Fig. 7.35. It is obtained after applying the whole reconstruction analysis. The time resolution of TC is improved by a factor of 2 from the MEG experiment (76 ps) and satisfy the requirement of ∼40 ps time resolution for a new TC in the MEG II environment.

7.8 Radiation Hardness

We monitored the current of the each channel. The current increasing indicates how much radiation damage counters had. Fig. 7.36 shows the distribution of the observed current increase for 32 hours for US and for 36 hours for DS. We observed 0.4 μA and 1 μA increasing in US and DS, respectively, which correspond to 158 μA and 394 μA current increasing for three years of MEG II running time. In the radiation tests as shown in Sec. 4.5.6, the resolution deterioration of 30 % is expected for the current increase of 100 μA. However by keeping the temperature at 10 degree the dark current can be reduced and the resolution deterioration are suppressed.
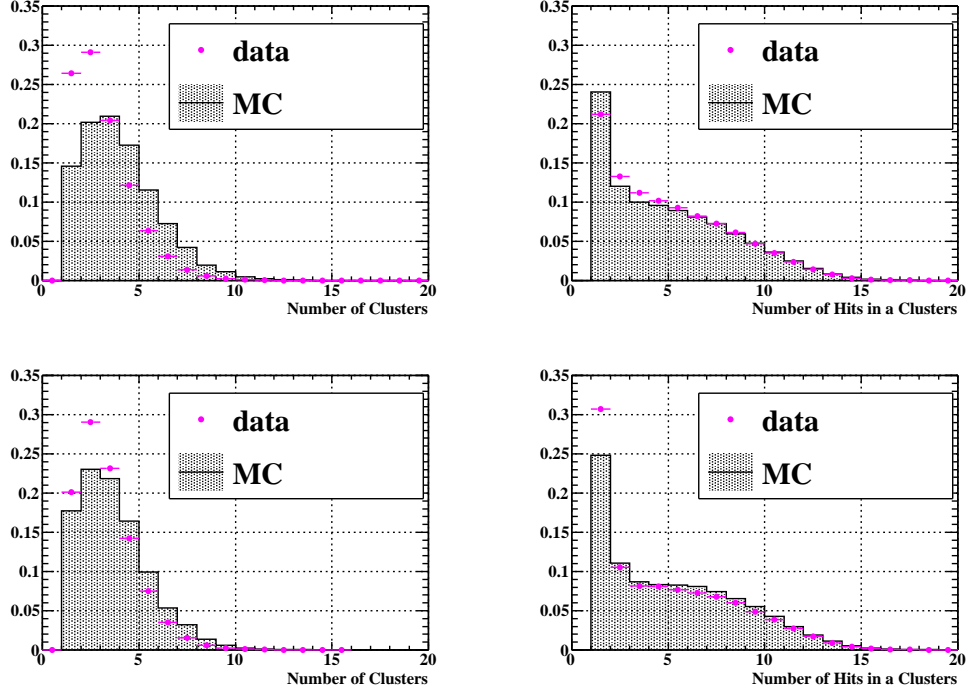
Figure 7.28: Number of clusters (left) and number of hits in a cluster (right) for DS (top) and US (bottom).
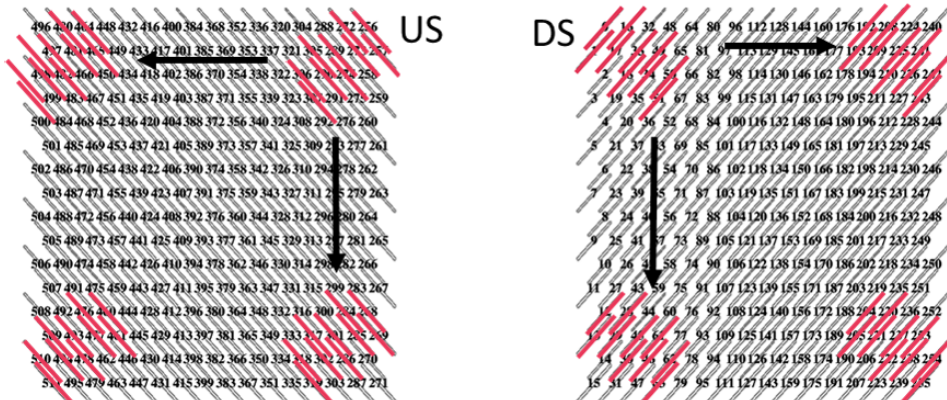

Figure 7.29: Schematic of the selection way for the resolution estimation with several number of hits.
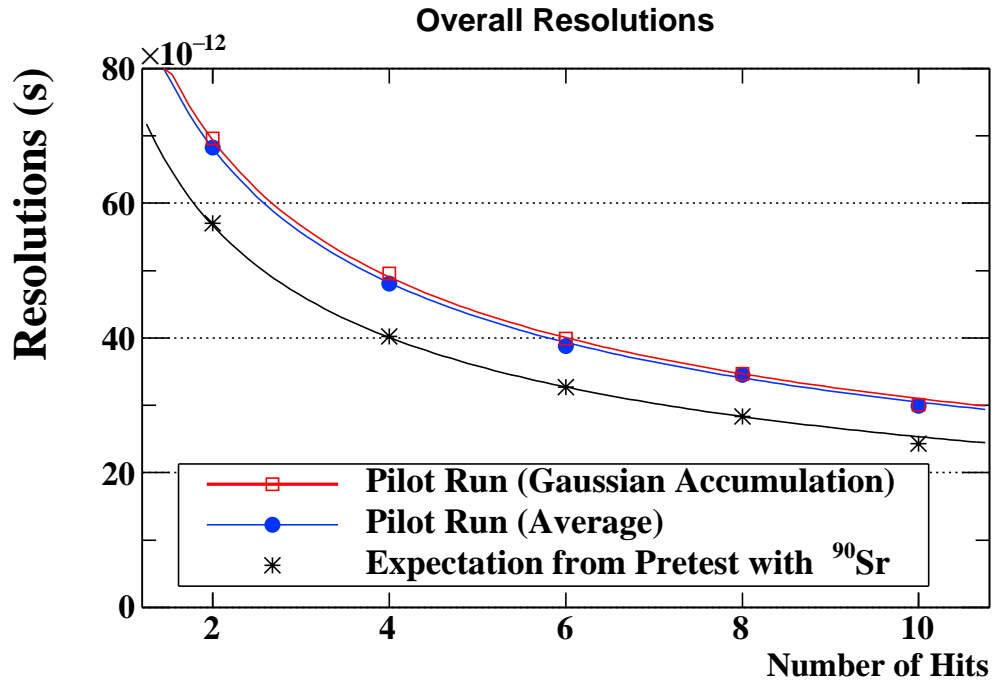
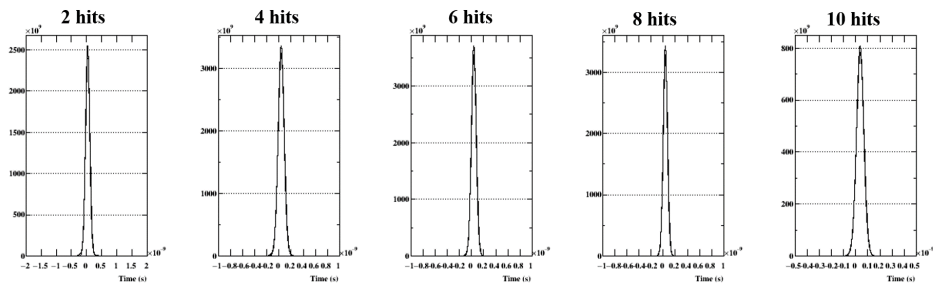Figure 7.30: Overall time resolution as a function of number of hits.

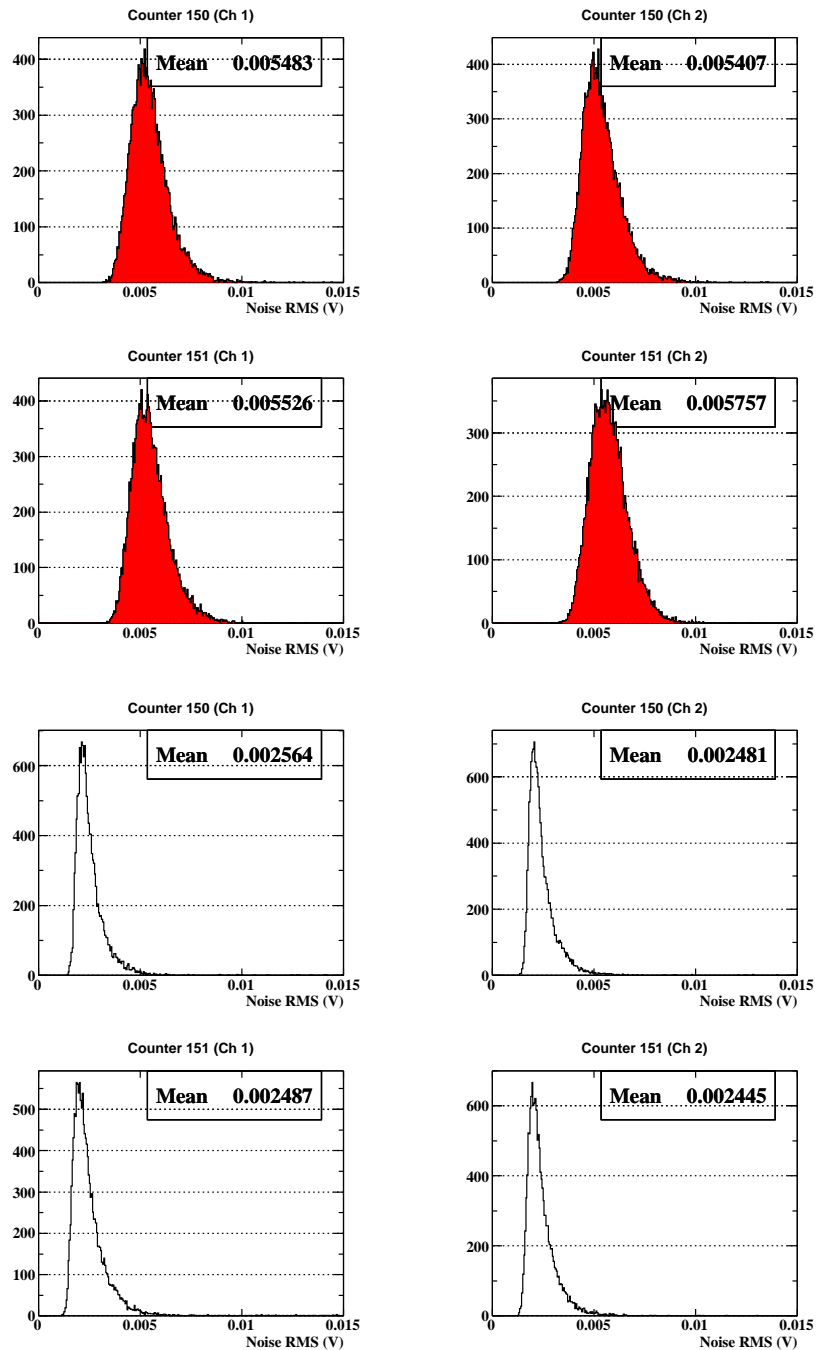Figure 7.31: Gaussian obtained by accumulating fit Gaussian over every counter combinations.

Figure 7.32: Typical noise RMS. The top figure is that in the pilot run, and the bottom is that in the Sr test.
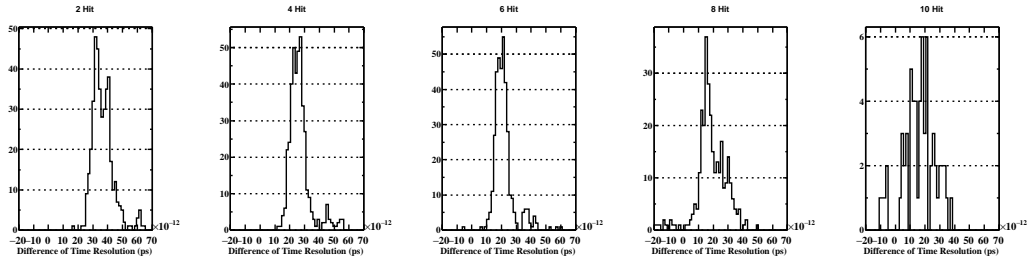
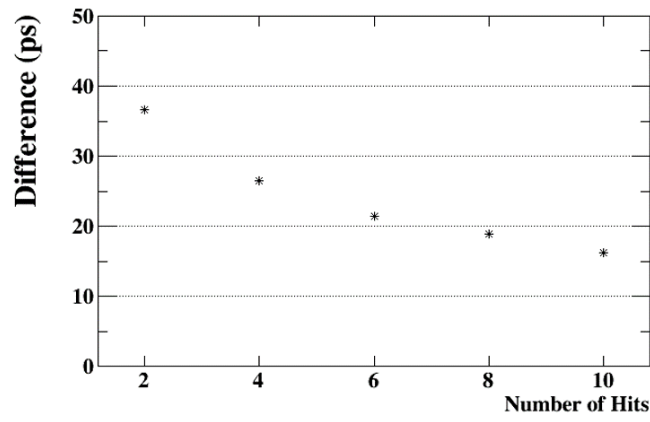Figure 7.33: Resolution difference from the expectation from mass test.

Figure 7.34: Resolution difference from the expectation from mass test with number of hits.
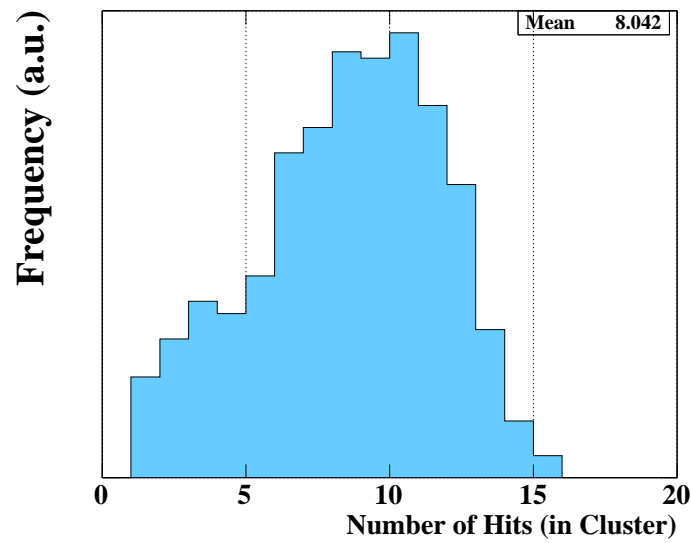

Figure 7.35: The number of hit distribution from the signal positrons after the full chain of the TC reconstruction in MC.
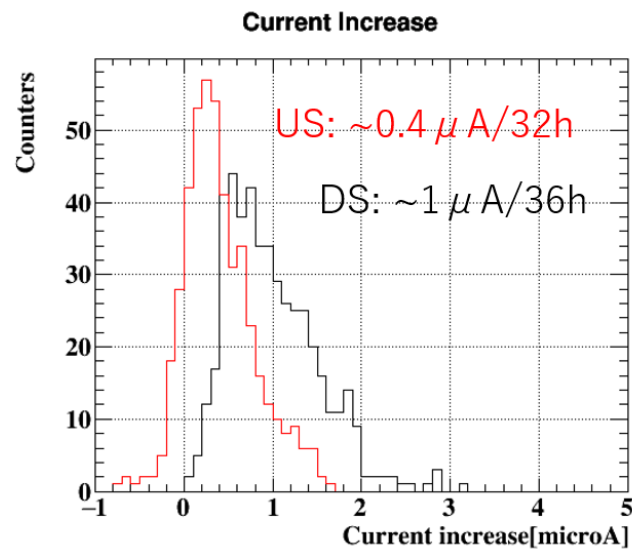
Figure 7.36: Current increase in pilot run 2017.

Chapter 8

Sensitivity Estimation

In this chapter, the sensitivity of the MEG II experiment will be discussed focusing on the performance of the positron spectrometer.

8.1 Performance of Positron Spectrometer

As shown in the previous sections, the multiple hit scheme is confirmed. The constructed TC indeed achieves the time resolution of $\sim$ 38.5 ps. The final goal of the positron spectrometer for the $\mu^+ \rightarrow e^+\gamma$ search is precisely to reconstruct the positron momentum, angle, vertex and time on the target. Moreover concerning the poor detection efficiency in the MEG experiment (30 %), achieving a high detection efficiency is another goal of the new spectrometer. In this section, the overall performance of the positron spectrometer will be discussed.

8.1.1 Combined Reconstruction

The DCH reconstructs the positron trajectory using TC hits information as the time seed and extrapolates the trajectory back to the target to reconstruct the momentum vector at the emission. At the other end, matching between DCH tracks and TC hits is examined. A reconstructed track in DCH is propagated to the first hit in each cluster in TC by calculating the equation of motion in COBRA magnetic field. If propagated position and TC hit position are in 5 σ of their combined resolution, they are matched.

8.1.2 MC Setup

Since DCH installation is not completed yet, the performance is estimated by the simulation. The signal positrons are generated uniformly in $0 < |\cos(\theta)| < 0.45$, and $-7/18\pi < \phi < 7/18\pi$ to cover the acceptance of the spectrometer. In addition, to estimate pile up effect of Michel positron background, Michel positrons are mixed at 7×10^7/s to the signal events.

8.1.3 Positron Time Resolution

There are two components which contribute to the positron timing resolution, while the other resolutions such as momenta and vertexes come from only DCH directly. One is the TC measurement whose independent performance is already demonstrated with the real detector as demonstrated in the previous sections, and the other is the flight time from

the target to the first hit point on TC calculated from the trajectory reconstructed by DCH.

As for the first point, all the information of hits in a cluster has to be combined into a time at the matched point (at the first hit counter). The hit time of each counter is converted into the time at the matched point by subtracting the propagation time from the matched point to the counter impact point, and then all the converted times are averaged to get the best estimate of the time at the matched point. To estimate the propagation times, we use the reconstructed trajectory extrapolated from the last DCH hits. This process was not tested in the pilot run analysis, in which we evaluate the TC overall performance to be 38.5 ps by the even-odd analysis, due to the lack of DCH. In the simulation, the time resolution at the matched point is obtained to be 31.0 ps as shown in Fig. 8.2.

The second contribution is shown in Fig. 8.1 and is 14.8 ps. It is large improvement from MEG. In the MEG experiment this contribution was 75 ps [40] which is almost the same as TC performance itself due to scattering by the material between DCH and TC. The single volume DCH having ability to track positrons just before TC realizes the reduction of scattering effect, which is one of the keys of positron spectrometer upgrade.
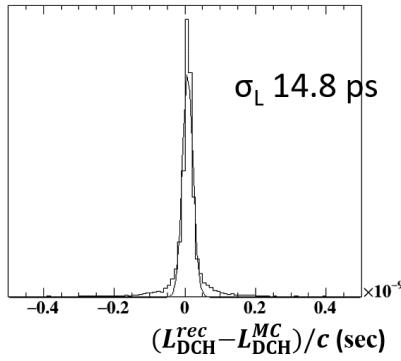

Figure 8.1: Reconstructed flight time between the target and TC obtained by DCH.
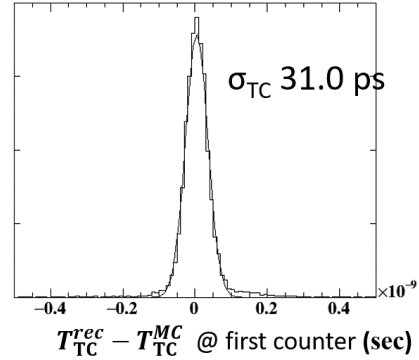

Figure 8.2: TC timing resolution in MC.

The tails in the distribution does not come from pile up. The comparison of the results between with and without background mixing is shown in Fig. 8.3. There is no large difference in the tail in the comparison. Poor track reconstruction in DCH, multi turn, or delta ray originated signal are possible to make the tail.

In conclusion the overall time resolution of the positron spectrometer is estimated to be

$$\sigma_{T_e} = 41.2 \text{ ps} \tag{8.1}$$

as the sum of squared of the measured time resolution of TC and the track contribution from MC. The time resolution of the spectrometer is more than twice better than that of MEG (107 ps).
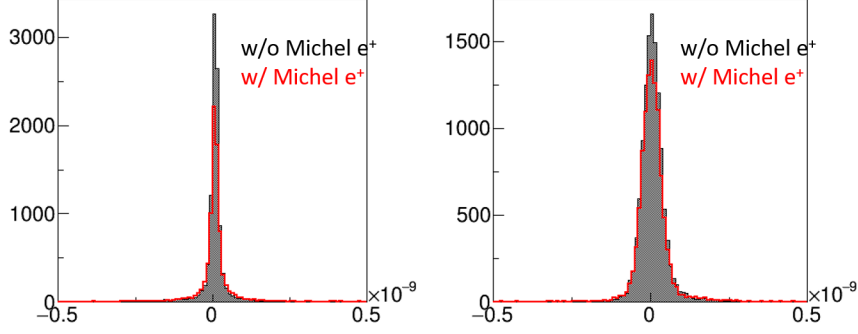
Figure 8.3: Time distribution comparison with pile up (red) without pile up (shaded). Left shows the flight time between the target and TC, and right shows time distribution measured by TC.

8.2 Efficiency

Since the LXe photon detector limits the geometrical signal acceptance, the positron detection efficiency is defined as the ratio to the number of accepted photon events. The photon acceptance is $|u| < 23.9$cm, $|v| < 67.9$cm on the inner face at $r = 64.84$cm, and in the simulation the judgment of photon accepted event or not is performed by the propagation from the inverted momentum of the true positron momentum. The positron detection efficiencies are summarized in Tab. 8.1. The detailed definition and discussion are as follows.

The distributions of the difference between the reconstructed observables of the signal positron and the true ones in MC are shown in Fig. 8.4 for the MC events of signal only and in Fig. 8.5 for those of signal and background mixed. When seeing the distributions in Fig. 8.4 and Fig. 8.5, one notices the long tails. When these tail events have correlation among the observable, it is likely to increase inefficiency. To simplify the event which at least one of reconstructed observable is out of 5 σ is not counted as an event detecting signal positron and becomes inefficiency. Fig. 8.6 shows that which combination of observables are out of window in the inefficiency event by the tail cut. Indeed in ∼70 % of cut events all the variables are reconstructed out of 5 σ.

Table 8.1: Efficiencies (%) in each step in the positron spectrometer.

	w/o pile up	w/ pile up
Photon accepted events	100	
DCH Reconstruction	81.9	63.0
Matching between DCH and TC	78.8	60.6
TC Reconstruction	76.4	56.1

In the DCH reconstruction, since almost all signal positron remain hits in DCH, main inefficiency comes from track reconstruction from reconstructed hits. There are three inefficiency in DCH reconstruction algorithm; (1) tail cut for vertex along Y, vertex along Z, θ, ϕ, and momentum as mentioned above; (2) propagation miss to TC region defined from $r = 27$ cm; and (3) further quality cut for reconstructed signal track having fake hits

more than 50 %.

Firstly, to recover the inefficiency from the tail cut track merge should be improved in the DCH track reconstruction. Fig. 8.7 shows the number of the reconstructed tracks without any pile up from Michel positron in MC. Even in the no background environment, the track merge is sometimes failed. The failure in the track merge worsens the quality of the reconstruction, which increases the inefficiency. The algorithm of the track merge should be optimized against multiple scattering.

Secondly, 20-30 % of the propagation miss to TC from DCH can be recovered by the modification of the algorithm, while the other is the intrinsic inefficiency coming from the multiple scattering as shown in Fig. 8.8. The former events have TC hits in the reconstructed track in DCH in which the starting point of the propagation is after TC hits and lose these hits. Using track segments before merging, the propagation should be succeeded.

8.3   Expected Sensitivity

The resolutions and the efficiencies summarized in Tab. 8.2 are assumed to estimate the MEG II sensitivity. Notice that the muon decay vertex reconstructed by the positron spectrometer is used to determine the photon emission angle as the direction from the vertex to the reconstructed photon conversion point in the LXe photon detector; therefore the resolutions of the vertex affects the measurement of the opening angle.

The time resolution of the LXe photon detector is expected to be 50–70 depending on the noise situation. Therefore as the positron time resolution is ∼40 ps, the resolution of $t_{e\gamma}$ is estimated to be 64–80 ps. On the other hand, in the MEG experiment the time resolutions of the photons and the positrons were 67 ps and 107 ps, respectively, and the resolution of $t_{e\gamma}$ was 126 ps. Since the timing measurement in the positron side is significantly improved by the innovative TC, we overcome the limitation of the time measurement from the positron side.

Table 8.2: Resolutions (σ) and efficiencies of MEG II parameters. Those in MEG are also shown for comparison.

Parameters	Performance		unit
	MEG II	MEG	
Resolution (σ)			
θ_{e+}	5.3	9.4	mrad
ϕ_{e+}	3.7	8.7	mrad
E_{e+}	130	380	keV
e^+ vertex (Y)	0.7	1.2	mm
e^+ vertex (Z)	1.6	2.4	mm
$u_\gamma/v_\gamma/w_\gamma$	2.6/2.2/5	5/5/6	mm
E_γ ($w < 2$ cm)/($w > 2$ cm)	1.1/1.0	2.4/1.7	%
$t_{e+\gamma}$	**64-80**	**126**	ps
Efficiency (%)			
Trigger	≈99	≈99	
γ	69	63	
e^+	56	30	

In the MEG experiment, the number of the signals, and backgrounds were estimated to extract the upper limit of $\mu^+ \to e^+\gamma$ decay at 90 % confidential level by the maximum likelihood analysis technique with the probability density functions (PDFs) of the observables prepared event by event [1]. The PDFs were also used to generate an ensemble of the simulated experiments (toy MC) with the assumption of zero signal to estimate the sensitivity. The sensitivity of MEG was thus defined as the medium of the upper limits distribution.

Following the MEG analysis, the sensitivity of the MEG II experiment is estimated with the two assumptions for $\sigma_{t_e\gamma}$ to be 64 ps and 80 ps as Fig. 8.9. Even in the conservative estimation of 70 ps photon timing resolution (which corresponds to $\sigma_{t_e\gamma} = 80$ ps), the sensitivity goes down to 6.3×10^{-14} in three years with the assumption the 140 DAQ days in each year. Moreover when the time resolution of the LXe photon detector is 50 ps, the sensitivity reaches 5.6×10^{-14}.
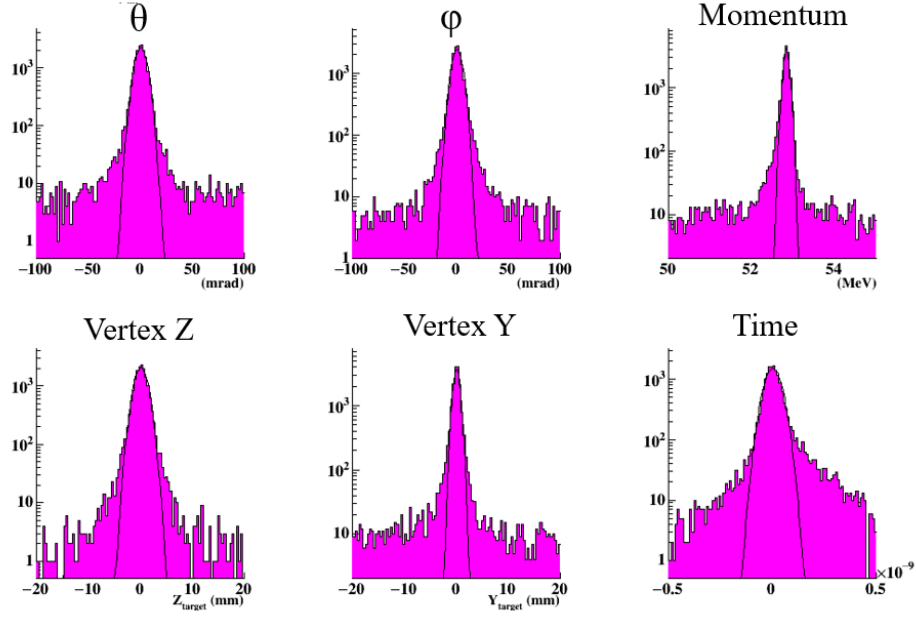
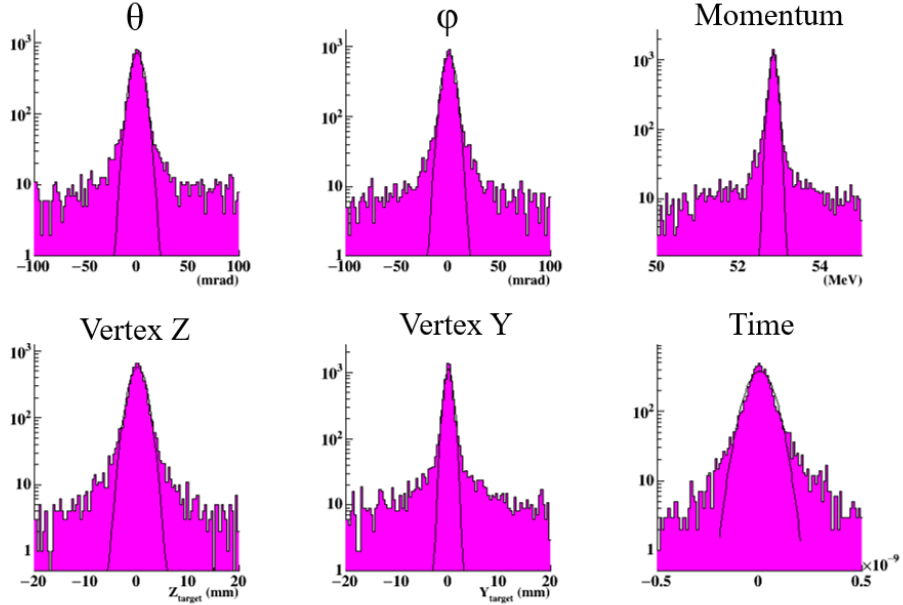Figure 8.4: Distribution of the reconstructed observables without effect of pile up.

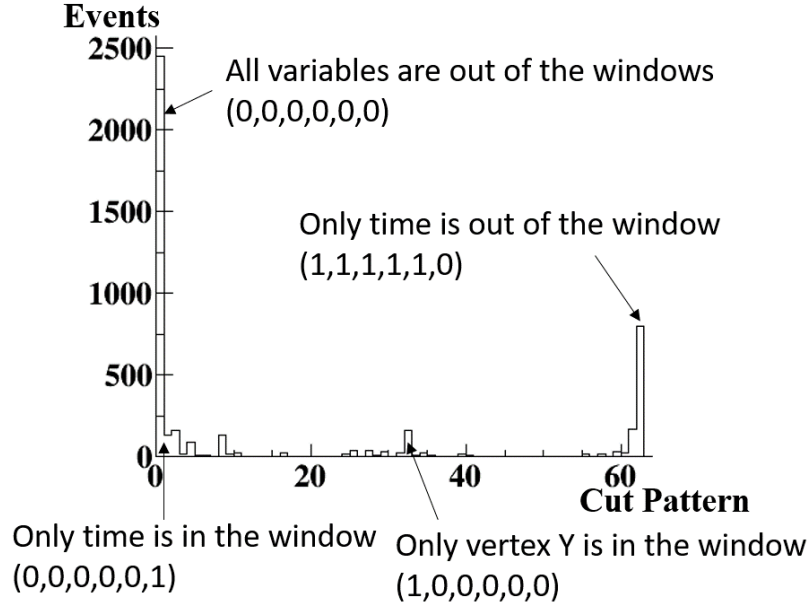Figure 8.5: Distribution of the reconstructed observables with pile up.

Figure 8.6: Correlation between each variable. Combinations are described as binary of (vertexY, vertexZ, θ, ϕ, P, T). When the reconstructed variable is out of 5 σ, 0 is assigned, while when in the window 1 is assigned.
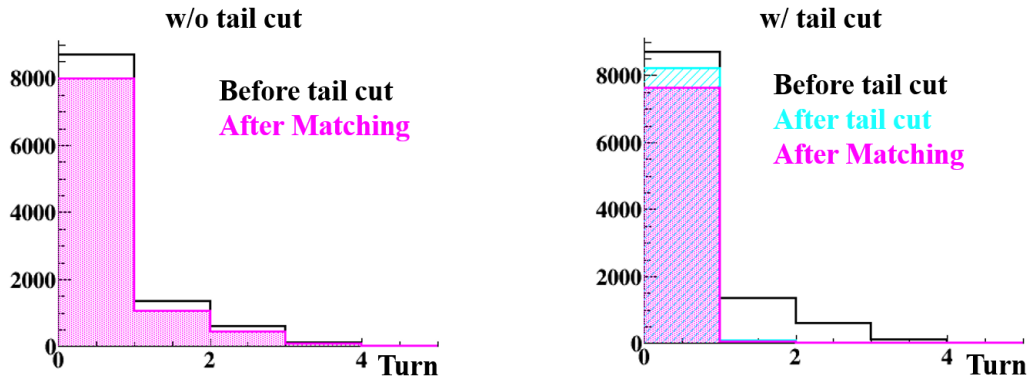

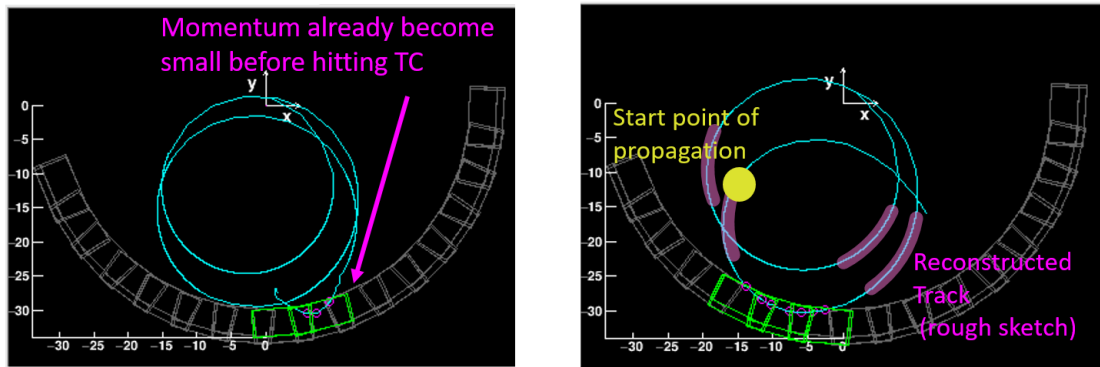Figure 8.7: Number of reconstructed tracks with (left) and without (right) quality cut to reconstructed observables

Figure 8.8: Event display of propagation miss to TC from reconstructed track in DCH in MC. Left: intrinsic inefficiency by multiple scattering, Right: event having TC hit among reconstructed track
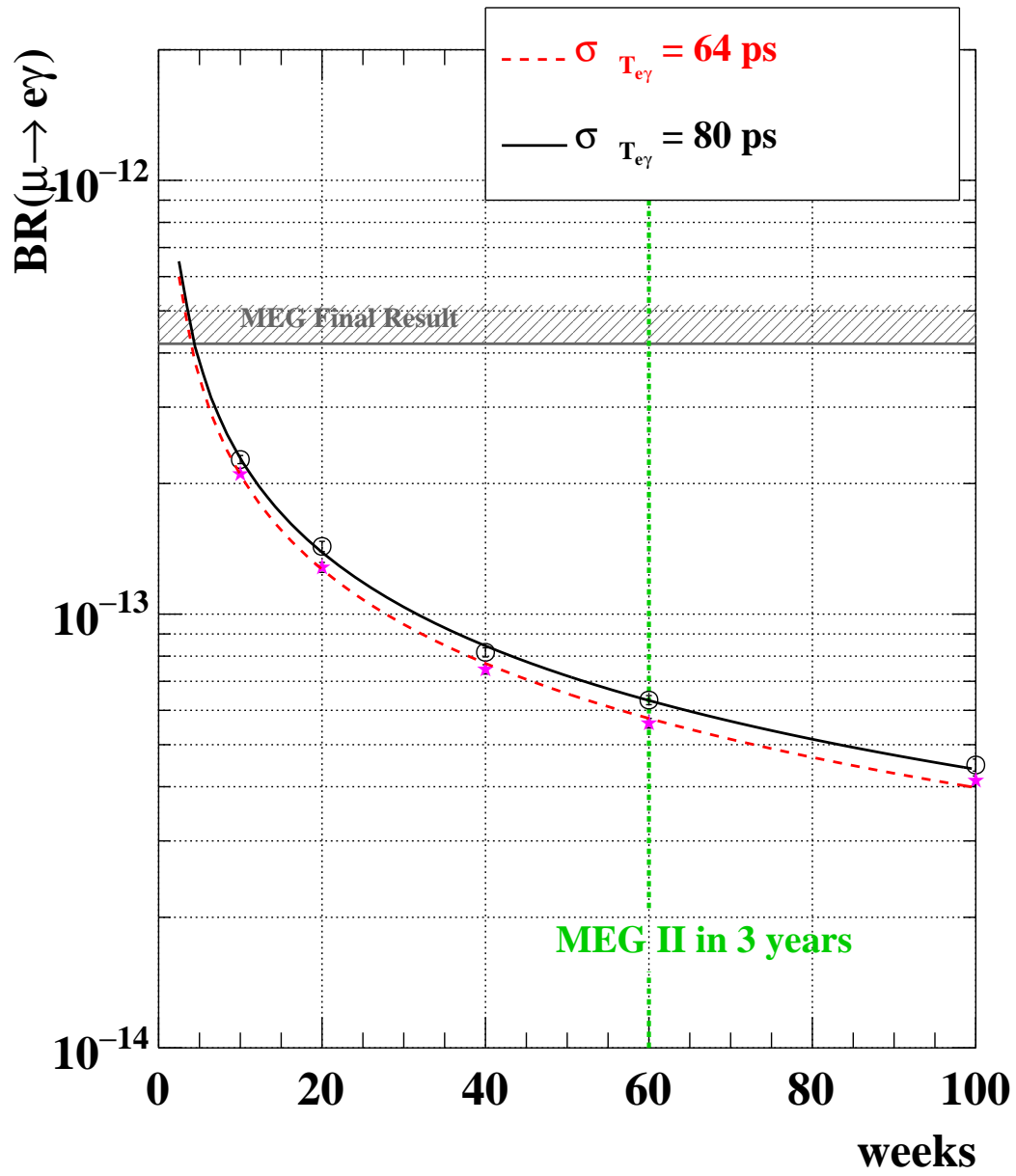
Figure 8.9: Expected sensitivity in MEG II to exclude the branching fraction with 90% C.L.

Chapter 9

Summary and Conclusion

To realize the search for the charged flavor violating decay, $\mu^+ \to e^+\gamma$, with an unprecedented sensitivity in the MEG II experiment, we have developed a positron timing counter. It is essential to increase the intensity of the muon beam two times higher than that in MEG. However it also makes more backgrounds, so the suppression of them is the key of the MEG II experiment. In the $\mu^+ \to e^+\gamma$ decay, a muon emits a positron and a photon simultaneously toward back-to-back direction having the energy of the half of the muon mass at the rest coordinate. The $\mu^+ \to e^+\gamma$ search is exposed to the positrons backgrounds from Michel decays and the photons backgrounds from the interaction of the positron with any material or the radiative muon decays. At the MEG II beam intensity, the accidental coincidence of the background positrons and the background photons becomes the dominant background. Since the distribution of the accidental background in the relative time window is the flat while the signals make a peak, the time measurement of both of positron and photon should be improved to enhance the sensitivity of the $\mu^+ \to e^+\gamma$ search.

The pixelated design is employed by using a new generation photo sensor, the silicon photo-multipliers (SiPM), and an ultra-fast plastic scintillator to measure the positron time with multiple hits which drastically improves the overall time resolution. The fine segmentation of TC also reduces the hit rate of the single counters, which enables TC to keep its time resolution even in higher positron background environment in the MEG II experiment.

The construction and installation of TC were completed in 2017. We conducted a pilot run successfully in late 2017. The calibration system and slow control system were operated in the pilot run. In the pilot run all the counters except for one counter worked properly. The single counter resolution including electronics jitter is obtained as 98.1 ps. Though the single counter resolution is worse than the expectation from the intrinsic counter resolution of $\sim$80 ps without electronics jitter, the ultimate time resolution below 40 ps is achieved with 8 counters. The obtained performance of the timing counter in the pilot run corresponds to 38.5 ps of the overall time resolution of the timing counter for the signal positron by scaling the expected number of hits from the signal.

The new trigger system is also successfully tested in the pilot run and we demonstrated the online time resolution of 415 ps, which reduces the trigger rate more than 50 % from the MEG experiment.

In the MC study the drift chamber is expected to reconstruct the flight time from the vertex to the timing counter with 14.8 ps resolution. Combining the drift chamber contri-

bution and the timing counter resolution, the time resolution of the positron spectrometer is expected to be 41.2 ps with the positron detection efficiency of 56.1 %. The time resolution for the signal positrons is improved to 38% of that in the MEG experiment. Though the detection efficiency still has room for improvement, it is already a large improvement from MEG by a factor of 1.87. As a result we can reduce the increasing background with the higher beam intensity in MEG II. It is concluded that the unprecedented sensitivity in the MEG II experiment 6×10^{-14}, which improves the sensitivity of the MEG experiment by one order of magnitude, is achievable with the MEG II detector including the new innovative timing counter discussed in this thesis.

Appendix A

Global Bias of Time Calibration

The global bias of the time calibration is observed as shown in Fig. 7.20. MC study indicates that the bias of estimation of the time of flight (TOF) among the counters makes the global bias in the track-based calibration though the detailed pattern of the bias is difficult to be predicted by MC.

In the MC study, at the beginning, *true* time offsets are prepared at random with Gaussian assumption. The true time offset is artificially added to true hit time in MC, and then the summed time are smeared with the counter resolutions as the reconstructed time.

In the pilot run, we use the TOFs estimated by MC instead of the tracks reconstructed by DCH. Almost all hits can be classified in three patterns as shown in Fig. 5.3. The true TOFs of the three pattern in MC are shown in Fig. A.1. By using the mean value of each TOF distribution, we calibrated the time offsets. Fig. A.2 shows the different between the true time offsets and the calibrated time offsets. The result has the global bias of ~50 ps
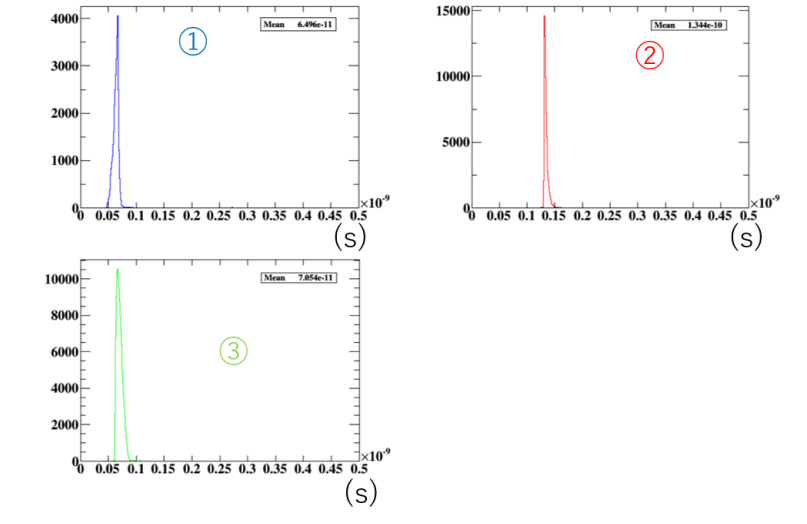

Figure A.1: TOF distributions for each hit pattern.

Fig. A.3 shows the closer view of Fig. A.1. The true TOF distributions have tail component. When the tail events are not used for the calibration, the bias becomes small as Fig. A.4. In this case the bias becomes smaller down to ~20 ps.
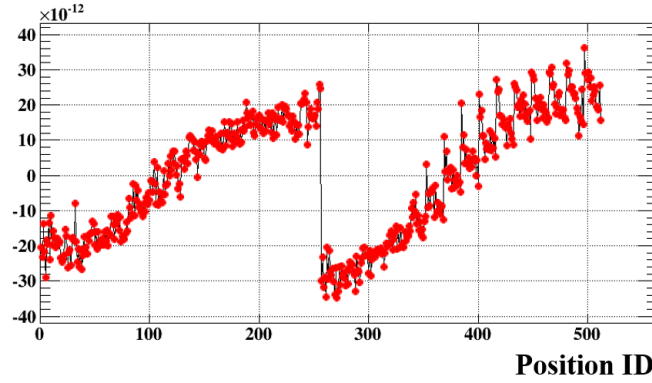
Figure A.2: Different between true time offsets and calibrated time offsets with three pattern TOF estimation

The mean of the TOF distributions are slightly different with the counter positions as shown in Fig. A.5 and these values are used in the pilot run tracked-based calibration. The result in the MC study is shown in Fig. A.6.

Fig. A.7 shows the result of another MC study in which the estimation of TOF have no bias, $+20$ ps bias, and -20 ps bias artificially. We smeared true TOFs with 10 ps Gaussian event by event as the TOFs used in the fit in track-based calibration. In the result no global bias is observed. On the other hand, when the estimations have bias, the global bias appears in the calibration result. The 20 ps bias generates ~ 1 ns global bias. Therefore even a few ps bias is expected to make observed global bias.

These MC study indicates that the track-based calibration is sensitive to the TOF estimation and the global bias observed in the pilot run is likely to be caused by the bias of the estimation of TOFs. The global bias is affected by TOF estimation bias of a few ps level. It is difficult to understand all components which change the TOF distribution, such as TC position, beam centering, background hits, and so on, in the level of ps. Though we cannot directly expect the global bias behavior for data, this global bias can be detected and corrected by using RMD events.
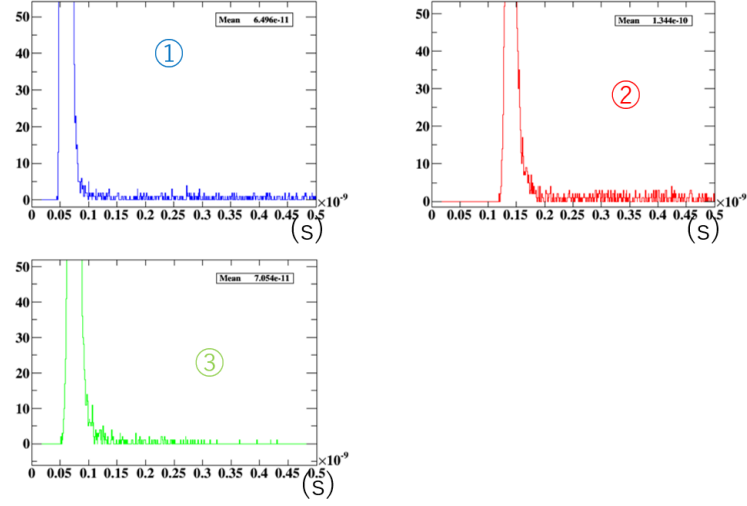
Figure A.3: Closer view of TOF distributions for each hit pattern.
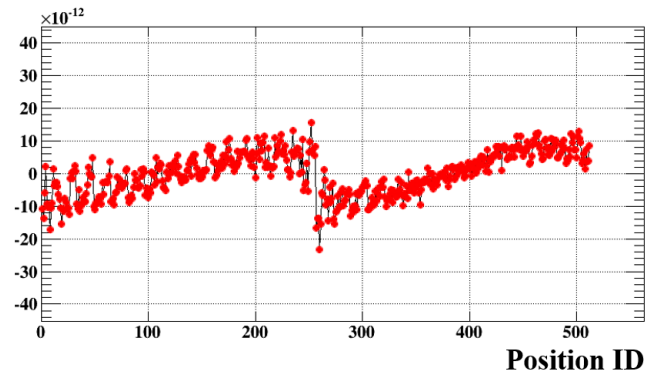

Figure A.4: Different between true time offsets and calibrated time offsets with tail cut of three pattern TOF estimation.
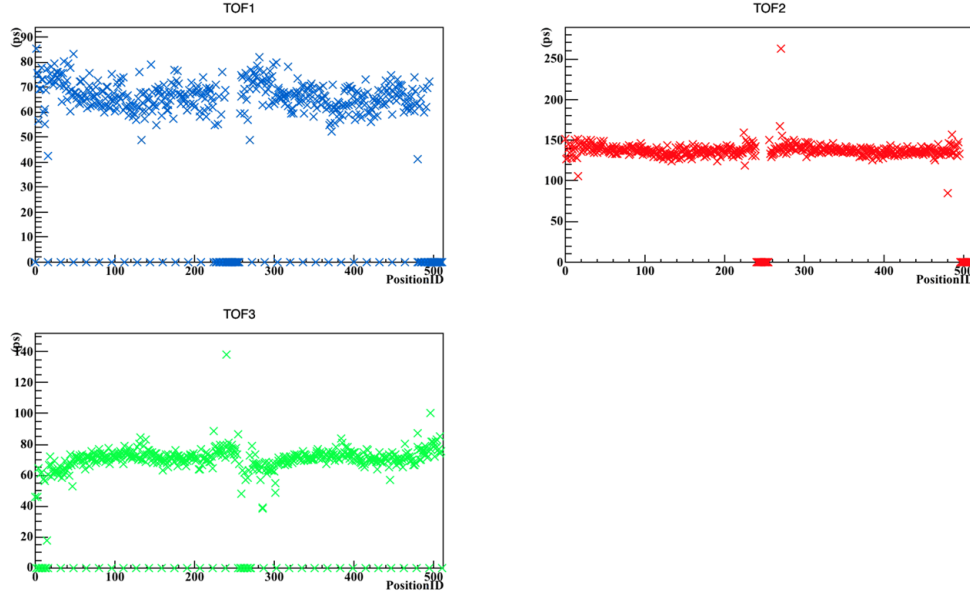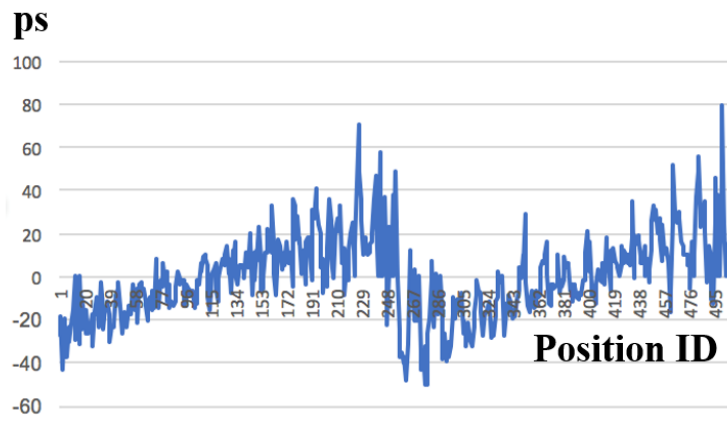
Figure A.5: TOF in each position.

Figure A.6: Different between true time offsets and calibrated time offset with same TOF estimation in the pilot run.
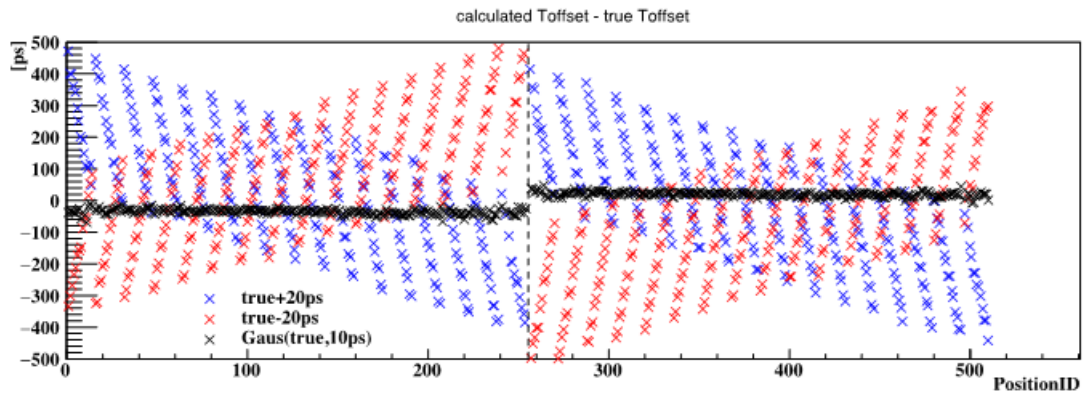
Figure A.7: Different between true time offsets and calibrated time offsets with TOF estimation with Gaussian (10 ps) error (black), $+20$ ps bias (blue), and -20 ps bias (red).

Appendix B

Optimization of Waveform Analysis

The waveform analysis for the single counter is optimized to perform the best resolution. The optimization of the single counter design we optimized the analysis for each set up. In Fig. 4.12 the connection of the SiPMs are compared. Since the waveforms are different each other, we also applied another constant fraction method based on amplitude and risetime compensation timing, while the final analysis for the TC extracts the time at a fixed ratio to the signal amplitude as described in Chap. 5. The data and optimal analysis in Fig. 4.12 is summarized in Tab. B.1.

Table B.1: Resolutions and optimized analysis.

Connection	Over Voltage (V)	Resolution (ps)	Optimal Analysis
Parallel	1.2	85.8	20%
	1.4	77.1	15%
	1.6	66.1	10%
	1.8	62.9	8%
	2	59.0	10%
	2.2	57.4	8%
	2.4	57.2	8%
	2.6	57.0	10%
	2.8	55.1	8%
Series	0.83	88.4	15%
	1.03	74.6	15% 1.5 ns delay
	1.23	68.5	15% 2 ns delay
	1.43	62.7	10%
	1.63	56.4	10% 2 ns delay
	1.83	55.3	20% 2 ns delay
	2.03	51.4	3%
	2.23	50.4	3%
	2.33	48.9	3%
	2.43	48.9	3%
	2.53	51.2	5%

Bibliography

[1] A. M. Baldini et al. (MEG Collaboration), Search for the lepton flavour violating decay $\mu^+ \to e^+\gamma$ with the full dataset of the MEG experiment. Eur. Phys. J. C **76**(8), 434 (2016). `doi:10.1140/epjc/s10052-016-4271-x`, `arXiv:1605.05081`

[2] S. P. Martin, A Supersymmetry Primer (2016), `arXiv:arXiv:hep-ph/9709356`

[3] G. Aad et al. (ATLAS Collaboration), Observation of a new particle in the search for the Standard Model Higgs boson with the ATLAS detector at the LHC. Phys. Lett. B **716**, 1–29 (2012). `doi:10.1016/j.physletb.2012.08.020`, `arXiv:1207.7214`

[4] S. Chatrchyan et al. (CMS Collaboration), Observation of a new boson at a mass of 125 GeV with the CMS experiment at the LHC. Phys. Lett. B **716**, 30–61 (2012). `doi:10.1016/j.physletb.2012.08.021`, `arXiv:1207.7235`

[5] S. H. Neddermeyer, C. D. Anderson, Note on the nature of cosmic ray particles. Phys. Rev. **51**, 884–886 (1937)

[6] S. T. Petcov, The processes $\mu \to e+\gamma$, $\mu \to e+e+\bar{e}$, $\nu' \to \nu+\gamma$ in the Weinberg-Salam model with neutrino mixing. Sov. J. Nucl. Phys. **25**, 340 (1977). Erratum ibid. 25 (1977) 698

[7] T. P. Cheng, L.-F. Li, $\mu \to e\gamma$ in theories with Dirac and Majorana neutrion-mass terms. Phys. Rev. Lett. **45**(24), 1908–1911 (1980). `doi:10.1103/PhysRevLett.45.1908`

[8] C. Patrignani et al. (Particle Data Group), Review of particle physics. Chin. Phys. C **40**(10), 100001 (2016). `doi:10.1088/1674-1137/40/10/100001`

[9] Y. Kuno, Y. Okada, Muon decay and physics beyond the standard model. Rev. Mod. Phys. **73**(1), 151–202 (2001). `doi:10.1103/RevModPhys.73.151`, `arXiv:hep-ph/9909265`

[10] P. Mikowski, $\mu \to e\gamma$ at a rate of one out of 10^9 muon decays? Phys. Lett. B **67**(4), 421–428 (1977). `doi:10.1016/0370-2693(77)90435-X`

[11] T. Yanagida, Horizontal gauge symmetry and masses of neutrinos. in *Proceedings Workshop on Unified Theories and Baryon Number in the Universe*, ed. by A. Sawada, A. Sugamoto, Tsukuba, Japan (1979). pp. 95–98

[12] M. Gell-Mann, P. Ramond, R. Slansky, Complex spinors and unified theories. in *Proceedings Supergravity Workshop at Stony Brook*, ed. by P. V. Nieuwenhuizen, D. Z. Freedman, New York, USA (1979). (North-Holland Pub. Co.), pp. 315–321. `arXiv:1306.4669`

[13] R. N. Mohapatra, G. Senjanović, Neutrino mass and spontaneous parity nonconservation. Phys. Rev. Lett. **44**(14), 912–915 (1980). `doi:10.1103/PhysRevLett.44.912`

[14] T. Moroi, M. Nagai, T. T. Yanagida, Lepton-flavor violations in high-scale SUSY with right-handed neutrions. Phys. Lett. B **728**, 342–346 (2014). `doi:10.1016/j.physletb.2013.11.058`, `arXiv:1305.7357`

[15] Y. Uchiyama, Analysis of the first MEG physics data to search for the decay $\mu^+ \to e^+\gamma$. PhD thesis, The University of Tokyo, 2009. `https://meg.web.psi.ch/docs/theses/uchiyama_phd.pdf`

[16] T. Kinoshita, A. Sirlin, Radiative corrections to Fermi interactions. Phys. Rev. **113**(6), 1652–1660 (1959). `doi:10.1103/PhysRev.113.1652`

[17] Y. Kuno, A. Maki, Y. Okada, Background suppression for $\mu \to e\gamma$ with polarized muons. Phys. Rev. Lett. **D55**(5), 2517–2520 (1997). `doi:10.1103/PhysRevD.55.R2517`, `arXiv:hep-ph/9609307`

[18] A. Bungau et al., Impact of the energy of the proton driver on muon production. in *Proceedings of IPAC'10*, 259 (2010)

[19] A. Kolano et al., Intensity limits of the PSI Injector II cyclotron (2017). `arXiv:1707.07970`

[20] The proton accelerator at the paul scherrer institute: forty years of top-flight research `https://www.psi.ch/media/the-psi-proton-accelerator`

[21] Injector 2: a pre-accelerator for protons `https://www.psi.ch/media/injector-2-a-pre-accelerator-for-protons`

[22] M. Seidel et al., Production of a 1.3 MW proton beam at PSI. in *Proceedings of IPAC'10*, 1309 (2010)

[23] A. E. Pifer, K. Browen, K. R. Kendall, A high stopping density μ^+ beam. Nucl. Instrum. Methods **135**, 39–46 (1976). `doi:10.1016/0029-554X(76)90823-5`

[24] A. Baldini et al. (MEG II Collaboration), The design of the MEG II experiment (2018), `arXiv:1801.04688`

[25] T. Haruyama et al., Development of a high-power coaxial pulse tube refrigerator for a liquid xenon calorimeter. CEC **710**(1), 1459–1466 (2004). `doi:10.1063/1.1774839`

[26] S. I. of Ceramics, Lyso crystal data sheet `http://www.siccas.com/LYSOScintillatorCrystal.htm`

[27] S. Ritt, The DRS chip: cheap waveform digitizing in the GHz range. Nucl. Instrum. Methods A **518**(1-2), 470–471 (2004). `doi:10.1016/j.nima.2003.11.059`

[28] *MIDAS : midas.psi.ch*

[29] M. Nishimura et al., Pixelated positron timing counter with SiPM-readout scintillator for MEG II experiment. in *Proceedings 4th Int. Conf. on New Photo-Detectors*, Moscow, Russia, (2016). PoS(PhotoDet 2015)011

[30] Saint-Gobain Ceramics & Plastics, Inc., BC-418, BC-420, BC-422 Premium Plastic Scintillators `http://www.crystals.saint-gobain.com/sites/imdf.crystals.com/files/documents/sgc-bc418-420-422-data-sheet_69699.pdf`

[31] R. A. Lerche, D. W. Phillon, Rise time of BC-422 plastic scintillator < 20 ps. in *Conference Record 1991 IEEE Nuclear Science Symposium and Medical Imaging Conference*, Santa Fe, NM (1991). pp. 167–170. `doi:10.1109/NSSMIC.1991.258899`

[32] P. W. Cattaneo et al., Development of high precision timing counter based on plastic scintillator with SiPM readout. IEEE Trans. Nucl. Sci. **61**(5), 2657–2666 (2014). `doi:10.1109/TNS.2014.2347576, arXiv:1402.1404`

[33] Millepede ii `http://www.desy.de/~kleinwrt/MP2/doc/html/index.html#ref_sec`

[34] S. Agostinelli et al. (Geant4 Collaboration), Geant4—a simulation toolkit. Nucl. Instrum. Methods A **506**, 250–303 (2003). `doi:10.1016/S0168-9002(03)01368-8`

[35] Ltspice (analog devices home page) `http://www.analog.com/en/design-center/design-tools-and-calculators/ltspice-simulator.html?domain=www.linear.com`

[36] G. Mazzitelli et al., Commissioning of the DAΦNE beam test facility. Nucl. Instrum. Methods A **515**(3), 524 – 542 (2003). `doi:DOI:10.1016/j.nima.2003.07.017`

[37] S. Ritt, R. Dinapoli, U. Hartmann, Application of the DRS chip for fast waveform digitizing. Nucl. Instrum. Methods A **623**(1), 486–488 (2010). `doi:10.1016/j.nima.2010.03.045`

[38] DRS4 Evaluation Board `http://www.psi.ch/drs/evaluation-board/`

[39] R. E. Kalman, A new approach to linear filtering and prediction problems. Trans. ASMEJ. Basic Engineering **D 82**, 35–45 (1960)

[40] J. Adam et al., The MEG detector for $\mu^+ \to e^+\gamma$ decay search. Eur. Phys. J. C **73**, 2365 (2013). `doi:10.1140/epjc/s10052-013-2365-2, arXiv:1303.2348`

Acknowledgments

Through this study my dreams came true. They were to study science deeply, and to go abroad and work with colleagues all over the world. I was really lucky to have enriching time in Switzerland.